OPTICAL µ-PRINTING OF POLYMER 3D MICRO-OPTICS/COMPONENTS FOR OPTO-BIO-MICROSYSTEMS

OUYANG XIA

PhD

The Hong Kong Polytechnic University

2020

The Hong Kong Polytechnic University
Department of Electrical Engineering

Optical μ-Printing of Polymer 3D Micro-Optics/Components for Opto-Bio-Microsystems

OUYANG Xia

A thesis submitted in partial fulfillment of the
requirements for the degree of Doctor of Philosophy

August 2019

CERTIFICATE OF ORIGINALITY

I hereby declare that this thesis is my own work and that, to the best of my knowledge and belief, it reproduces no material previously published or written, nor material that has been accepted for the award of any other degree or diploma, except where due acknowledgment has been made in the text.

_______________________________________(Signed)

_________________OUYANG Xia__________(Name of student)

Abstract

Bio-microsystems or biochips are an ensemble of microfluidic systems with bioassay and manipulation micro-components and have many advantages ranging from low expense and high throughput to miniaturization and multifunction, which thus promise great potentials in e.g. biomedical diagnostics and tissue engineering. Recently, optical micro-devices have been demonstrated as a promising component to be integrated within bio-microsystems for a new generation of biochips, called opto-bio-microsystem. Compared with conventional bio-microsystems, it has potentials in ultrasensitive measurement of variations of cellular phenotypes and biomolecules and provides a new technology for study cell behavior. In this thesis, two kinds of polymer optical micro-devices, i.e. top-lensed microlens array and 3D μ-printed microlaser biosensors, and a cellular-scale 3D microscaffold array are developed for bio-microsystem applications.

Firstly, polymer microlens arrays with lens-on-lens structures were designed and fabricated by using custom-built digital mirror devices (DMD)-based optical μ-printing technology. Top-lensed microlens (TLML) were designed to achieve special focal structures with either elongated focal length or two distinct foci. For precise fabrication of the complex profiles, the relation between the exposure dose of UV light and cured depth of photopolymer was studied, which can be utilized to correct the bitmaps of dynamic exposure schemes of the microlenses. We experimentally demonstrated that the TLML with elongated focal structure has a depth of focus at half maximum of 767.11 μm, and another TLML has two separate foci with a gap of 280 μm. The microlenses with the capability of advanced beam shaping have potentials in integration of biochips for fluctuating target detection.

Secondly, polymer optical whispering-gallery mode (WGM) resonator laser sensors were 3D printed and integrated into an optofluidic biochip for detection of vascular endothelial growth factor (VEGF). By using the bitmaps with corrected exposure dose, three groups of optical microresonators with suspended microdisks of different radius, whose quality (Q) factor can reach around 9800, were successfully fabricated. By coating a thin layer of gain material, the WGM resonators can support lasing operation with very low threshold (around 0.2 nJ). The microlasers were then integrated into a microfluidic chip to achieve an optofluidic platform for enzyme-linked immunosorbent assay (ELISA) processing. Such an ELISA biochip can detect VEGF at the detection limit as low as 17.8 fg/mL.

Lastly, 3D cellular-scale microscaffold arrays with various dimensions and combinations were designed and fabricated by using custom-built optical 3D μ-printing technology for 3D cell culture. Single-cell-size cubic microscaffolds were fabricated and utilized to facilitate cells to spread along the suspended beams of microscaffolds. It is found that with the increasingly top-opening area of the cubic microscaffolds, the area of cell spreading will be larger, which will enhance the mechanosensing signaling, and hence promote osteogenesis in cell differentiation. Furthermore, on the top of the suspended beams of 3D microscaffolds, bioactive material (gelatin methacrylate) were selectively patterned, which enabled controlled cell adhesion and spreading in 3D microenvironment.

Publications arising from the thesis

Journal papers:

1 **X. Ouyang**, T. Liu, Y. Zhang, J. He, Z. He, A. P. Zhang and H. Y. Tam, "Ultrasensitive optofluidic enzyme-linked immunosorbent assay by on-chip integrated polymer whispering-gallery-mode microlaser sensors," under review.

2 **X. Ouyang**, Z. Yin, J. Wu, C. Zhou, and A. P. Zhang, "Rapid optical μ-printing of polymer top-lensed microlens array," Optics Express 27, 18376-18382 (2019).

3 **X. Ouyang**, K. Zhang, J. Wu, D. S. Wong, Q. Feng, L. Bian, and A. P. Zhang, "Optical μ-Printing of Cellular-Scale Microscaffold Arrays for 3D Cell Culture," Scientific Report 7, 8880 (2017).

4 M. Yao, **X. Ouyang**, J. Wu, A. P. Zhang, H. Y. Tam, and P. K. A. Wai, "Optical Fiber-Tip Sensors Based on In-Situ micro-Printed Polymer Suspended-Microbeams," Sensors (Basel) 18(2018).

5 Y. Zhang, Q. Zhang, **X. Ouyang**, D. Y. Lei, A. P. Zhang, and H. Y. Tam, "Ultrafast Light-Controlled Growth of Silver Nanoparticles for Direct Plasmonic Color Printing," ACS Nano 12, 9913-9921 (2018).

6 Y. Zhang, M.-J. Yin, **X. Ouyang**, A. P. Zhang, and H.-Y. Tam, "3D μ-printing of polytetrafluoroethylene microstructures: A route to superhydrophobic surfaces and devices," Applied Materials Today 19,

100580 (2020).

Conference papers:

1 **X. Ouyang**, Y. Zhang, J. He, Z. Liang, A. P. Zhang, and H.-Y. Tam, " 3D μ-Printed Polymer Whispering-Gallery-Mode Microcavity Laser Sensor Array", in CLEO/Europe-EQEC Conference, OSA Technical Digest (Optical Society of America, 2019), CE-11.4.

2 **X. Ouyang**, J. He, A. P. Zhang, and H.-Y. Tam, "Optical 3D μ-Printing of Polymer Whispering-Gallery-Mode Microcavity Lasers," in Frontiers in Optics / Laser Science, OSA Technical Digest (Optical Society of America, 2018), JW3A.27.

3 **X. Ouyang**, Z. Yin, J. Wu, A. P. Zhang, and C. Zhou, "Fabrication of Dual-Focus Microlens Array by Using Dynamic Optical Projection Stereolithography," in CLEO Pacific Rim Conference 2018, OSA Technical Digest (Optical Society of America, 2018), Th4H.6.

4 M. Yao, **X. Ouyang**, A. P. Zhang, H.-Y. Tam, and P. K. A. Wai, "Optical fiber-tip microfluidic refractive-index sensors," in CLEO Pacific Rim Conference 2018, OSA Technical Digest (Optical Society of America, 2018), F1E.3.

5 Y. Zhang, M. Yin, **X. Ouyang**, A. P. Zhang, and H. Tam, "Optical 3D μ-printing of polytetrafluoroethylene (PTFE) microstructures," in 2018 IEEE Micro Electro Mechanical Systems (MEMS), 2018), 37-40.

Acknowledgements

First of all, in my heart, I would like to express my heartfelt thanks to my chief supervisor, Dr. A. Ping Zhang. I can only use the word ‘lucky’ to express the meet between my supervisor and me. In the past four years, his support for my studies and the concern for life are the prerequisites for my successful completion of the thesis. In the past four years, he has given me the best research training, which not only improved my ability to think independently, but also inspired me to move forward. His keen research insight has deeply impressed me. It can be said that the publication of each of my articles has condensed a lot of his efforts. His persistent pursuit of scientific research has deeply influenced me. He has given me the courage and determination to continue to engage in scientific research. Therefore, Dr. Zhang is the first person I want to thank, and I am truly grateful to him.

I would appreciate the guidance and assistance from Dr. Liming Bian, my co-supervisor, who inspired me a lot on combination of biology and optical printing. His advices on my research help me overcome many difficulties.

I would like to thank Prof. Hwa-yaw Tam, my co-supervisor, for giving me the opportunity to study in such a great lab. Prof. Tam’s profound English skills and rigorous academic attitude have benefited me a lot.

I am grateful to those who provided many helps on my experiments and thesis. I would like to thank Dr. Jushuai Wu, Dr. Mingjie Yin, and Dr. Shaorui Gao for their great help from the beginning of my research. I wish to thank Dr. Kunyu Zhang, Mr. Zhengkun Yin, Dr. Jijun He, Mr. Siqi Li, Miss. Yunfeng Wang, Miss Yilin Liu and Mr. Zijian He for their help in my experiment design and setup of experiment. I appreciate Mr. Song Zhu, Dr. Xinbiao Xu, Dr. Shuai Liu and Dr. Xiaochong Yu for their help on simulation. I would also express my appreciation to Dr. Yangxi Zhang, Mr. Mian Yao, Mr. Feng Xiong, Mr. Zengtian Liang, Miss Zuoqin Ding, Miss Bei Huang, Mr. Bo Zhang, Miss Tong Liu, Dr. Jie Wang, Dr. Xin Guo, Mr. Xin Cheng, Dr. Zhengyong Liu, Dr. Anand Mohan, Mr. Virag S. Raut, Mr. Yu Wang, Mr. Gang Yang, Dr. Dexter Siu-Hong Wong, Miss. Yaxi Yan, Dr. Julien Bonefacino, Mr. Yun Qi, Dr. Qitao Lue, Ms. Jing Zuo, Mr. Yan Zhao, Mr. Fengze Tan, and Ms. Pendy Ho for their discussion.

I wish to express my gratefulness to my friends for their help and encouragement in my life and study in HK where I had great times.

Last but not least, I am very grateful to my family for their care and encouragement. Especially, I would like to say a heartfelt thank you to my parents for their dedication, support, believing in me and encouraging me to overcome difficulties. I also appreciate Dr. Zidan Gong for her warmest encouragement and care. I would like to dedicate this thesis to them and express profound gratitude and love!

TABLE OF CONTENTS

page

List of Figures

List of Table

List of Acronyms

Acronyms	Description
WGM	Whispering gallery mode
TLML	Top-lensed microlens
DLP	Digital light processing
SEM	Scanning electron microscope
PDMS	Polydimethylsiloxane
LED	Light-emitting diodes
FWHM	Full width at half maximum
PMMA	Poly(methyl 2-methylpropenoate)
SMF	Single mode fiber
HRP	Horseradish peroxidase
TMB	3,3′,5,5′-tetramethylbenzidine
ICG	Indocyanine green
TEOS	Tetraethyl orthosilicate
DLD	Deterministic lateral displacement
CTCs	Circulating tumor cells
GEM	Geometrically enhanced mixing
TPP	Two-photon polymerization
DMD	Digital micromirror device

PEGDA	Polyethylene glycol diacrylate
PETA	Pentaerythritol triacrylate
TBA	Tributylamine
Rh6G	Rhodamine 6G
ELISA	Enzyme-linked immunosorbent assay
VEGF	Vascular endothelial growth factor
BSA	Bovine serum albumin
HRP	Horseradish peroxidase
LOD	Limit of detection
APTES	(3-aminopropyl)triethoxysilane
TMB	3,3′,5,5′-tetramethylbenzidine
PBS	Phosphate buffered solution
RT	Room temperature
PGMEA	Propylene glycol monomethyl ether acetate
OSA	Optical spectrum analyzer
FSR	Free-space ranges
DOPsL	Dynamic optical projection stereolithography
GelMA	Gelatin methacrylate
PC-2506	4-((2-hydroxytetradecyl)oxy)phenyl)-phenyliodoniu
DI	Deionized
TEMPO	2,2,6,6-tetramethylpiperidine 1-oxyl

AA	Acrylic acid
HMBS	2-hydroxy-4-methoxybenzophenon-5-sulfonic acid
hMSCs	Human mesenchymal stem cells
YAP	Yes-associated protein

Chapter 1

Introduction

1.1 Background

Opto-bio-microsystems have shown their great promise for biomedical assays, diagnostics and clinical applications [1]. It consists of a large ensemble of micro-scale devices (**Figure 1.1**) that are integrated and work together for biological or biochemical purposes ranging from diagnostics to therapy [2]. Optical micro-devices are attractive in bio-microsystems because of its ultrasensitive detection abilities as well as the advantages including miniaturization, immune to electromagnetic interference, and noninvasive [3]. With the development of micro-fabrication technologies, various optical micro-devices, such as microlens array [4], optical waveguide [5], and optical microresonators [6, 7], can be fabricated and investigated in areas of optical detection [8, 9], nonlinear optics [10], and low-threshold lasers [11, 12]. Micro-components using biocompatible materials and supporting components [13] also play an important role in bio-microsystems and can be used in e.g. regeneration and transplantation of tissues, such as skin and bone [14]. By integrating the micro-optics and microstructures on a chip, the monolithic system can not only study cell behavior but also enable real-time monitoring of living cells [15], which plays an important role in cell studies [16].

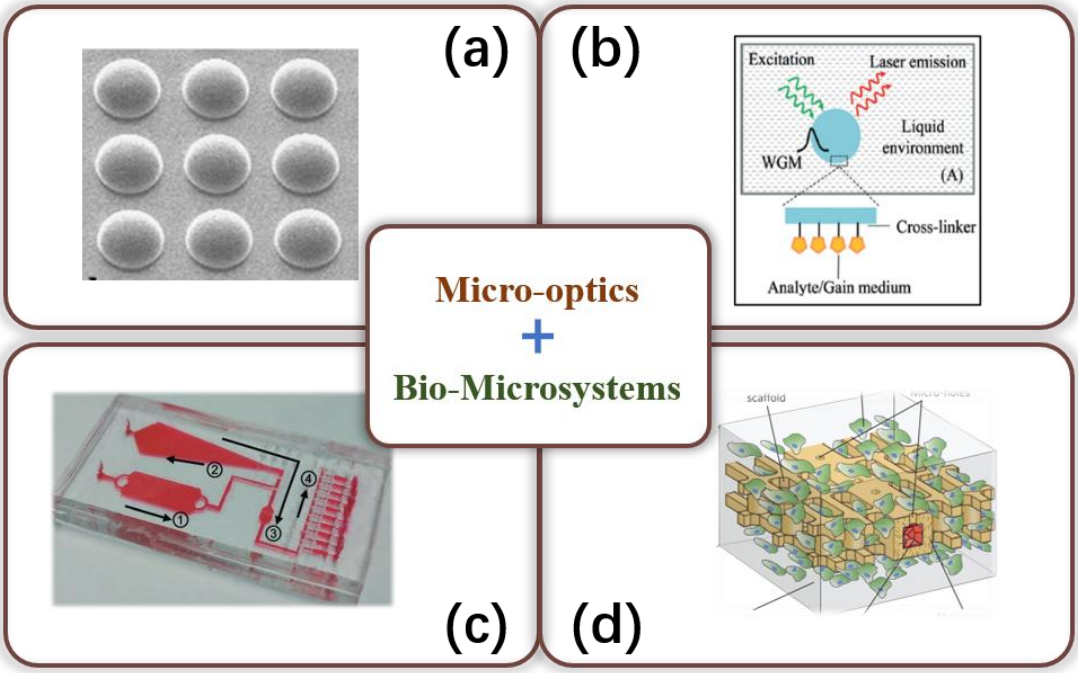

Figure 1.1 Two elements of opto-bio-microsystems: micro-optics and bio-microsystems. (a) & (b) are microlens array and optical microcavities in micro-optics, respectively. (c) & (d) are biochip and bio-microscaffolds in bio-microsystems, respectively. (a) to (d) are adapted from Ref.[17-20], respectively

Micro-optics is an ensemble of micro-scale optical devices, which is fabricated by using microfabrication technologies [21]. As shown in **Figure 1.1 (a)**, microlenses, enable to shape the light beam in micro scale to achieve engineered focal structure for optical bioassay and cell counting [22, 23]. The profile of microlens can be tailored in fabricating process to meet the requirements of different applications. In addition to conventional spherical profile, aspherical designs or even high-degree freeform designs can be used in application of imaging, illuminating and sensing systems to achieve better focal performance [24-27]. To achieve more compact and dedicated optical systems, advanced microlenses with e.g. lens-on-lens microstructure attract increasing research interest [28].

Optical whispering-gallery-mode (WGM) microcavities, as shown in **Figure 1.1(b)**, are powerful components of bio-microsystems because of their advantages of small volume and low optical loss [29]. These advantages enable WGM microcavities to be a good candidate for on-chip low-threshold laser [30]. Due to the nature of narrow linewidth of laser, optical WGM microcavity lasers are capable to reflect slight changes in resonances and thereby be used for on-chip sensing [31, 32]. Compared with passive optical microresonators which typically use evanescent wave-based methods, optical WGM microlasers can be pumped and collected in relatively easy way and thus be more suitable for on-chip integration [33]. Integrated with functional biochip (Figure 1.1 (c)), the WGM microlasers can be a key part as ultrasensitive biosensors in opto-bio-microsystem which is a compact and portable device for diagnostics.

Micro-components that could create customized *in vitro* microenvironments for cell studies, as shown in **Figure 1.1 (d)**, are another kind of important elements of bio-microsystems [34-37]. To mimic complex *in vivo* microenvironment, 3D microstructures with various physical cues have attracted lots of research interests [38]. Physical cues created by microstructures including topography, roughness, and size can influence the differentiation and proliferation of stem cells [39-41]. The controlled fate of unspecialized cells can develop into specialized cells for certain organ or tissues, which can be utilized in tissue regeneration [42, 43].

To fabricate micro-optics and 3D micro-components, different kinds of fabrication technologies, such as droplet-based technologies, two-photon polymerization, and ion/electron-beam lithography have been demonstrated to overcome the limitations of conventional photomask-based lithography to process biocompatible materials [13, 44-47]. Although the above-mentioned fabrication technologies can fabricate 3D microstructures, they encounter an obstacle to compromise the fabrication speed and resolution [48]. To solve this problem, optical maskless lithography base on spatial light modulator were proposed [49]. The millions of pixels of the modulator and seamless-stitching technology enable to fabricate large-scale microstructures rapidly, and at meanwhile maintain the high-resolution for delicate micro optics [50].

1.2 Research objectives

Although micro-optics and 3D microstructures have been intensively investigated over the past decades, most of preivous works focus on inorganic (e.g. silica and silicon) devices and rely on time-consuming and expensive conventional fabrication technologies. On the other hand, recently developed optical maskless fabrication technology enables rapid fabrication of polymer micro-optics and biocompatible 3D microstrucutres, which thus pave a new pathway for many promising bio-microsystem applications, such as passive optical devices for beam shaping, active optical devices for lasing operation, and 3D microstructures for cell culture study.

In this thesis, two kinds of polymer optical micro-devices and a kind of 3D micro-components are designed and fabricated by using custom-built optical 3D μ-printing technology. Firstly, top-lensed microlenses (TLML) array with engineered profile will be fabricated for advanced beam shaping. Such TLMLs should achieve special focal structures, for instance, elongated focal length or two distinct foci. Secondly, polymer whispering-gallery-mode (WGM) microresonator arrays will be fabricated and then coated with a thin-film of gain material for lasing operation, which can be further used for light-intensity modulation-based biosensors for biomarkers. Lastly, polymer 3D microstructures with in-situ printed bioactive material arrays will be fabricated and can be used in controllable cell culture study.

1.3 Outline of thesis

The chapters of the thesis are organized as below:

Chapter 1: Introduction. In this chapter, the background of micro-optics devices and 3D micro-components are reviewed. The objectives of research are introduced, and then the outline of thesis is presented.

Chapter 2: Overview of optical bio-microsystems. In this chapter, micro-optics devices, such as microlens and polymer WGM resonator laser, are reviewed, and micro-components are summarized. The applications of micro-optics devices and 3D micro-components are also discussed. Optical printing technologies, especially the optical 3D μ-printing technology, are also introduced and discussed.

Chapter 3: Rapid optical μ-printing of polymer top-lensed microlens array. In this chapter, the top-lensed microlens arrays were designed and fabricated by optical μ-printing technology. The fabrication process is described in detail, and the characteristics of profiles and optical properties are compared with the design.

Chapter 4: Optical 3D μ-printed whispering-gallery-mode micro-laser sensors on optofluidic biochips for ultrasensitive detection of vascular endothelial growth factor. In this chapter, whispering-gallery-mode microcavities fabricated by using optical μ-printing technology and coated with a gain layer for low-threshold lasing oscillation are presented. The microlasers are then integrated into an optofluidic chip for ultrahigh sensitive detection of biomarker.

Chapter 5: Direct μ-printing of cellular-scale microscaffold arrays for 3D cell culture. In this chapter, 3D microstructures were designed and fabricated by optical in-situ μ-printing technology are presented. The processes of in-situ printing of 3D selected-bioactivated microstructures are described in full length. The controlled cell behavior on 3D printed microscaffolds are also provided.

Chapter 6: Conclusions and future outlook. In this chapter, the research results are summarized. Future work and development of the project are discussed.

Chapter 2

Overview of Components and Microstructures of Opto-/Bio-Microsystems

2.1 Introduction

In this chapter, fundamentals and recent progress of micro-optics devices and micro-components for bio-microsystems are reviewed. Different types of microlens for light beam shaping are summarized. Whispering-gallery-mode microresonator for lasing operation are reviewed. 3D printed microstructures and their applications in biology are also summarized.

2.2 Microlenses for optical bio-microsystems

2.2.1 Fundamentals and applications of microlenses

Micro-optics is one of important components in modern optoelectronics. It enables the miniaturization and high integration of the optoelectronic devices while maintains characteristics of multifunctionality and energy saving [21, 51]. Microlens plays an important role in micro-optics as it can enhance functions of the microsystem [52-55]. To fabricate microlenses, various materials, such as glass, polymer, liquid crystal, liquid, cells, and protein, as used [22, 56-60]. Polymers are widely used in the fabrication of microlenses because of their characteristics of low cost, biocompatibility and relative good mechanical performance [61].

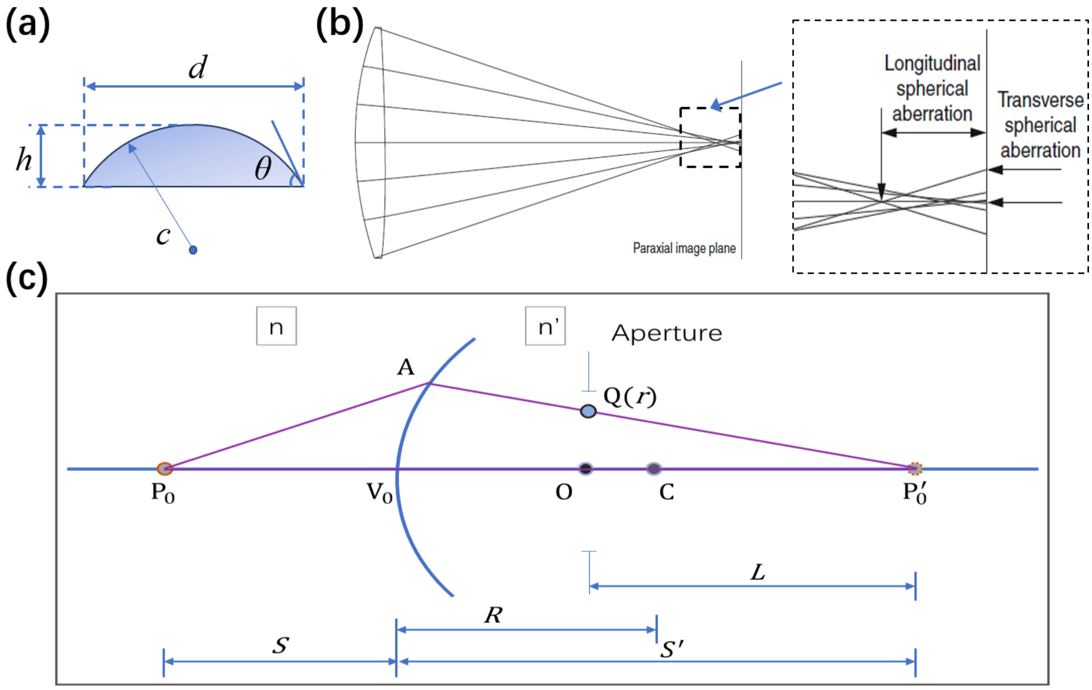

Figure 2.1 Characteristics and aberration of lens. (a) Geometrical parameters of microlens. (b) Positive lens that suffers under-corrected or negative spherical aberration. The inset is close-up view of the image region. (b) is adapted from Ref. [62]. (c) Imaging of an on-axis point P_0 by a spherical surface.

The geometric characteristics of microlens, as shown in **Figure 2.1 (a)**, are usually given by curvature (c), contact angle (θ), diameter (d), height (h), and profile [63]. The quality of microlens can be evaluated by using these characteristics which can be measured by white-light confocal microscopy, confocal laser scanning microscopy, contact profilometry, fluorescence confocal microscopy, scanning electron microscope (SEM), and optical microscopy [64]. Specifically, the profile of microlens with shallow configuration can be measured by contact profilometry and confocal laser scanning microscopy optimally, while microlens with small curvature can be measured by using fluorescence confocal microscopy. For the microlens with thick configuration, white-light confocal microscopy can be used in measurement of the height (*h*) of microlens.

Spherical profile is one of the most commonly used profile. For microlens of a sphere profile, it is on the center of optical axis, while the base locates at the plane which is perpendicular to optical axis [65]. The profile of microlens is widely given by Eq. 2.1,

$$z(r) = -\frac{cr^2}{1+\sqrt{1-(1+k)c^2r^2}} \tag{2.1}$$

where c is the curvature (the reciprocal of the radius), r is the radial coordinate and k is the conic constant. For hyperbolic microlens profile, the conic constant k is less than -1. For elliptical profile, the conic constant k is between -1 and 0. For a spherical profile, the conic constant k is 0. The conic constant k is greater than 0 for oblate ellipsoidal profile.

For an infinite conjugate system, spherical aberration can be described as a variation on focal length, while for the finite imaging system, it can be defined as the variation of aperture [62]. Assume that the paraxial rays go to a focus at the optical axis, the meridional rays which are farther away from the optical axis will go to a focus where is closer to the lens, compared with paraxial rays [66]. As shown in the **Figure 2.1 (b)**, The longitudinal spherical aberration resulting in the marginal rays have a shorter focal length. Similarly, for the transverse spherical aberration, the rays which intercept the paraxial image plane cannot locate at the same point. **Figure 2.1 (b)** shows a typical circumstance of a positive lens with negative aberration. **Figure 2.1 (c)** shows a zoom-in view of the image region of **Figure 2.1 (b)**.

To illustrate the spherical aberration, the schematic of imaging of an on-axis point is shown in **Figure 2.1 (d)**. The object point P_0 locates at the left side of a spherical surface with distance *S*, where the refractive index is n. The imaging point P'_0 locates at the right side of the surface with distance *S'*, where the refractive index is *n'*. The vertex of the spherical surface is V_0, while C is the center of curvature, and *R* is the radius of curvature (*c*) of the surface. The aperture, which is also an exit pupil here, locates at the left side of imaging point P'_0 with distance L which is defined to be positive at this situation. O is the center of the aperture. Point *Q* locates the plane of exist pupil with the distance of *r* from the center of the aperture.

The chief ray for the object point P_0 is ray $\mathrm{P_0V_0P'_0}$ which pass through the center of the aperture O. The aberration between the chief ray $\mathrm{P_0V_0P'_0}$ and the incident ray passing the point *A* on the spherical surface and point *Q* is given by [67]

$$W(A) = [P_0 A P_0^{'}] - [P_0 V_0 P_0^{'}] \tag{2.2}$$

where the square brackets are the optical path length. If the refractive surface is a totally aberration free surface, rays which pass through any point on the surface will be converged on the same point of the chief ray, otherwise the scattered spot diagram will be observed at the imaging plane [68]. According to the aberration theory, the on-axis spherical aberration $W_s(A) \equiv W_s(Q)$ is given by [67]

$$W_s(r) = -\frac{n'(n'-n)}{8n^2}(\frac{1}{R}-\frac{1}{S'})^2(\frac{n'}{R}-\frac{n+n'}{S'})(\frac{S'}{L})^4 r^4 . \tag{2.3}$$

Compared with above-mentioned spherical surface, a conic surface with conic constant *k* have additional aberration ΔW_c for the on-axis point P_0, which is given by [67]

$$\Delta W_c = -\frac{(n'-n)k}{8R^3}(\frac{S'}{L})^4 r^4 . \tag{2.4}$$

As shown in equation 2.3, one can see that, for a situation of real imaging, the spherical aberration is a negative value. To eliminate the negative spherical aberration, one of the common methods is to use a conic surface with negative conic constant *k*, in which the conic aberration can compensate the spherical aberration. Moreover, by tailoring the conic surface, the controlled aberration can be used in advanced light beam shaping.

Light beam shaping by microlens can be widely used in packaging for isotropic emission light source, such as light-emitting diodes and quantum dots [69, 70]. As shown in **Figure 2.2 (a)**, PDMS microlens arrays were attached on the surface of the organic light-emitting diodes (OLED), which lead to an efficiency boost up to 34% [71]. **Figure 2.2 (b)** shows that microlens with the optimized profile were used to enhance the output power of ultraviolet LED [72]. To achieve single-photon sources with high photon-extraction efficiency, Sarah *et al.* fabricated a GaAs microlens on quantum dots light source, and further *in-situ* printed a complex microlens upon the light source (**Figure 2.2 (c)**) [73]. The novel design enables high photon-extraction efficiency of 40%, which is important for the field of quantum communications. Besides the enhanced light extraction, as shown in **Figure 2.2 (d)**, microlens can also modify properties of quantum dots, such as spectral shift, and change of binding energy [74].

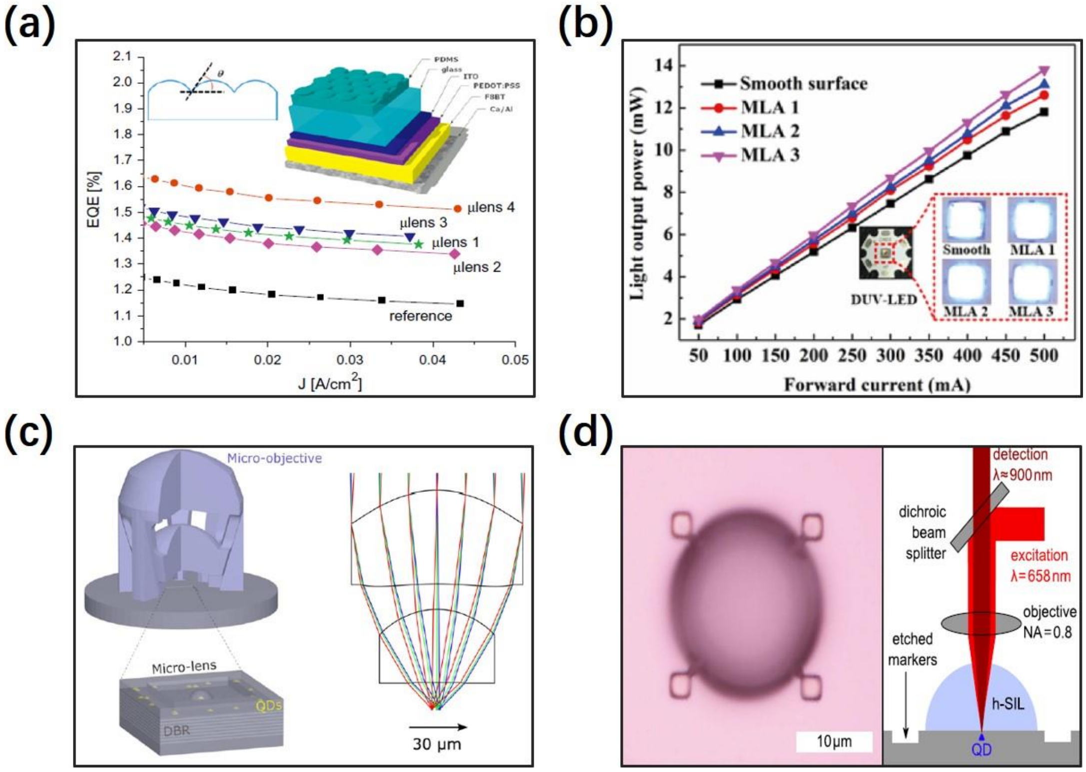

Figure 2.2 Microlens for light beam shaping to enhance the efficiency for (a) OLED, (b) ultraviolet LEDs, (c) quantum dot light source, and (d) quantum dot spectroscopy. (a) to (d) are adapted from Ref. [71], [72], [73], and [74], respectively.

Optofluidic system with integration of microlens provides novel on-chip optical detection and adaptive imaging approaches. As shown in **Figure 2.3 (a)**, Lv *et al.* fabricated a dual channel microfluidic chip in which a hydrogel microlens was in-situ fabricated in one channel [9]. As the hydrogel response to concentration of salt solution, the tunable microlens can be achieved, which were used in adaptive imaging. Beside the stimulus responsive materials, stable materials, such as glass, can also be utilized for fabrication of tunable microlens with the help of optofluidic chips. Due to the different etching speed between the exposed/non-exposed glass, the glass microlens, as shown in **Figure 2.3 (b)**, can be fabricated and integrated into an optofluidic chip [75]. By injection of fluidic of different refractive index, the focal length can be tuned, which can be used for adaptive imaging. In **Figure 2.3 (c)**, microwell template with spherical microlenses was integrated into an optofluidic channel [76]. The small focal points of the microlens enable to detect nano particles by detecting the back scattering light, in which the optical signal can be enhanced up to a factor of 40 by the focal point of the microlens. In **Figure 2.3 (d)**, Yang *et al.* proposed to use spherical microlens to enhance the fluorescent signal of specific protein, e.g. mouse IgG, in which the detection limit was down to 2 ng/mL [77]. Microlens can also be used for single biomolecule imaging (**Figure 2.3 (e)**). With traditional methods, single biomolecule can only be imaged by objectives with high numerical aperture and index-matching liquid, which cannot operate at high temperature, such as 70 °C.

The TiO_2 spherical microlenses were demonstrated to couple light to the surface with biomolecules and enable to monitor the real-time single-biomolecules kinetic under high temperature (70 °C) [78].

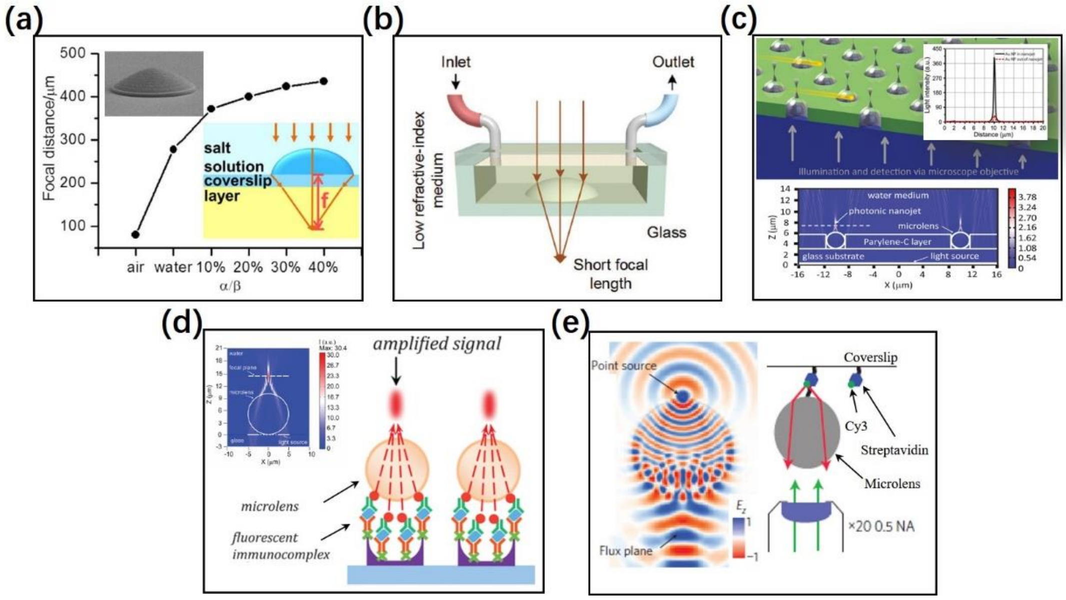

Figure 2.3 Microlens in optofluidic systems. Hydrogel microlens (a) and glass microlens (b) for tunable focal length. (c) Microlens array for nanoparticle detection. (d) Microlens for enhancing signal of immunoassays. (e) Microlens for imaging of biomolecules. (a) to (e) are adapted from Ref. [9], [75], [76], [77], and [78], respectively.

2.2.2 Integration of polymer microlenses into bio-microsystems

Due to the characteristics of miniaturization and facile beam-shaping ability, microlens is attracting in optical detection in bio-microfluidic system, which can significantly enhance the signal-to-noise ratio compared to traditional methods [79]. As shown in **Figure 2.4 (a)**, Wu *et al.* first printed microlens arrays in an embedded microfluidic channel in 2015, which enables to carry out cell detection and counting simultaneously in a wide microfluidic channel without additional coupling steps [56]. For further improve the success rate of cell counting, microlens array were fabricated in a set of center-pass unit in a microfluidic channel, as shown in **Figure 2.4 (b)**, and 100% success rate was achieved by this method [80]. Imaging of cells in flowing environment is one of the most important rapid analysis methods. For fast analysis of cell, microlens arrays with appropriate focal length, as shown in **Figure 2.4 (c)**, were embedded in microfluidic channel so as to determine up to 50,000 cells per second [81].

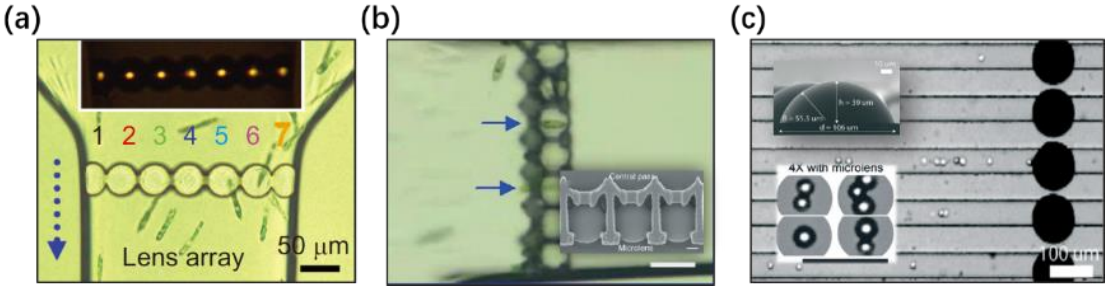

Figure 2.4 Microlens for application of optical detection of cells. (a) Microlens array were integrated in microfluidic chip for cell detection. (b) Microlens array with center-pass scaffold for high success rate cell counting. (c) Microlens array for parallel imaging flow cytometry. (a) to (c) are adapted from Ref. [56, 80, 81], respectively.

2.3 WGMR laser sensors for optical bio-microsystems

2.3.1 Fundamentals of WGM resonators

Whispering-gallery modes were first observed in the dome of St. Paul's Cathedral in London and attract research interest in acoustic domain at first [82]. In the domain of optics, whispering-gallery modes is a kind of electromagnetic modes with high angular momentum. In these modes, light propagate along the rounded surface due to the total internal reflection at a certain phase condition.

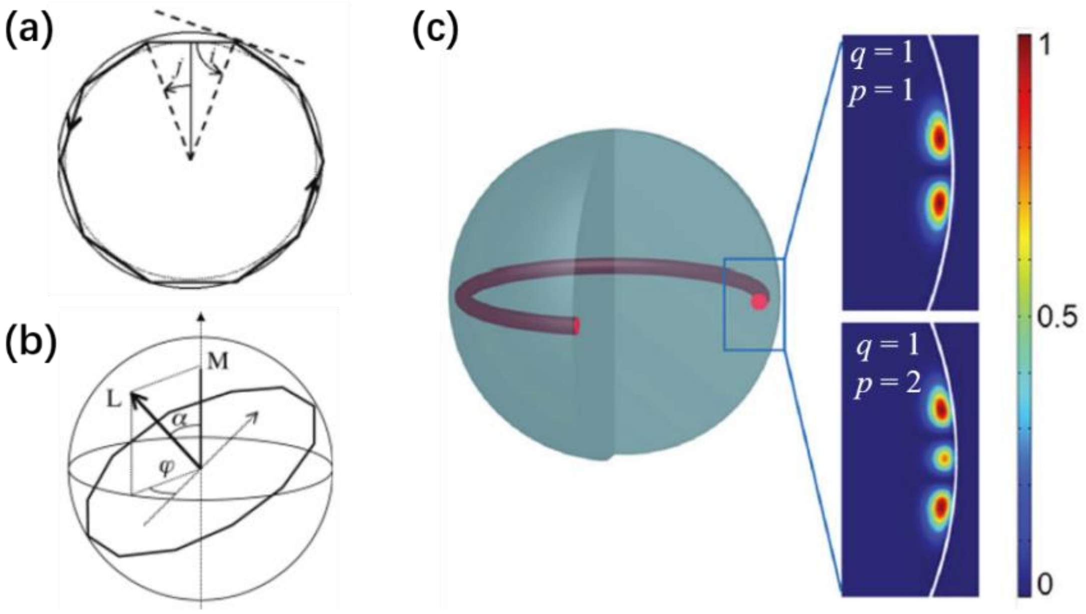

Figure 2.5 Schematic of (a) light propagation in a circle by total internal reflection, (b) angular momentum L in WGMs. (c) Electric field distribution of whispering-gallery-mode with different angular mode number p. (a) and (b) are adapted from Ref. [83]. (c) is adapted from Ref. [84].

In **Figure 2.5 (a)**, a ray of light propagates within a microsphere with refractive index n, radius a, and the incident angle of the ray is i. According to Snell's law [85], total internal reflection occurs when the incident angle is under condition of $i > i_c = \arcsin(1/n)$. Due to symmetric characteristic of a microsphere, the incident angle will not change during propagation of ray, which means light is trapped in the microsphere. For a trapped ray that propagates near the surface of the microsphere, a standing wave will occur if the round distance meets the following condition,

$$2\pi a \approx \ell(\frac{\lambda}{n}) \tag{2.5}$$

where λ is the wavelength in vacuum, and ℓ is the number of wavelengths (integer). This condition is resonance condition. Number of wavelengths ℓ can be identified by angular momentum as shown in **Figure 2.5 (b)**. The momentum of a photon in **Figure 2.5 (a)** is given as [83]

$$p = \hbar k = \frac{\hbar 2\pi n}{\lambda} \tag{2.6}$$

where k is the wave number, and $\hbar$ is reduced Planck constant. If the incident angle meets the condition $i \approx \pi / 2$, the angular momentum is given as [86]

$$L \approx ap = \frac{a 2\pi \hbar n}{\lambda} = \hbar \ell \tag{2.7}$$

According to Maxwell's equations, spherical harmonic functions and spherical Bessel functions can be used to depict electromagnetic field distribution of whispering-gallery-mode in spherical resonators[87]. Lame coefficients can be neglected in the equations, because the modes near the equatorial plane and the surface of sphere [88, 89]. The electric field amplitudes are approximated by [90]

$$E \propto e^{-\frac{1}{2}(\frac{\alpha}{\alpha_\ell})^2} \cdot H_p(\frac{\alpha}{\alpha_\ell}) \cdot e^{i\ell\varphi} \cdot Ai(\frac{r}{r_\ell} - \xi_q), \tag{2.8}$$

$$\alpha_\ell = a^{\frac{3}{2}} \ell^{-\frac{1}{2}}, \tag{2.9}$$

$$r_\ell = (\frac{a}{2})^{\frac{1}{3}} \ell^{\frac{2}{3}}, \tag{2.10}$$

where r is the distance to the surface of sphere, φ is azimuth angle, and α is polar angle from the equatorial plane. $H_p(x)$ is the Herimitian polynomial of degree p. $Ai(x)$ is Airy-function, while $\xi_q > 0$ is the q-th root of when Airy-function is equal zero. From the above-mentioned result in sphere, the whispering-gallery-modes can be mainly described by three factors: angular number p, azimuthal mode number ℓ, and radial mode number q. The radial mode number q ($q \geq 1$) determines the number of electrical maximums along the radial direction of the equatorial plane in a sphere. The azimuthal mode number ℓ ($\ell \gg 1$) is the number of wavelengths, which is discussed in Eq. 2.5. Typically, angular mode number $p = \ell - m$ is utilized to represent the number of field oscillation in α direction, as shown in **Figure 2.5 (c)**. The polar mode number m ($m = -\ell, -\ell + 1, \ldots, \ell$) represents the direction of wave circulation around the equatorial plane and corresponding wave numbers.

Mode volume of whispering-gallery-mode can be utilized to describe the spatial confinement of optical microcavities [91]. The optical mode volume V_m in microcavity is determined by [92]

$$V_m = \frac{\int_{V_Q} \varepsilon(\vec{r}) \left|\vec{E}(\vec{r})\right|^2 d^3\vec{r}}{\left|\vec{E}_{\max}\right|^2}, \tag{2.11}$$

where $|\vec{E}|$ is electric field strength and V_Q is a quantization volume of electrical field. In calculation, the cross section of V_Q should be chosen to cover the field distribution until the choice of the cross section only cause marginal difference to the final result [93].

The temporal confinement of optical microcavities can be described by quality factor of the mode (Q factor) [91]. Q factor characterizes the time τ that an optical resonator can keep energy in. Q factor is defined as:

$$Q = \frac{\omega}{\Delta\omega} = \omega\tau \tag{2.12}$$

where $\Delta\omega$ is the full width at half maximum (FWHM) at corresponding resonance wavelength. For an uncoupled whispering-gallery-mode microresonator, the intrinsic Q factor is given by [94]

$$Q_0^{-1} = Q_{rad}^{-1} + Q_{mat}^{-1} + Q_{s.s}^{-1} + Q_{cont}^{-1} \tag{2.13}$$

where Q_{rad}^{-1} represents Q factor limited by intrinsic radiative losses (related to the curvature of microcavity), Q_{mat}^{-1} denotes the absorption in material itself, $Q_{s.s}^{-1}$ is scattering losses (related to surface roughness), and Q_{cont}^{-1} is the losses by surface contaminants, such as atmospheric water on surface [94]. The intrinsic radiative losses are typically very small, and Q_{rad} is larger than 10^{11}, when $D/\lambda \gg 15$ [83]. By using appropriate materials, processing method, such as thermal reflow, and clean testing environment, the Q factor of whispering-gallery-mode microresonators can be up to 10^8 [95-97].

A particular advantage of WGM microresonators is that it has not only high Q factor but also relatively small mode volume [98, 99]. A high Q/V_M ratio means that a tightly-confined mode exists in the microcavity, which enable strong interaction between light field and objects on the microcavity [100]. If the active material was doped inside the microcavity, the strong interaction will enable low-threshold laser operation [30].

2.3.2 Polymer WGM resonator lasers

Polymers have advantages including low cost, easy processing, and versatility in structure and thus are becoming very appealing in fabrication of microresonators in the past decades. Various fabrication technologies have been reported for fabrication of polymer optical WGM microresonators, such as molding method, mechanical polishing method, surface-tension based technique, two-photon / multi-photon polymerization technique, and optical 3D μ-printing technology [101-105].

Active materials, such as organic dyes and quantum dots, can be doped into polymer host matrix or coated on the polymer microresonators as a gain layer directly [106]. As shown in **Figure 2.6**, laser emission has been demonstrated in various polymer microresonators, such as microspheres, microrings, microdisks, and microgoblet microresonators [107-110].

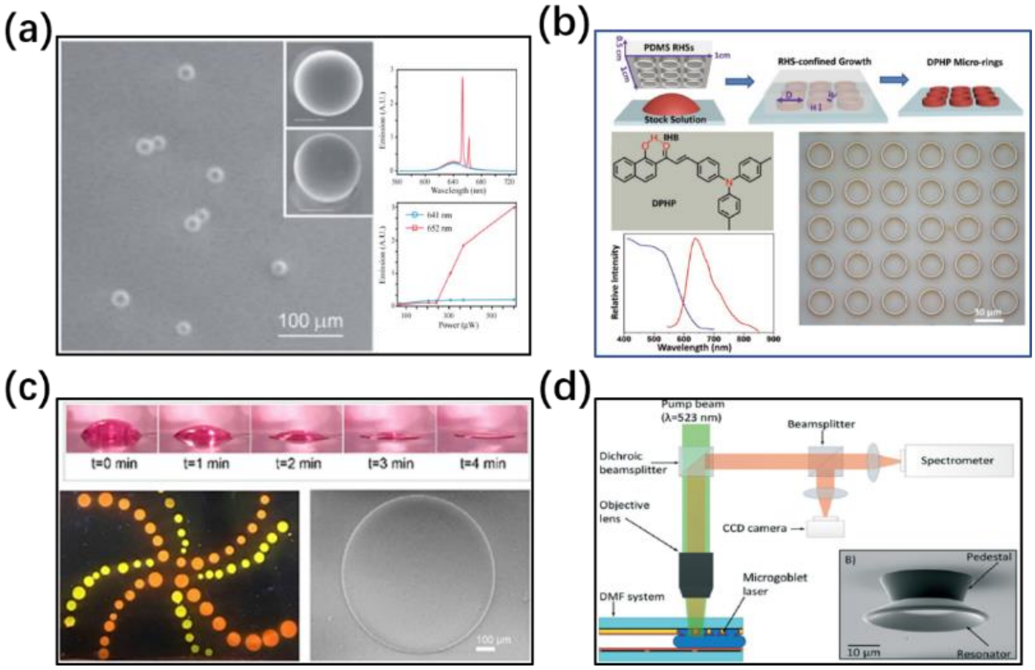

Figure 2.6 Polymer microresonator lasers. (a) Microsphere resonators made by semiconductor nanocrystal sol. (b) Microring resonator array fabricated by DPHP. (c) Microdisk resonator made by rhodamine doped protein and PVP. (d) Dye-doped PMMA Microgoblet resonator. (a) to (d) are adapt from Ref. [107], [108], [109], and [110], respectively.

Typical protocol for fabrication of organic spherical whispering-gallery-mode microresonator, as shown in **Figure 2.6 (a)**, is deposition of polymer on silica microsphere[107]. The silica microsphere can be synthesized via the base-catalyzed hydrolysis of tetraethyl orthosilicate (TEOS) [111]. In **Figure 2.6 (b)**,the microring resonator is made up of PH sensitive organic gain material in near infrared spectrum directly by using stamping technology [108]. Due to the high photoluminescence quantum yield of 11.26% and high-quality factor of 8.8×10^2, the lasing threshold can be achieved at 65 μJ cm^{-2}. As shown in **Figure 2.6 (c)**, the biomaterials, such as silk fibroin and PVP, can also be used in fabrication of microdisk laser [109]. The self-assembled methods enable them to fabricate microdisk laser in one step without high processing temperatures or toxic precursors which will damage the biomaterials. For further improve the *Q* factor, the microgoblet whispering-gallery-mode resonator with suspended component were fabricated [110]. In **Figure 2.6 (d),** Organic dye-doped Poly(methyl 2-methylpropenoate) (PMMA) was used to fabricate the suspended goblet component. The *Q* factor was reported as high as 3×10^5, while the lasing threshold can be boosted to be 0.54 nJ per pulse.

2.3.3 Applications of WGM laser sensors

Whispering-gallery-mode resonators are suitable for sensing applications because that resonant condition depends on both the refractive index of surrounding media and the geometry of the microresonator [112].

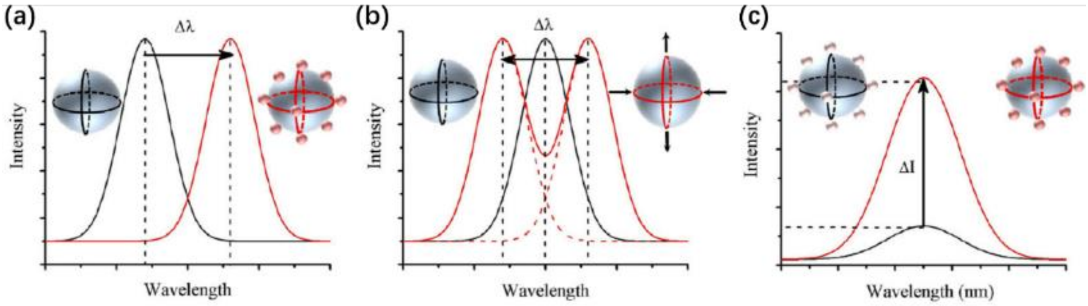

Figure 2.7 Sensing mechanisms of microresonator lasers. (a) Resonant wavelength shift. (b) Mode splitting. (c) Change in mode intensity. Adapted from Ref. [113].

WGM resonator lasers have attracted lots of research interests in ultrasensitive sensing application, because the narrow linewidths of the microlasers can indicate slight changes of resonant wavelength, while it is hard for passive microresonators to resolve that slight changes [31, 114]. It is been reported that the whispering-gallery-mode resonator lasers can be utilized for sensing of humidity, pressure, electric fields, temperature and biological objects [115-119].

In **Figure 2.7**, several sensing mechanisms of whispering-gallery-mode resonators were demonstrated. Tracking the shift of resonant wavelength ($\Delta\lambda$), as shown in **Figure 2.7 (a)**, is one of the most common sensing methods, because $\Delta\lambda$ is proportional to the change of effective radius of the microresonators which can be influenced by change of the refractive index inside or near the surface of microresonator, or by expansion or compression caused by change of temperature or other isotropic mechanical force. If an anisotropic force is applied to microresonators, as shown in **Figure 2.7 (b)**, the deformation of microresonators will lead to mode degeneracy and finally induce splitting of resonant wavelength which is prominent within microresonator lasers [120]. The previous two sensing mechanisms rely on the fine resolution of the spectrometer or momochromator, which prevent people from developing low-cost and portable opto-biochip. However, the method based on measurement of intensity, as shown in **Figure 2.7 (c)**, has great potential in effective platform for biosensing platform, which relies on the absorption of microlaser light or interaction between gain material and sensing molecule [121].

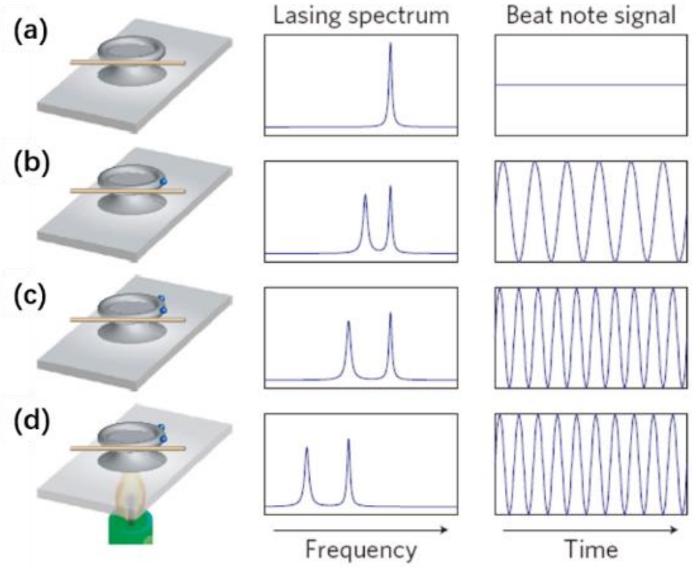

Figure 2.8 Schematics of nanoparticles detection by lasing mode splitting and beat note signal. (a)-(c) Spectrums of 0-2 nanoparticles. (d) Spectrum temperature fluctuations. Adapted from Ref. [31]

Another mechanism for realization of mode-splitting detection, as shown in **Figure 2.8**, bases on standing wave modes [31, 100, 122, 123]. A particle attached on the outer profile of whispering-gallery-mode microresonator will cause the scattering of light which will be coupled into whispering-gallery-mode. The original mode and counter-propagation mode will create two standing wave modes, by which particle size down to tens of nanometers can be detected by this self-reference method [31, 124]. In **Figure 2.8 (a)-(c)**, the laser beat note signals are extracted by fast Fourier transform of the laser spectrums. Besides the advantage of high sensitivity, another advantage of the method, as shown in **Figure 2.8 (d)**, is resistant to environment noise, such as temperature fluctuations, because such a noise will shift the splitting modes simultaneously.

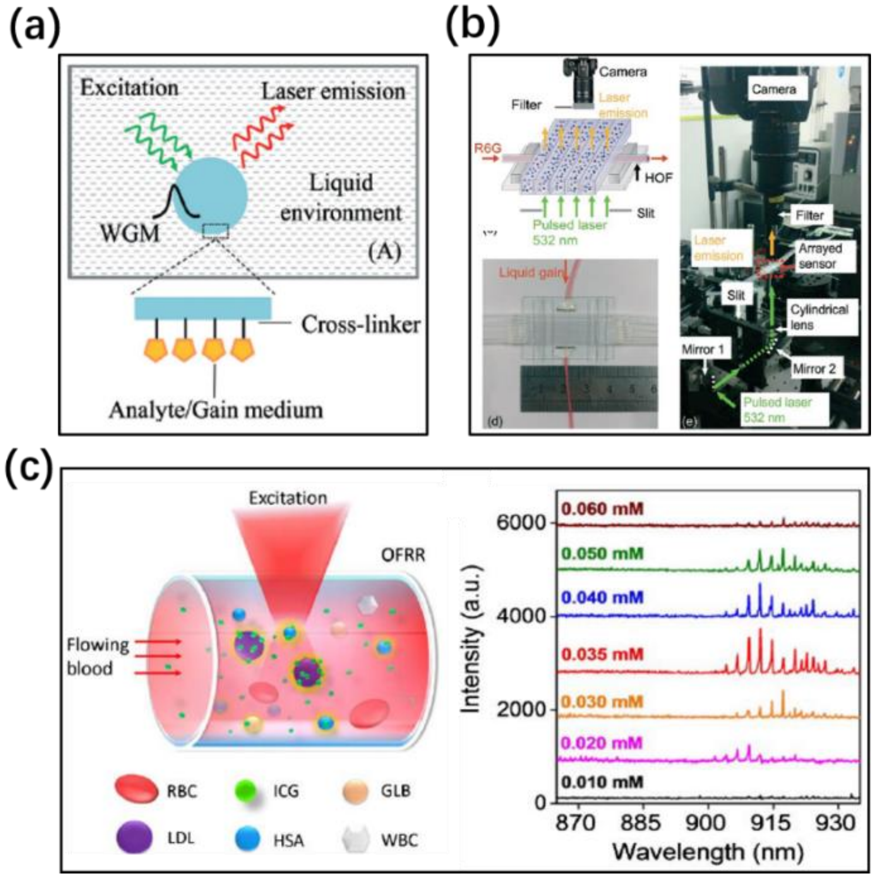

Figure 2.9 Laser intensity-based biosensors. (a) WGM microlaser for detection of DNA. (b) Optofluidic laser for sensing of HRP. (c) ICG laser for detection of serological component. (a) to (c) are adapted from Ref. [18, 125, 126], respectively.

Figure 2.9 shows a series of laser-intensity based biosensors. Chen *et al.* immobilized a layer of crosslinker (BS^3), as shown in **Figure 2.9 (a)**, on the surface of single mode fiber (SMF) which can be further be functionalized streptavidin for DNA detection [18]. Due to the quenching effect between Cy3- and Cy5- labeled DNA, the DNA sensing can be realized by measuring the intensity of laser. The one of the advantages of intensity-based sensor is no need of expensive monochrometer, as shown in **Figure 2.9 (b)**. Horseradish peroxidase (HRP) is a kind of protein which will generate certain color when it was mixed with 3,3′,5,5′-tetramethylbenzidine (TMB) [127]. A commercially available camera was used to measure the intensity of laser which is attenuated by the mixture of HRP and TMB [125]. The limit of detection can be as low as 14 pM HRP. In **Figure 2.9 (c)**, Chen et al. used Indocyanine green (ICG) as the gain material, which is responsive to serological components (albumins, globulins, and lipoproteins), in a silica capillary [126]. They found that the laser intensity will change according to the change of concentration of the components, which can be further used in biosensing applications.

2.4 Micro-components for bio-microsystems in cell study

To achieve a multifunctional opto-bio-microsystems, micro-components are of great potential in integration with micro-optics so as to process biological sample or provide a novel cell culture environment. For better understanding of diseases and drugs, investigation on cellular and molecular has been developing rapidly over the past two decades [128]. However, there are two problems for traditional methods to investigate such biological systems. The first one is that culturing many kinds of cells with heterogeneous physiological states will affect the accuracy of diagnosis or analyzing, because of intrinsically different gene expression

[129]. The second one is that for statistical data of multiple parameters, large number of samples should be tested, which requires the complex technologies to have high throughput [130]. Bio-microsystems are good candidates for biological investigation with limited reagent consumption [131].

2.4.1 2.5D microstructures for cell separation

Compared with 3D structures, 2.5D structures have no suspended elements in the vertical dimension. Cell separation is of great importance as a prerequisite in many applications.[132-134] Cell manipulation without chemical, or electrical, or magnetic methods is important in many fields in biology, because the methods may affect the states of the cells [129]. 2.5D microstructures in bio-microsystems can be used to manipulate cells, which play an irreplaceable role in cell isolation and cell trapping.

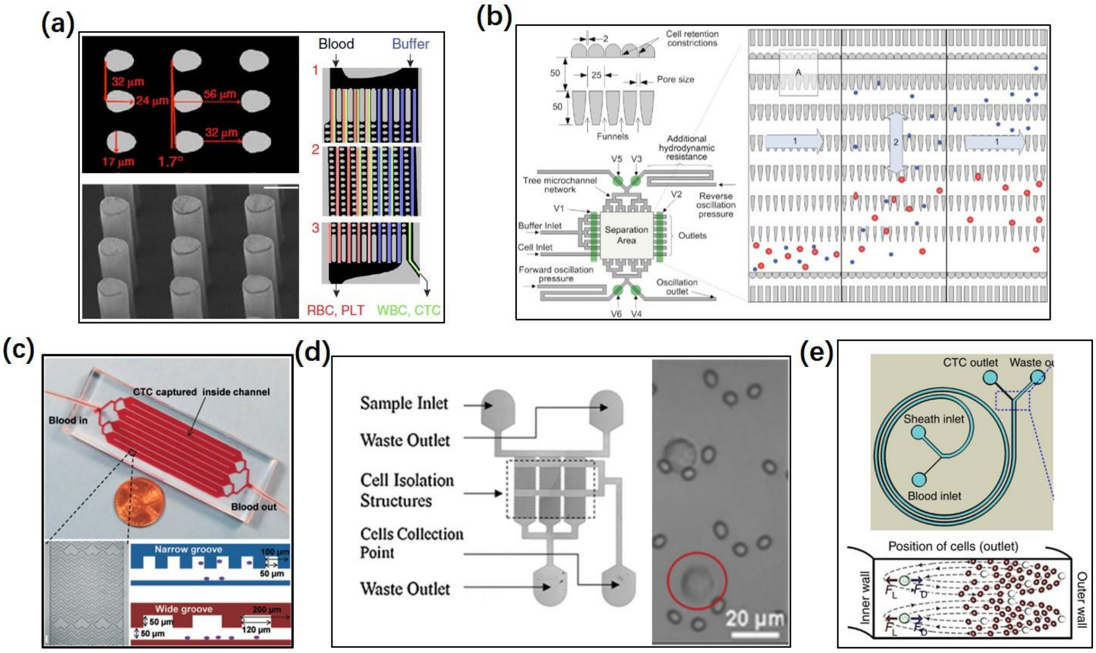

Figure 2.10 2.5D microstructures in bio-microsystems for cell manipulation. (a) 2.5D micropillars with design of deterministic lateral displacement (DLD) for isolation of circulating tumor cells (CTCs). (b) Microstructures for cell separation by using structural ratchet mechanism. (c) Geometrically enhanced mixing (GEM) microstructures for high-efficiency CTC trapping and separation. (d) The micropillars for separation of CTCs. (e) Spiral microfluidic channels for separation of CTCs. (a) to (e) are adapted from Ref. [134], [135], [136], [137], and [138], respectively

As shown in **Figure 2.10 (a)**, Karabacak and co-workers develop a biochip with micropillars array for separation of nucleated cells from whole blood [134]. The micropillars array were arranged according to deterministic lateral displacement (DLD) in which the key parameter is critical deflection diameter [139]. The critical deflection diameter determines the minimum hydrodynamic diameter of the particles which will be deflected by the micropillars array. For DLD arrays, three parameters can influence the critical deflection diameter, which are gap between adjacent micropillars in horizontal axis, row shift fraction and geometrical factor. As the dimension of circulating tumor cells (CTCs) and other blood cells are different, the CTCs can be isolated from whole blood.

In **Figure 2.10 (b)**, microstructures with microfluidic ratchet mechanism were fabricated for cell separation by using oscillatory flow [135]. The shape of micro funnel was designed to be parabolic, which can balance the length of microstructures and cell compression levels. When the microstructures are longer, there are more risks that cell clogging happens. The cell compression levels are highly related to cell damage. Compared with traditional cell filtration, the microstructures with furry design have advantages in lower selectivity and avoiding cell accumulation.

For high-efficiency of capture CTCs, the Geometrically enhanced mixing (GEM) microstructures, as shown in **Figure 2.10 (c)**, were utilized in a biochip [136]. The herringbone microstructures were optimized to disrupt streamlines effectively so as to generate microvortex, which enhance the interaction between CTCs with surface of microstructures. The surface of microstructures were functionalized by biotinylated anti-EpCAM, which can capture CTCs specifically so as to isolate CTCs from blood cells.

As shown in **Figure 2.10 (d)**, the bio-rheological differences in the cell size and deformability was used for separation of CTCs from blood cells.[137] The trap made up of 2.5D micropillars can distinguish the bio-rheological differences and keep the CTCs in microfluidic channel. The 2.5D spiral microfluidic channels, as shown in **Figure 2.10 (e)**, can be also used to separate CTCs, which based on inertial and Dean drag forces in microfluidics[138]. The advantages of this technique include high throughput and simpler fabrication process.

2.4.2 3D microscaffolds for investigation of cell culture and behavior

Polymer 3D microstructures with engineered geometry by optical printing technologies enable a lot of meaningful applications in the field of mechanobiology [140, 141]. These applications involved measurement of cell force on 3D microstructures, cell migration and motility, and cell proliferation and differentiation on 3D environment [142-144].

To estimate cell force in *in vivo* environment, one of the methods is to measure the cell force on 3D microstructures, which can be realized by measuring the change of the geometry of the 3D microstructures caused by cell force [145]. In **Figure 2.11 (a)**, Klein *et al.* uses TPP technology to fabricate the 3D suspended spider-web like microstructures and investigated the contractile forces of cardiomyocytes which is around 50 nN on the microstructures [142]. This method can be also extended to other cells, such as mouse embryonic kidney fibroblast cell. In **Figure 2.11 (b)**, 3D micro flowers with selectively functionalized patterns were fabricated by photomask lithography and material shrink [44]. Different from the microstructures with homogeneous material, cells tended to attach on the functionalized area which enables the force measurement to be more precise and easier.

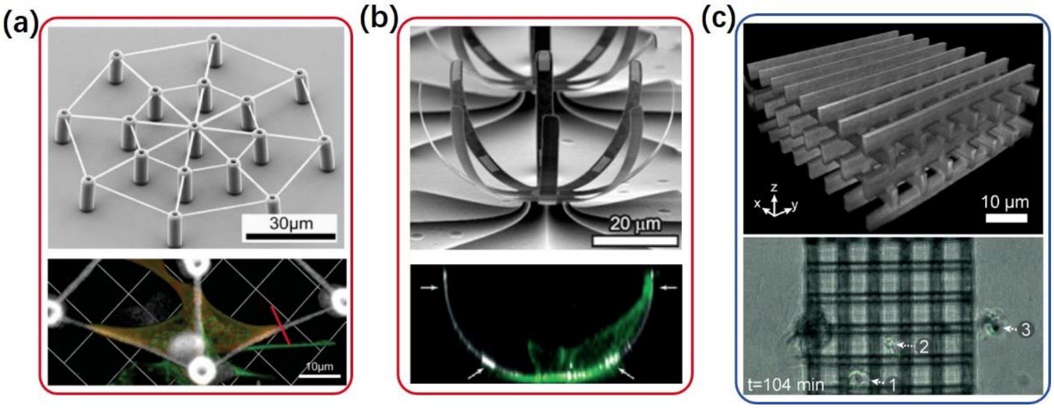

Figure 2.11 Optical-printed 3D microstructures used in investigation of cell behavior. (a) cobweb-like microstructures and (b) micro "flowers" for cell force investigation. (c) 3D matrix for cell mobility investigation. (a) to (c) are adapted from Ref. [44, 142, 146], respectively.

The 3D networks in **Figure 2.11 (c)** can be integrated into microfluidic channel, which was utilized to investigate cell motility of mature human dendritic cells [146]. It is found that smaller pore dimensions in the 3D network can enhance the cell motility and have higher probability to move across the network at least one turn.

By resembling the environment of native cartilage, the 3D networks in **Figure 2.12 (a)** can enhance the cell proliferation, which shows significantly improved performance of implantation[147]. Besides the 3D networks, complex 3D microstructures can also be applied to influence the rearrangement of actin and adhesion of cell, which can influence the cell proliferation by controlling the physical cues [148]. In **Figure 2.12 (b)**, pillars in square and hexagonal arrangement connected with rods were fabricated to investigate how 3D structures influence cell proliferation and differentiation. Judith *et al.* found that cell proliferation was enhanced by 25 μm spaced pillars regardless the type of arrangement, i.e. hexagonal and square [148].

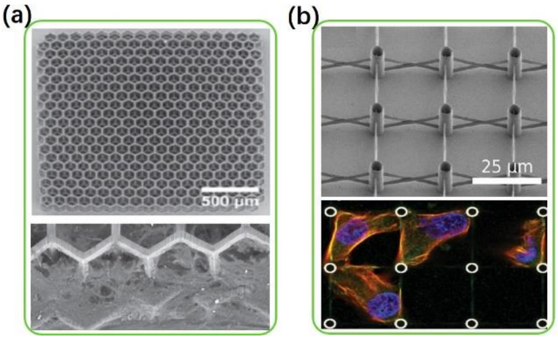

Figure 2.12 Optical-printed 3D microstructures used in investigation of cell culture for (a) implantation and (b) proliferation, which are adapted from Ref [147] and [148], respectively.

To create complex interaction between cells and microstructures and resemble the physiological interactions cells and extracellular matrix better, materials engineering and functionalization are utilized in the process of fabrication of 3D microstructures [149, 150].

In 2011, Franziska *et al.* utilized two kinds of materials (i.e. bioinert material, mixture of polyethylene glycol diacrylate (PEGDA) and pentaerythritol triacrylate (PETA); bioactive material, OrmoComp) in fabrication of the functionalized 3D microstructures [151]. As main part of the scaffold made by PEGDA-PETA mixture was protein-repellent material, as shown in **Figure 2.13 (a)**, cells tended to bind on the OrmoComp micro cubes which were functionalized with fibronectin. Besides the materials engineering, advanced functionalization technique can also be integrated into 3D microstructures. In 2017, Richter *et al.* demonstrated that, as shown in **Figure 2.13 (b),** the photoenol polymer network can be activated by UV irradiation, which eventually made the two of the beams on microstructures bioinert. These selectively functionalized 3D microstructures enable to investigate influence of spatial distribution of ligand and mechanical cues on cell behavior [152].

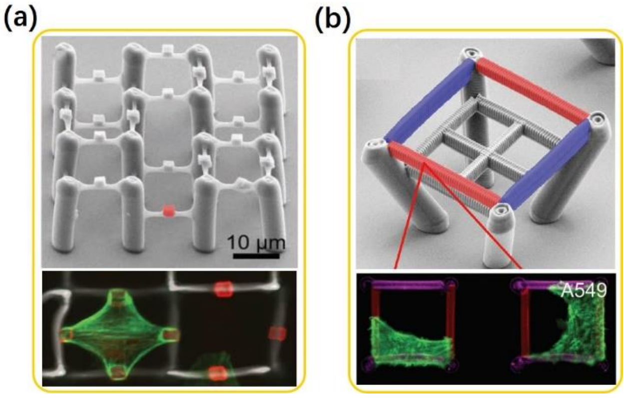

Figure 2.13 Optical-printed 3D microstructures used in investigation of cell culture for selective 3D cell spreading on (a) fibronectin-modified structure and (b) ligand-modified structure, which are adapted from Ref [151] and [152], respectively.

2.5 Optical printing technologies for 3D microstructures

3D micro printing technologies have advantage in fabricating relatively complex 3D microstrucutres easily and directly with aid of computer, while the conventional fabricating methods rely on molds and masks. To unleash the great potential of additive manufacturing in biological application, polymer, as a biocompatible material, attractive vast research interests in fabrication of 3D microstructures.

2.5.1 Fabrication technologies for 3D microstructures

For fabrication of 3D polymer microstructures, the most commonly technologies based two strategies, i.e. light and ink [13, 153]. In 3D micro printing, the basic mechanism is that a stage controlled by computer move a pattern generator which can be ink-based print head or optical engine, as shown in **Figure 2.14**, and enable to generate the pattern of designed structure layer-by-layer.

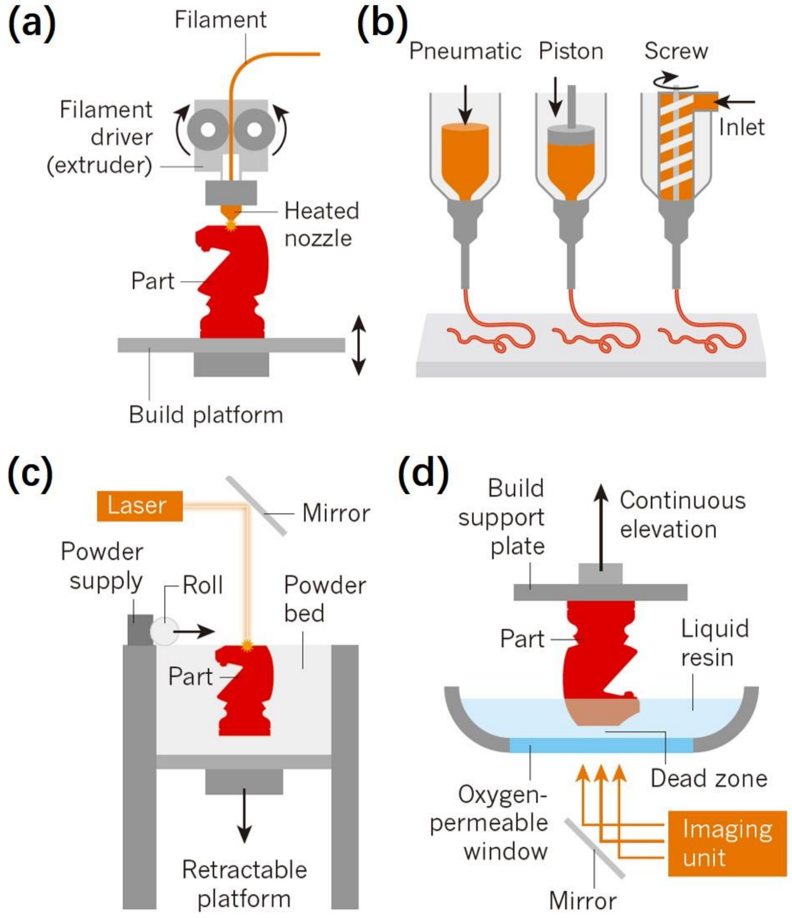

Figure 2.14 Schematics of ink-based 3D fabricating technologies and optical engine-based fabricating technologies. Ink-based technologies: (a) fused deposition modelling and (b) direct ink writing. Optical engine-based technologies: (c) selective laser sintering and (d) stereolithography. Adapted from Ref. [154].

Compared with optical-engine based fabricating methods, as shown in **Figures 2.14 (a) & (b)**, the advantage of ink-based fabricating technologies not only can use photopolymerizable material, but also can utilize thermoplastic polymers and thermoset polymers. The basic concept of ink-based printing technology is that the printheads scan and deposit ink according to each layer of 3D models. Several ink-based technologies refer to this concept, such as binder jetting printing, direct inkjet printing, and hot-melt printing [155-157]. In **Figure 2.15,** the feature size of the ink-based technologies (below the horizontal line) is from several of micrometers to a few hundred micrometers. Unlike fused deposition and photocurable method, the ink-based direct-write technologies for 3D microstructures mainly based on the solvent evaporation so that the dried ink can support itself, whose resolution highly depends on properties of inks [158].

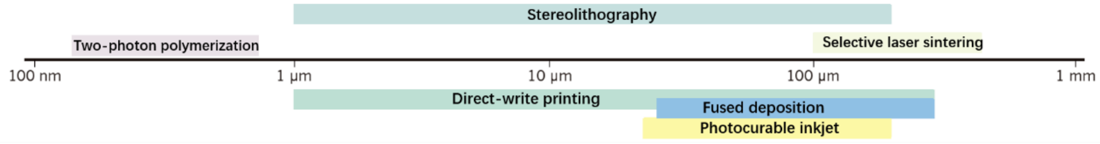

Figure 2.15 Minimum size range of pattern features fabricated by optical engine-based and ink-based 3D fabricating technologies. Adapted from Ref. [154].

For selective laser sintering technology, as shown in **Figure 2.14 (c)**, the polymer powders in a powder bed are sintered by laser point-by-point and form the patterned layer [159]. After a layer is fabricated, additional powder will be added on the powder bed in which the non-sintered powders are used as supporting material of the structure. The resolution of the technology is typically around 100 micrometers which is a few times larger than the size of the powder.

The first fabricating mechanism based on optical engine to sculpt 3D microstructures is stereolithography of photo sensitive polymer [160]. In stereolithography, as shown in **Figure 2.14 (d)**, the prepared polymer is selectively photopolymerized layer-by-layer. Each layer is polymerized in locally illuminated regions. Some newly developed technologies also refer to this basic concept, such as digital light processing (DLP)-based printing technology, two-photon polymerization (TPP) technology, and continuous liquid interface production (CLIP) technology [161-165]. In the DLP-based printing technology, optical patterns are projected on the prepared polymers which is polymerized lay-by-layer and finally realize 3D printing.

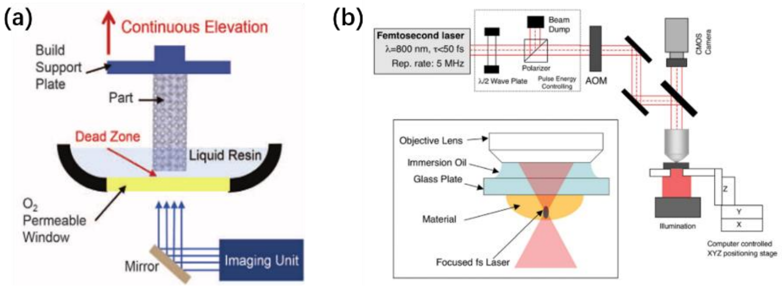

Figure 2.16 Optical 3D fabrication technology. (a) Continuous liquid interface production (CLIP) technology. (b) two-photon polymerization (TPP) technology. (a) and (b) are adapted from [165] and [166], respectively.

CLIP technologies, as shown in **Figure 2.16(a)**, can polymerized an entire layer at one time through projection of optical pattern by using digital micromirror device (DMD) or dynamic liquid-crystal masks [114, 167], which provide much higher fabricating speed than TPP technology. Although TPP technology has lower speed in fabrication, the resolution of the technology is higher because the light is tightly confined to a focused voxel with the dimension, as shown in **Figure 2.16(b),** on the order of λ^3 [168], and the two-photon absorption area is even smaller than the focused voxel[169, 170]. It can be seen in **Figure 2.15** that the resolution of two-photon polymerization has the highest resolution among the above mention and achieve a few hundred nanometer feature size.

2.5.2 Optical 3D μ-printing based on DLP technology

Digital light processing (DLP)-based printing technology based on optical micro-electro-mechanical technology that utilizes a digital micromirror device (DMD) to modulate light beam [171]. Based on deformable micromechanical units, the first DMD chip was reported in 1987 by Larry Hornbeck in Texas Instruments Incorporated [172]. A DMD chip typically consists around a million of micro mirrors which can adjust the tilting angle of the micro mirrors (+12° and -12°), as shown in **Figure 2.17 (a)**, so as to realize on/off switch.

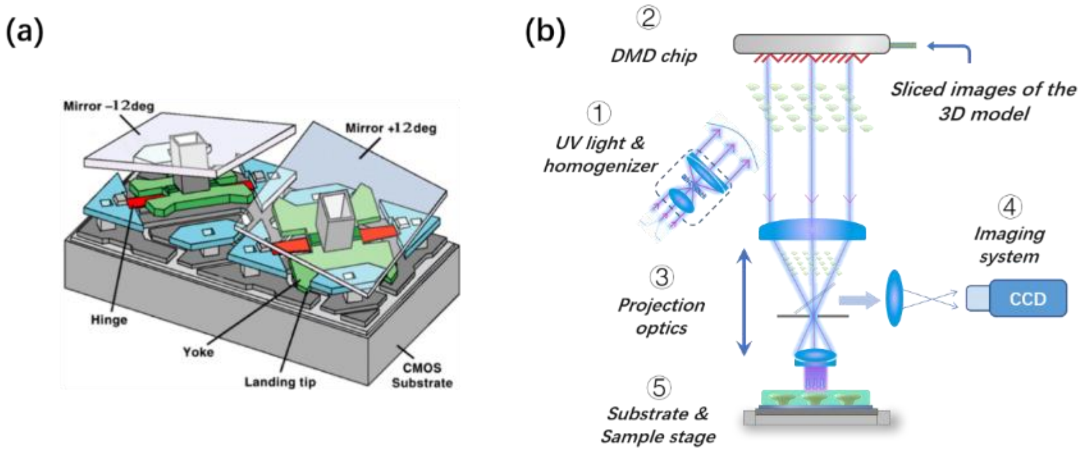

Figure 2.17 (a) Schematic of DMD in state of on/off, adapted from Ref. [173]. (b) Diagram of optical μ-printing platform based on DLP technology.

For optical printing, the DMD chip mainly has three advantages including high resolution, high contrast ratio and high light modulating speed. Due to the development of commercially available DMD chip, the smallest pixel pitch of the DMD chip can achieve 5.4 μm, while it contains micro mirrors with array of 1920 × 1080. With the small pixel pitch and large number of micro mirrors, the DMD chip provides good capability in high-resolution optical μ-printing process.

Compared with other spatial light modulating devices, such as liquid crystal on silicon, the contrast ratio of DMD chip can be as high as 2000:1 which is much faster than liquid crystal spatial light modulators, i.e. 700:1. The high light modulating speed is another important advantage of DMD, which enables the DLP based optical printing technology has the capability of tailoring the profile in z-axis more precisely. The latest DMD chip have light modulating speed of 5 kHz. While the liquid crystal spatial light modulator only have light modulating speed of 200 Hz [174].

As shown in **Figure 2.17 (b)**, the custom-build optical μ-printing technology mainly consists of five parts including UV light source with homogenizer (illumination system), DMD chip, scale-down projection optics, imaging system and sample stage. The homogenized and collimated UV light illuminates the DMD chip in certain angle. The DMD chip generates optical patterns according to the image data of sliced 3D model, and the optical patterns pass through the scale-down projection optics and expose the prepared sample. The in-line imaging system can be used for sample observation and in-situ printing.

The fabrication yield of the custom-build printing technology is mainly limited by the unstable exposure process, difference among batches of photosensitive polymer and environmental contaminant. For exposure process, the UV power of light source, of which the variation is ±5%, plays a key role. To eliminate the effect from unstable UV light source, an optical power detector was used to record the intensity so as to improve the fabrication repeatability. For photosensitive polymer, the relation between the exposure dose and cured depth was studied to achieve the optimized exposure dose for high fabrication yield. Environmental contaminates also affect the fabrication yield, since all our processes were not carried out in clean room. Because of the use of millions of pixels in the printing process, the throughput of the optical printing technology is higher than two photon polymerization technology, of which the exposure time for 3D microstructures array such as microlens array, WGM resonators, microscaffold array are less than 36 s, 46 s, and 30 s, respectively.

The illumination system is one of the most important part of a lithography system, which will affect the quality of projection significantly.

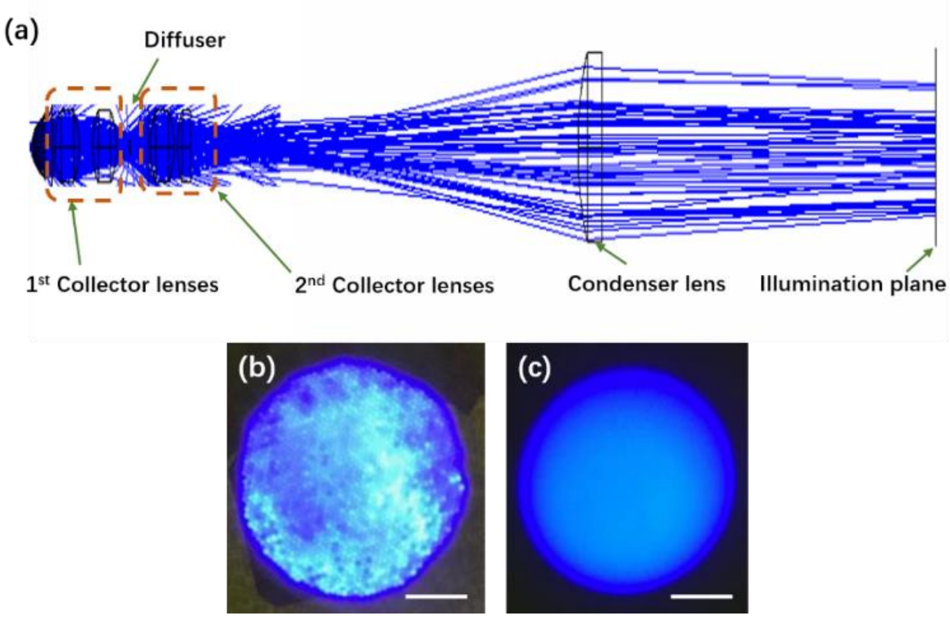

Figure 2.18 (a) Schematic of Kohler illumination system with a diffuser. (b) Uneven illumination by telecentric illumination. (c) Even illumination by Kohler illumination system with a diffuser.

The light from light source usually is not homogenized because of the emission structure of UV LED or some drawbacks of light pipe of UV lamp. To achieve the homogenized illumination, we integrate a diffuser into Kohler illumination system (**Figure 2.18 (a)**). Different from normal Kohler illumination, a diffuser and 1st collector lenses were placed before the Kohler illumination system (2nd collector lenses and condenser lens), which have larger assembling tolerance. The light from light source were collected by two lenses and focused on the diffuser, which can be taken as a new light source for Kohler illumination. Then, the new light source was imaged by 2nd collector lenses, in which the diaphragm of condenser lens locates. Here, due to the focal length of 2nd collector lenses are short, it is difficult to adjust the position and enable the image of light source locate at diaphragm of condenser lens precisely, which may cause that the light source will be imaged at illumination plane. As a result, the diffuser is critically important, which can fuzz the image of light source further.

As shown in **Figure 2.18 (b)**, due to the relatively large depth of field, the telecentric illumination system will image the light source in the illumination plane, which will affect the quality of lithography. The relative even illumination can be achieved, as shown in **Figure 2.18 (c)**, by Kohler illumination system with a diffuser.

2.6 Summary

In summary, different kinds of micro-optics devices and micro-components including microlens, WGM resonator laser, and 3D microstructures are reviewed in this chapter. The optical printing technologies for fabrication of 3D microstructures are also reviewed. Spherical aberration of microlenses can be adjusted by tailoring the conic profiles, which can be utilized in advanced beam shaping. The microlenses with engineered profiles have wide applications especially in optical detection in biochip. WGM resonators with high Q factor and small mode volume intrinsically have advantages in low threshold laser operation. With narrow linewidth, WGM resonator lasers can be utilized as laser sensor by tracking the shift of resonance or measurement of mode splitting. With the advances of optical fabrication technologies and innovation of functional polymer, 2.5D/3D microstructures can be fabricated and functionalized for biological study, such as cell manipulation and cell culture.

Chapter 3

Rapid Optical µ-Printing of Polymer Top-Lensed Microlens Array

3.1 Introduction

As one of the fundamental micro-optics, microlenses attract lots of interest because of its irreplaceable role in various miniaturized optical system[80, 175]. Due to the enhanced capability of light-beam shaping, microlens with complex configuration or profile became increasingly appealing. For example, it is demonstrated that asymmetrically divergent output can be achieved by a microlens with double-axial hyperboloidal profile [176]. For high-density optical storage systems, a microlens with two aspherical surfaces was fabricated for a diffraction-limited focal point [177]. In particular, due to the extraordinary capability of beam shaping, a special kind of microlenses with lens-on-lens microstructures becomes increasingly attractive because its ability of advanced beam shaping, which has promising applications in various optical systems including microfluidic counting systems for fluctuating or unconfined objects and optical storage [28, 178-180]. Due to its unique beam shaping capability, the lens-on-lens microstructure with elongated focal structure is appealing in opto-bio-microsystems, such as flow cytometry for cell counting, which can increase the success rate. And microlens with distinct foci has great potential in multiplexed microfluidic channel for high-throughput flowcytometry.

However, it is difficult for conventional methods, such as microdroplet jetting, hot embossing, and femtosecond laser ablation process to directly fabricate the lens-on-lens microstructures [181-184]. On fabrication of arbitrary form microlens, two-photon polymerization technologies demonstrated capability and flexibility [23, 176, 185, 186]. However, the technology shows low efficiency on fabrication of extensive arrays of microlenses which typically cost a few hours, because of its single-spot scanning nature [183, 187]. To overcome such technical bottleneck, one of the solutions is DMD-based dynamic optical exposure technology. Lu *et al.* demonstrated that the DMD-based dynamic grey masks can enable rapid fabrication of arrays of microlenses [188]. However, the microlenses demonstrated in their work are conventional one with spherical profile. It is still in a loose sense whether the technology can fabricate microlenses with complex profiles, such as lens-on-lens structures.

In this chapter, a DMD based dynamic optical exposure technology was improved so as to print microlenses with lens-on-lens microstrucutures (i.e. TLML) directly. With the in-house optical μ-printing technology, we study the relation between the UV exposure dose and cured depth of photopolymer. Then a bitmap of corrected exposure by the relation was used to generate a dynamic exposure scheme which can tailor the profile of microlens pixel-by-pixel. As a result, the TLML array with focal structures of elongated focus or dual foci can be fabricated facilely and precisely.

3.2 Design of lens-on-lens microlens

The designs of TLMLs with diameters of 290 and 180 μm are shown in **Figure 3.1**. In the first microlens, the upper and bottom parts' curvatures, as shown in **Figure 3.1 (a)**, are 0.0065 and 0.002 μm^{-1}, respectively. In the second microlens, the curvatures of upper and bottom parts are 0.045 and 0.006 μm^{-1}, respectively. Because the dimension of microlenses are far larger than the wavelength in visible range, the propagation of incoherent light passing through the microlens can be simulated using ray tracing method [189, 190]. For a 2D plot of light field after passing through the microlens, 10,000 incidence rays were traced in **Figure 3.1 (b)** in which the intensity depicts the relative number of the rays deposited at each point on a meridional plane. The elongated focal depth of the TLML can be achieved as 570 μm. For the second design, two separate foci can be achieved, as shown in **Figure 3.1 (c)**, by further increasing the difference of the curvature between the bottom and upper lenses. **Figure 3.1 (d)** numerically demonstrates two separate focal points with 215-μm distance was achieved.

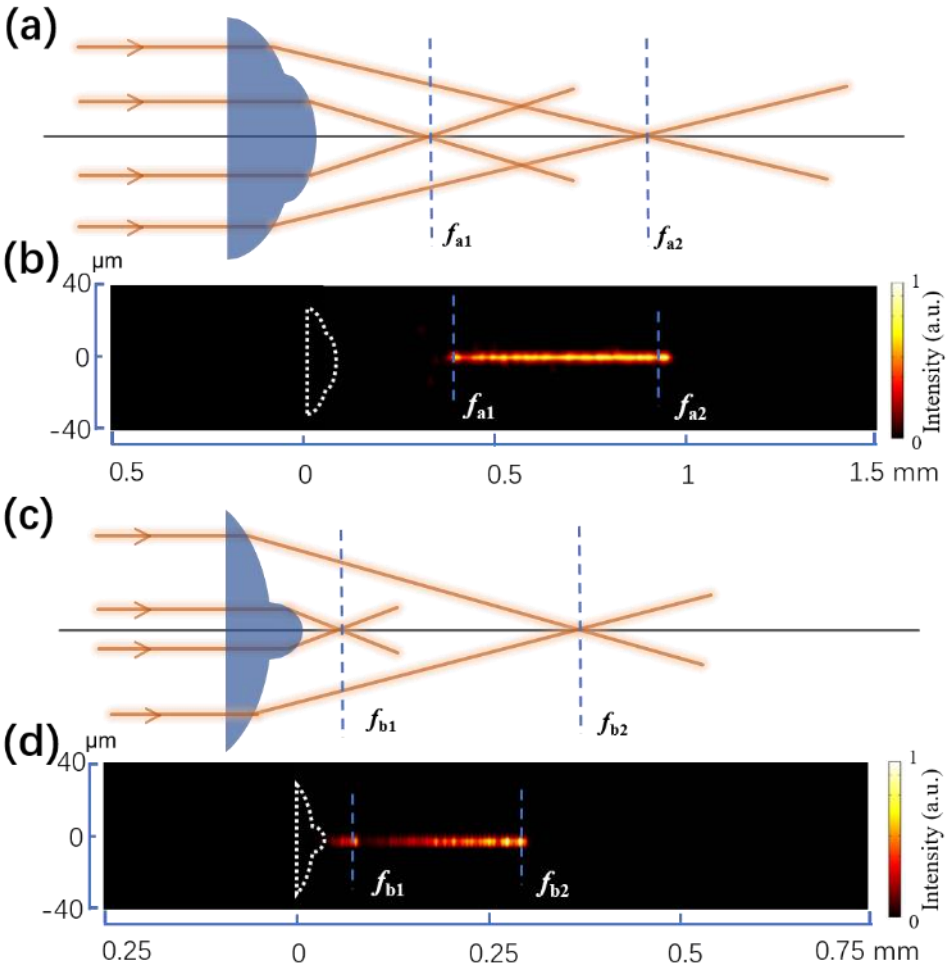

Figure 3.1 Schematic design and simulation of TLMLs. A TLML with elongated depth of focus (a) and its simulated distribution of light field (b). A TLML with dual focuses (c) and its simulated distribution of light field (d).

3.3 Fabrication and testing setup of polymer top-lensed microlens array

Figure 3.2 (a) shows the optical 3D μ-printing platform which consists a high-resolution XY stage (M-687, Physik Instrumente GmbH & Co.), a digital micromirror device (DMD, DLi4120 0.7” XGA, Texas Instruments, USA), a set of projection optics (Thorlabs, Inc., USA), and a high-power UV light source (OmniCure 2000 System, Lumen Dynamic Group Inc.).

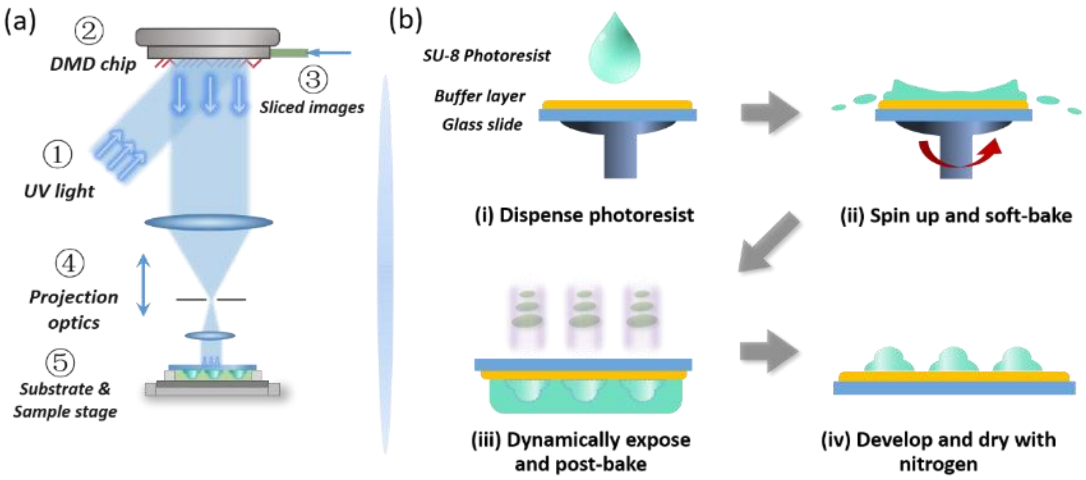

Figure 3.2 (a) Schematic diagram of the optical µ-printing platform: collimated UV light illuminates the DMD chip which loads the data of sliced modal and reflects light with designed patterns. The patterns are projected through sets of lenses onto SU-8 photoresist to fabricate microlens arrays. (b) Fabrication process of microlens array; (i) SU-8 photoresist is dropped on the glass slice with buffer layer; (ii) the photoresist is spin-coated and soft baked to remove solvent; (iii) the data of sliced images of 3D model is inputted into DMD chip, and the photoresist is dynamically exposed and post baked. (iv) the exposed resin is developed and dried.

The stage can locate the position of exposure, which enable to fabricate large-area microstructures by seamless pattern-stitching process. The 3D model of designed microlens is sliced into 100-layers bitmap by an in-house add-on of a commercial image data analysis software (Tecplot Inc., USA). Before illuminating the DMD chip, the light beam of the UV lamp is homogenized and collimated. According to the sliced bitmap, the DMD chip, as a spatial light modulator, can switch into corresponding patterns dynamically and generate the optical patterns by reflecting UV light into the projection optics. Thereafter, the optical patterns are projected on the SU-8 resin. Based on layer-by-layer polymerization, the designed 3D microstructures were manufactured. The key of fabricating the MLAs with smooth profile is the DMD chip which can regenerate optical patterns for each polymerized layer by flipping the micro-mirrors in 30 μs.

Figure 3.2 (b) shows the fabrication process of MLAs including making buffer layer, spin-coating, soft bake, dynamic exposure using OMsL, post bake, and development. A thin film (~ 1 μm) of SU-8, as a buffer layer, was spin-coated on a clean glass slice for improvement of adhesion between glass and microstructures. This layer was exposed by a UV lamp (2.61 mW/cm2) for 20 min, and then was baked at 95 °C for 3 min. Then, the prepared SU-8 photoresist was spin-coated on the glass slice with buffer layer. The glass slice with photoresist was baked at 65 °C for 5 min, and at 95 °C for 15 min in soft bake, which can minimize the solvent concentration. When the sample cooled down to room temperature, the UV light with a light intensity of 41.15 mW/cm^2 was applied for 36 seconds in the whole maskless exposure process. After exposure, the sample was post baked at 65 °C for 5 min, followed by a subsequent bake at 95 °C for 10 min. After that, propyleneglycol monomethylether acetate (J&K Scientific, China) was applied for 10 min in development.

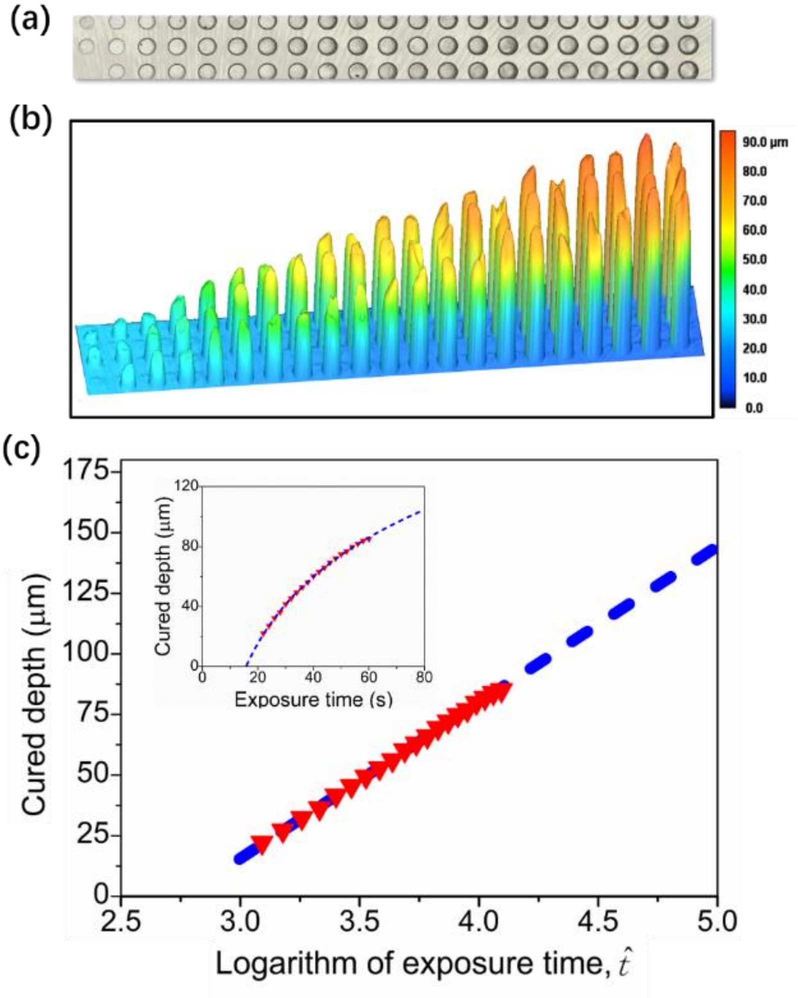

Figure 3.3 Optical microscopic image (a) and confocal laser scanning 3D image (b) of the fabricated SU-8 micro-pillar array for calibration of exposure time. (c) Dependence of cured depth on the natural logarithm of exposure time. The inset is the curve of cured depth verses exposure time.

For the fabrication of MLAs with engineered profile, the required exposure dose of the design should be optimized according to the relation between cured depth and exposure dose. For investigation of the relation, a series micro pillars with growing height, as shown in **Figure 3.3**, were fabricated by applying increasingly exposure time. The optical microscopic image and laser scanning confocal 3D image of the micro pillars was shown in **Figure 3.3 (a)** and **Figure 3.3 (b)**, respectively. The height of micropillars was from 17.10 μm to 84.53 μm when the exposure time increased from 22 to 60 seconds. **Figure 3.3 (c)** left inset shows that the height of the micro pillars (i.e., the cured depth of resin) increased with the accumulative exposure dose, and the UV light intensity was fixed in 41.15 mW/cm^2. A threshold of exposure time can be observed, which is the minimum exposure dose requirement for the initially cured photoresist. The threshold is related to the ratio of concentration of photo initiator to photo inhibitor which can neutralize photoacid during the exposure process. The relation between the cured depth and exposure dose is not linear, because the UV absorber and SU-8 resin can hinder the penetration of UV light in photoresist. The relatively flat curve in the end is caused by weaker light in deeper photoresist.

Figure 3.3 (c) shows cured depth versus logarithm of exposure time which is a linear relationship. According to Beer Lambert law, such a nonlinear relation caused by the absorption of UV light in SU-8 resin and TINUVIN 234 can be written into a linear equation as

$$\mathrm{d} = \gamma \ln(t) - \gamma \ln(E_{th}) \tag{3.1}$$

where d is cured depth, t represents exposure time (larger than E_{th}), γ is defined as the linear slope of the curve, and E_{th} is the threshold time of exposure. In certain UV light intensity, the slope is related to the ratio of photo initiator to UV light absorber in photo resist. The larger ratio causes larger slope γ. In a fixed UV light intensity, the ratio of photo initiator to photo inhibitor influences the threshold time. The relatively higher concentration of photo inhibitor leads longer threshold time, as the initially generated photoacid will be neutralized by photo inhibitor. Here, the fitting result shows γ is 56.25, while threshold time E_{th} is 15.75 seconds.

The focusing performance of the microlenses was tested by using an own-established setup, as shown in **Figure 3.4**. To minimize the refractive effect of the microlens, a LED light source, as an incoherent source, instead of laser source is used in the testing setup.

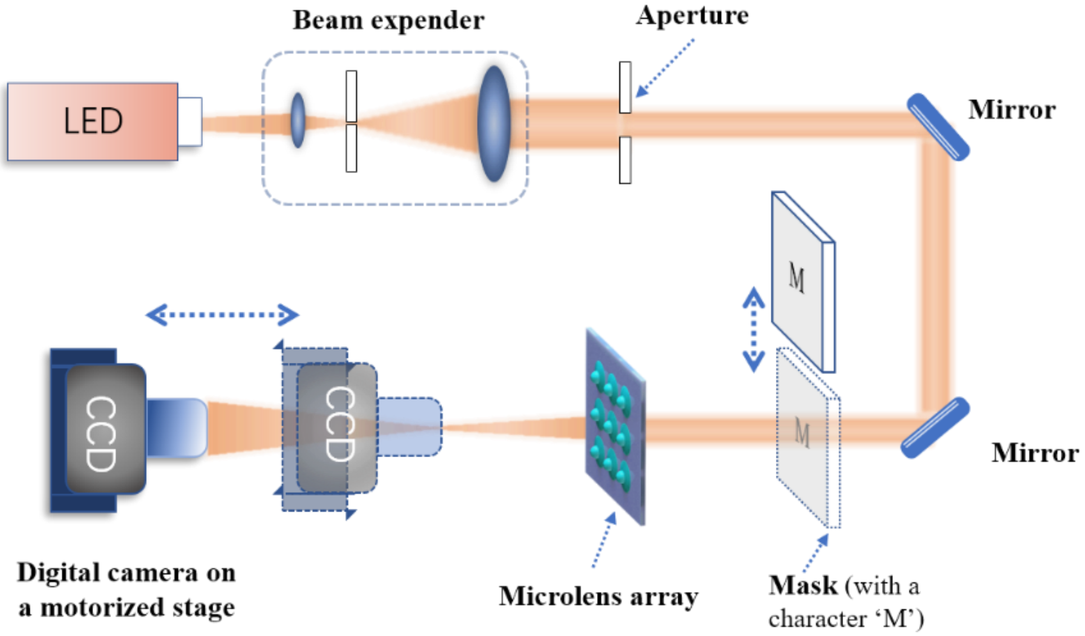

Figure 3.4 Testing setup for focusing performance and imaging ability. For testing of focusing performance, the LED light was collimated by a beam expender and illuminated the microlens arrays from the side of substrate directly. For testing of imaging ability, the mask with a character "M" was put between the microlens and beam expender.

The LED light was collimated by a set of lenses, and the collimated light is reflected by two mirrors and then illuminates the glass substrate. The collimated light passes through the sample from bottom to top so as to avoid that the glass substrate refracts the light once again which will affect the optical property of microlens on the testing. To measure the light field intensity distribution along the optical axis, a motorized stage is mounted a digital camera, which can move along the optical axis of microlens and take images of light field distribution. A LabVIEW program was used to automate the capturing of images every 5 µm from the microlens to the position that is 1750 µm away the microlens.

For testing of imaging ability, a 4mm-by-3mm mask with a character “M” was used and put between the glass substrate of microlens array and the reflect mirror. During the testing procedure, the distance between mask and ML-0, TLML-1 and TLML-2 are about 9, 18, and 7 mm, respectively.

3.4 Results

3.4.1 Fabricated microlens array

Within 36-seconds exposure time, three groups of microlens arrays without and with top-lensed microstructures were experimentally fabricated, called ML-0, TLML-1 and TLML-2, respectively. Scanning-electron microscope images of arrays of microlens, as shown in **Figure 3.5**

(a)-(c), are taken by VEGA3, TESCAN company at 20 kV with magnifications of 276, 134, and 260, respectively. **Figure 3.5 (d)-(f)** are the zoom-in SEM images of the microlens in **Figure 3.5 (a)-(c)**, respectively. All microlenses are with circular apertures and arranged in orthogonal array. **Figure 3.5 (g)-(i)** are the designed (dash curves) and measured (solid curves) cross-sectional profiles of corresponding microlenses. The standard deviation of the profiles of single-focus microlens, TLML-1 and TLML-2 are 0.88, 0.46 and 0.71 μm, respectively.

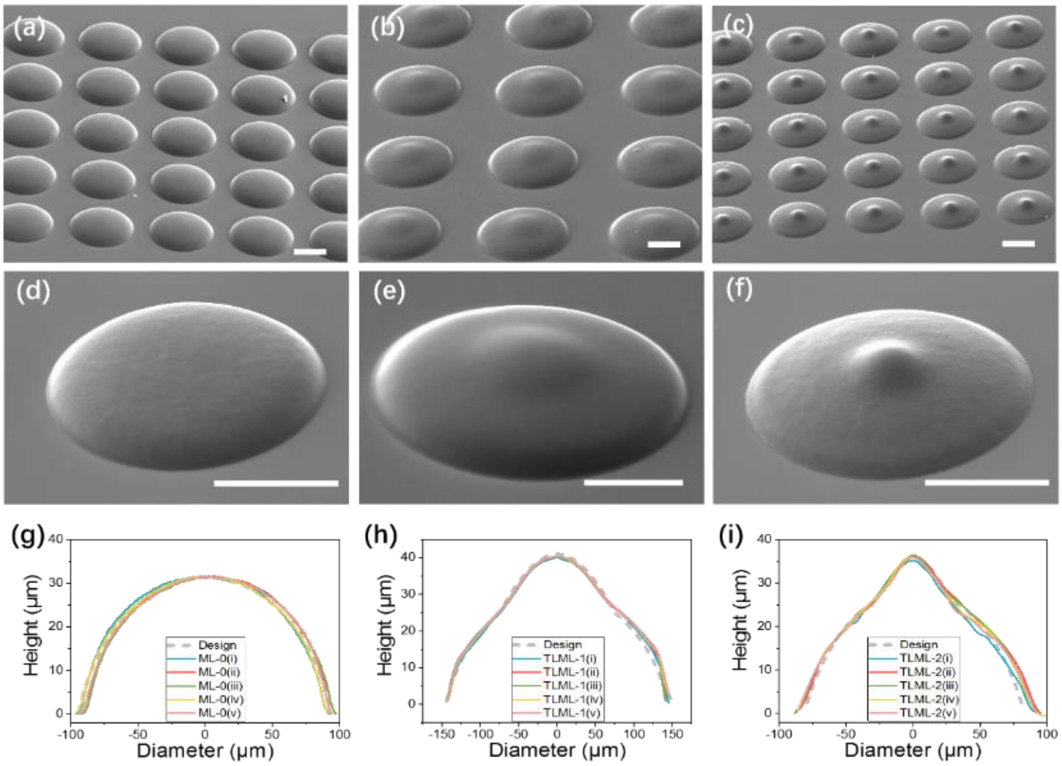

Figure 3.5 (a) to (c) are SEM images of the arrays of single-focus microlens, TLML-1 and TLML-2, respectively. (d) to (f) are zoom-in images of (a) to (c), respectively. (g) to (i) are designed and measured profiles of the microlenses (d) to (f), respectively. Scale bars are 100 μm.

The profiles were measured by a laser-scanning confocal microscopy (Keyence VK-X200K), which shows the height are 32.9, 40.1, and 35.1 µm, respectively, and diameters are 184.1, 296.83 and 178.02 µm, respectively. For TLML-1 and TLML-2, the diameters of the top lenses are 120.1 and 50.8 µm, respectively. The profile of individual lenses can be approximated by conic surface using the equation [191],

$$z(r) = -\frac{cr^2}{1+\sqrt{1-(1+k)c^2r^2}}. \tag{3.2}$$

The fitted results of the parameters of the measured profiles of the fabricated microlenses, which were measured by using laser-scanning confocal microscopy, were given in **Table 3.1**. It can be seen that the lower-lenses (L.) of TLML-1 and TLML-2 are oblate ellipsoidal, whose conic constants are 11.31 and 2.33, respectively. The upper-lenses (U.) of both TLML-1 and TLML-2 are hyperbolic, whose conic constants are -3.5455 and -4.8393, respectively.

TABLE 3.1 Fitted results of the curvature *c* and the conic constant *k* of the profiles of three kinds of fabricated microlenses.

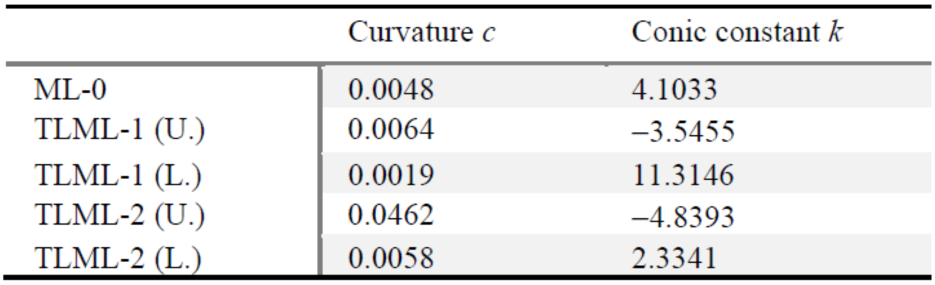

	Curvature c	Conic constant k
ML-0	0.0048	4.1033
TLML-1 (U.)	0.0064	−3.5455
TLML-1 (L.)	0.0019	11.3146
TLML-2 (U.)	0.0462	−4.8393
TLML-2 (L.)	0.0058	2.3341

3.4.2 Simulation of fabricated microlens array

With the measured profiles, numerical simulations have been carried out by using ray-tracing method to compare with measured results. As the light beam in testing had a small divergent angle, in simulation, numerous rays were released from a spherical surface with the curvature of $3\times 10^{-4}\mu m^{-1}$ which was put in front of microlens. The refractive index of SU-8 is assumed to be 1.59.

Light field distributions of fabricated microlens are shown in **Figure 3.6**. It is shown in **Figure 3.6a (i)** that the light beam is converged by the single-focus microlens at round 394.4 μm and forms the focal spot from the ring shape. As shown in **Figure 3.6a (ii)**, focal structure distributed along the longitudinal axis instead of as a single focal point which results from the spherical aberration. The spherical aberration can be deduced from the conic constant of single-focus microlens, as shown in **Table 3.1**, which is around 4.1.

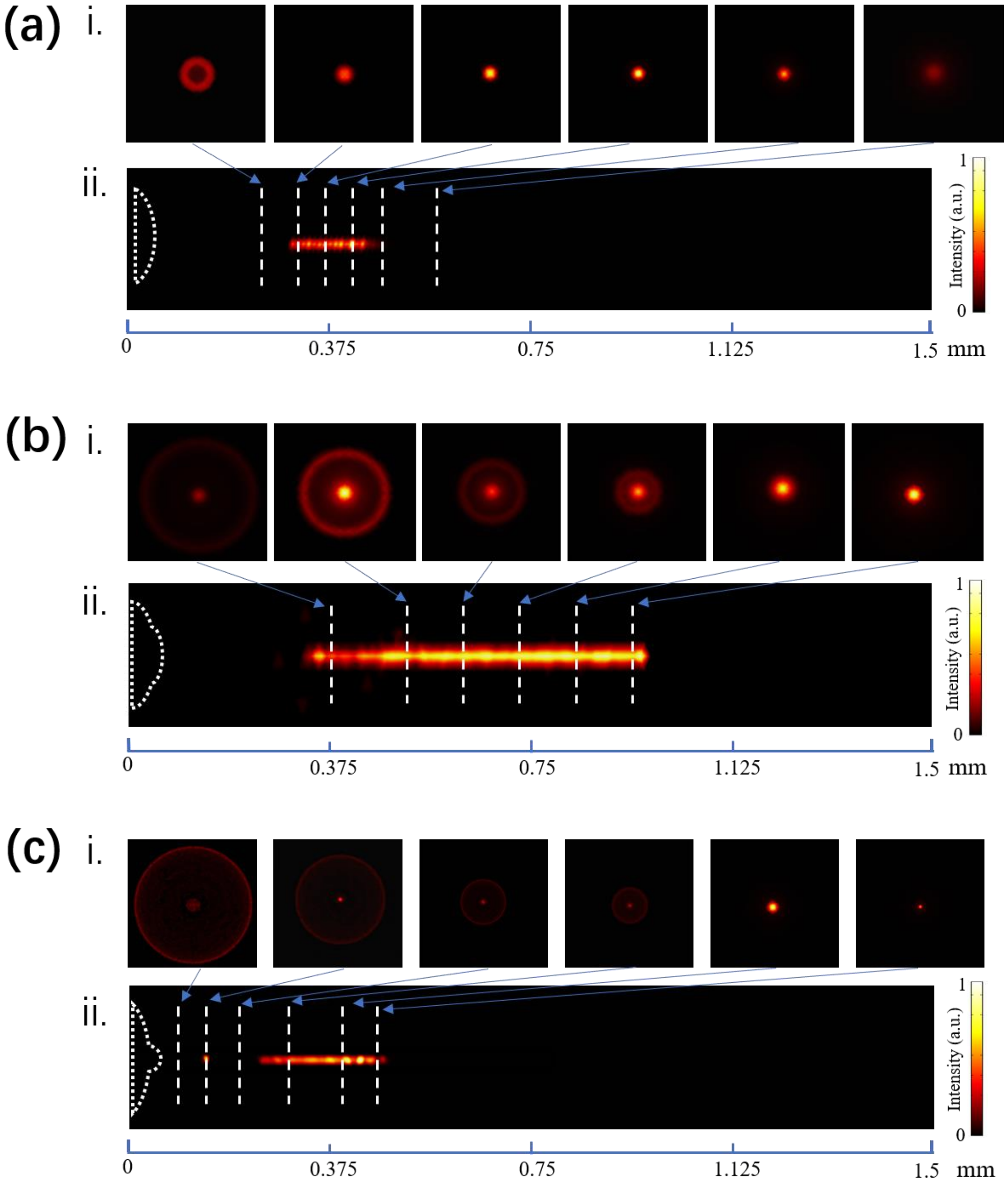

Figure 3.6 Simulation of light field intensity distribution of (a) single-focus microlens, (b) TLML-1, and (c) TLML-2, in which (i) is cross-sectional distribution at corresponding positions and (ii) longitudinal distribution along the optical axis.

The light field distribution of top-lensed microlens 1 is shown in **Figure 3.6 (b)**. Different from light field distribution of single-focus microlens, when the first focus appears, as shown in **Figure 3.6b (i)**, there is a ring around it. The first focus is formed by the top lens with smaller curvature of radius, while the ring from the bottom lens with larger curvature of radius. When the first focus diverges, the light refracted by the bottom lens converge and maintain the light field intensity along the optical axis. In **Figure 3.6b (ii)**, the first small focal point locates at around 366.1 µm. Large spherical aberration is induced in the bottom lens, which is shown in **Table 3.1**. As a result, one can see that the second focal area is long. When this long focal area connects to the first focal point, it is realized the elongated focal structure.

In **Figure 3.6 (c)**, the light field distribution of top-lensed microlens 2 is shown. The focal structure of first focal structure of top-lensed microlens 2, as shown in **Figure 3.6c (i)** also contains one focus and a ring around it. The difference between the first focus in **Figure 3.6b (i)** and **Figure 3.6c (i)** is that the first focus of top-lensed microlens 2 is sharper and clear, which indicated that the upper lens of top-lensed microlens 2 has smaller spherical aberration. In **Figure 3.6c (ii)**, one can see the first focal point locates at around 88.7 µm and separates from the second focal area, which forms the two distinct focal structure.

3.4.3 Light intensity distribution and imaging ability

The distributions of optical intensity along the optical axis, as shown in **Figure 3.7 (a)-(c)**, were drawn by extracting the light intensity of the images at the determined focus' location. **Figure 3.7 (d)-(f)** show the images of light patterns at corresponding position in **Figure 3.7 (a)-(c)**, respectively. To compare with the measured focal parameters, the simulated optical intensity distribution on optical axis were shown in **Figure 3.7 (a)-(c)** as dash lines.

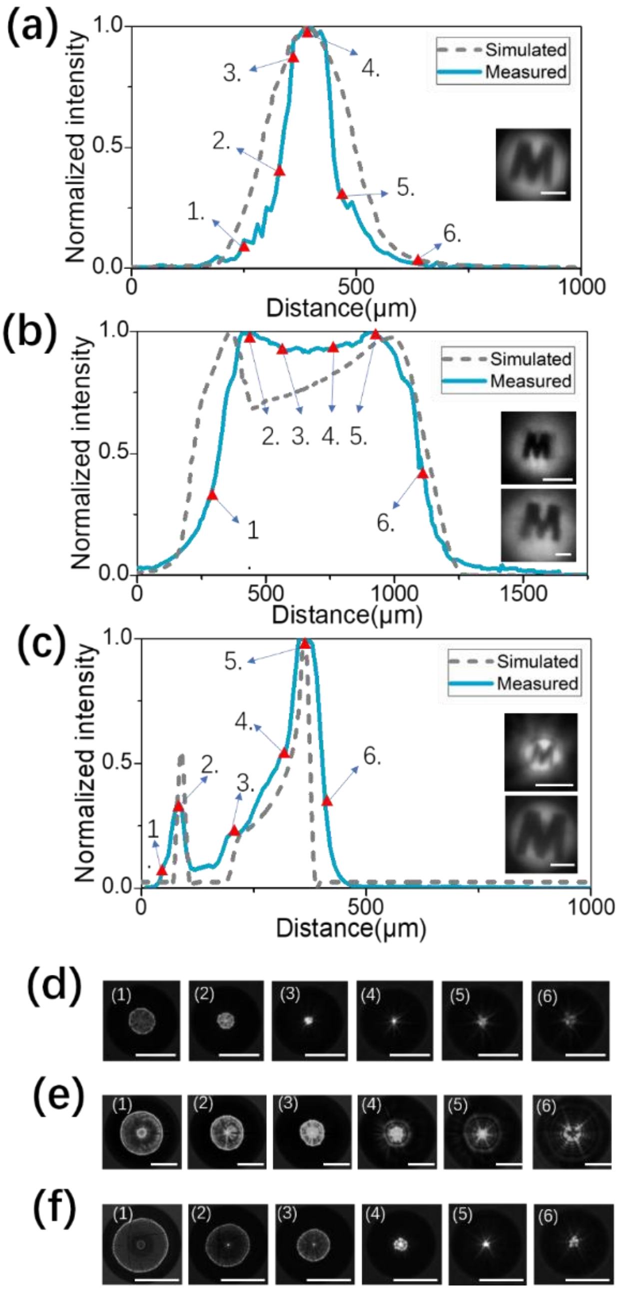

Figure 3.7 (a)-(c) are measured and simulated light intensity distributions along the

optical axes of single-focus microlens, TLML-1, TLML-2, respectively. The insets are the measured images of the character 'M' projected by the microlenses, in which the scale bars are 25 µm. (d)-(f) are measured transverse optical images at different positions in (a)-(c), respectively, and the scale bars are 100 µm.

The focal position of the fabricated ML-0, as shown in **Figure 3.7 (a)**, was measured to be at 400 µm, while the simulated focus located at 394.4 µm. It is shown in the inset of **Figure 3.7 (a)** that the image of characteristic 'M' project by fabricated ML-0.

As shown in **Figure 3.7 (b)**, the fabricated TLML-1 has two focal points, the first one locates at 410 µm while the second on locates at 910 µm. The elongated focal depth of TLML-1 is demonstrated that the depth of focus at half maximum is 767.11 µm. The simulation results show that the two focal points locate at 366.1 µm and 992.9 µm, respectively. According to the simulation results, the close location of the two focal points results from the elongated depth, while the flat light nitensity distribution between first and second focus attributes to the smooth transition between the upper lens and bottom lens. The imaging pictures of characteristic 'M' by upper and bottom lenses are shown in the upper and lower insets in **Figure 3.7 (b)**.

The spider-web like segmented structures of the images may attribute to the structure of LED's emitting area and the TLMLs' astigmatism aberration. The cross-sectional light intensity distributions at the corresponding places in **Figure 3.7 (b)** are shown in **Figure 3.7 (e)**. The light passing through the upper and bottom lenses result in a focal point and the outer ring in **Figure 3.7e (1-3)**. Then the first focus from the upper lens diverge gradually, while the light from bottom lens converge from the ring to the focus and maintain the light intensity. The structure of LED's emitting area and astigmatism of the fabricated lens should be attributed to the spider-spoke like light pattern structure.

By increasing the difference between the curvatures of upper lens and bottom lenses, the TLML-2 with two distinct focal points can be achieved. For TLML-2, the light intensity distribution along the optical axis was shown in **Figure 3.7 (c)**. The first and second focal points were measured to locate at 80 μm and 360 μm, respectively. The simulation result shows that the first and second foci were at 88.7 μm and 363.1 μm, respectively, which confirms well with the measured results. Due to spherical aberration caused by the oblate ellipsoidal shape of the bottom lens, the light distribution is not symmetric. There is a bit mismatch between the simulated and measured plots because of the complex input light condition and uneven refractive index of the polymer microlenses.

For the imaging ability, due to the smaller spherical aberration of the lower part of TLML-2, the image from bottom lens of TLML-2 is clear than the bottom lens of TLML-1. The spherical aberration can be deduced from the sharpness of the focal point, in which **Figure 3.7f (5)** has a sharper focal point than in **Figure 3.7e (5)**. Similarly, the image from upper lens of TLML-2 is clear than the upper lens of TLML-1 due to the smaller spherical aberration, which can be deduced from **Figure 3.7e (2)** and **Figure 3.7f (2)**.

TLML-1 demonstrated the capability of extending the focal length by adopting aspherical lens-on-lens microstructure. The elongated focal structure is suitable for detection of fluctuated targets in microfluidics, because it can enhance the success rate of detection by enlarging the detection area. Also, the microlens with elongated focal structural is appealing in endoscopic bioimaging microsystem, in which the microlens can elongate the imaging depth. TLML-2 can generate two distinct foci, which can be used in rapid and high-throughput optical analysis of cell on compact multiplexed microfluidic channels.

Compared with the inorganic microlenses such as glass devices in opto-bio-microsystems,[81] limitation of the polymer microlenses include surface roughness and chemical resistance. The relatively rougher surface is mainly caused by thermal distortion during post-baked process and development of uncured polymer, which can be further improved by using programmed hot plate and the developer with surfactant. The relatively limited chemical resistance of polymer induce that the devices are not compatible with certain cleaning processes including acid for removing protein, which may hinder the reusability of devices in practical application

3.5 Summary

To sum up, a fast and facile fabricating method was developed for microlens arrays with complex profile, such top-lensed microlens. Different focal structures of microlens with complex profile have been demonstrated experimentally. For the elongated focal depth, a lens-on-lens microstructure with hyperbolic upper-lens and bottom-lens with oblate ellipsoidal profile has been printed. For focal structure with two distinct focuses, the difference between the curvature of upper-lens and bottom-lens in the top-lensed microlens was further increased. Such TLMLs have great potentials in laser beam shaping for e.g. real-time detection of fluctuating target in microfluidic channel.

Chapter 4

Optical 3D μ-Printing of WGM Microlaser Sensors for On-Chip Ultrasensitive VEGF Detection

4.1 Introduction

Optical microcavities can spatially confine light into microscale dimensions to form resonant recirculation.[192] Various optical microcavities, such as Fabry-Perot, Whispering-Gallery-Mode (WGM), and photonic crystal microcavities, have been widely demonstrated to achieve high-performance photonic devices and systems.[6, 193, 194] In particular, WGM microcavity attracts increasing research interest due to its high-quality factor and tight mode confinement, which thus can achieve high light intensity inside microcavity even when the input power is not very high.[100] In the tightly confined cavity mode under lasing operation, the strong interaction between light field and active material can enhance pumping efficiency and therefore enable low-threshold laser oscillation.[30, 195-197] Compared with passive optical microcavities which rely on evanescent-wave coupling to interrogate the optical WGM microcavities[198], WGM microcavity lasers can be efficiently excited and collected by free-space coupling.[113, 199, 200] Herein, the microcavity lasers can alleviate the coupling difficulties in practical application [201, 202] and thus can be integrated into on-chip bio-microsystems as optical sensing components.[18, 203, 204] With the characteristics of narrow linewidths and high contract ratio between ON and OFF resonance, WGM microlasers have been widely applied as highly sensitive biosensors for detection of protein, lipids, DNA, and virus.[31, 110, 125, 205-207] Laser intensity-modulation based biosensors are of great interest, because they can not only improve discrimination ratio[208] but also save cost in e.g. use of photo-detector, e.g. commercial camera, which thus provide an high-performance and affordable sensing platform for biomarker detection.[209]

Quantitative detection of disease biomarkers is of great importance in diagnosis of diseases in early stage.[210] Vascular Endothelial Growth Factor (VEGF), a hypoxia-inducible protein, plays an important role in vascular development, and the abnormal expression of VEGF associates with many diseases such as early diabetes, cancer and neurological disorders.[211-213] Enzyme-Linked Immunosorbent Assay (ELISA) has become the gold standard for quantitative detection of VEGF because of its advantages of high sensitivity and high specificity.[214] To further enhance the sensitivity of ELISA-based approach, various technologies have been demonstrated, such as plasmonic, fluorescence, and laser-based methods.[215-217] In particular, optofluidic chip technology, combining photonic devices and microfluidics, attracts much research interests for miniaturized on-chip integration.[216]

In this chapter, we present an optically 3D μ-printed WGM low-threshold microlaser array and its integration within a microfluidic chip for highly sensitive detection of VEGF. With an improved in-house DMD-based optical μ-printing platform,[218, 219] we directly print arrays of suspended microdisks with smaller size and finer structures so as to achieve WGM resonators with Q factor higher than our previous work[105]. The microdisks were then deposited with a thin layer of gain media for low-threshold laser oscillation. A pair of multimode optical fibers were used to pump the WGM resonator and collect light from the plane of the laser to achieve on-chip integration. A microfluidic chip is fabricated to integrate arrays of microlasers to achieve a platform for on-chip ELISA-based optical detection of VEGF. Compared to conventional ELISA, the microlaser-enhanced device can boost the LOD to 17.8 fg/mL, which is 500 times lower than conventional ELISA kit.

4.2 Fabrication of polymer WGM microcavity lasers

To fabricate the high Q microcavity lasers, we use an improved optical 3D μ-printing technology. **Figure 4.1 (a)** shows the schematic diagram of optical 3D μ-printing technology. The UV light from a light pipe of mercury arc lamp is homogenized and collimated and then illuminates the DMD chip which can generate patterns according to the sliced images of the 3D model of WGM microcavity. The optical patterns pass through a set of scale-down projection optics and project upon the prepared sample. The motorized sample stage can not only be utilized to locate sample position but also boost seamless stitching to print large-scale arrays of WGM microcavities.

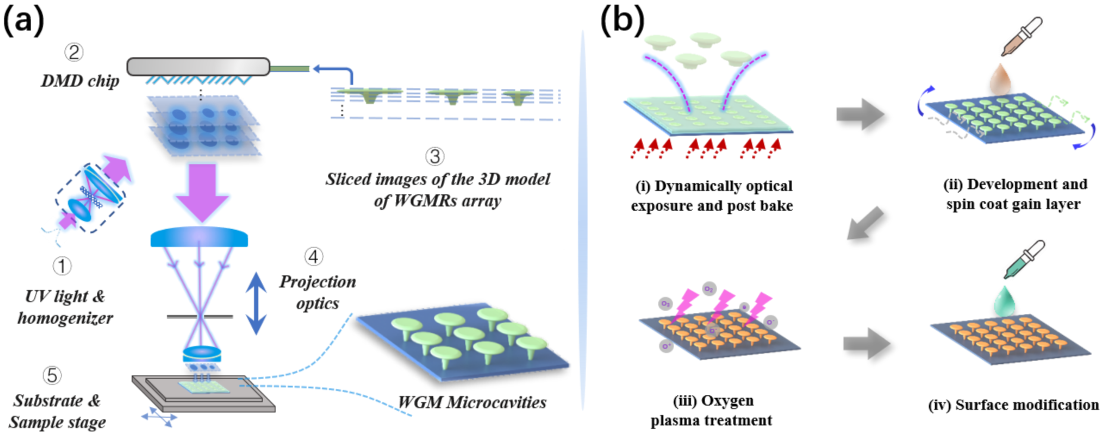

Figure 4.1 (a) Schematic of the optical μ-printing technology. (b) Processing flow of fabrication of WGM microcavity laser sensors.

EPON resin SU-8 was used as the photopolymer for the fabrication of WGM microcavities. Octoxyphenylphenyliodonium hexafluoroantimonate (OPPI) was added as photoacid generator, and TINUVIN 234 was used as UV absorber, while Tributylamine (Tba) was used as inhibitor. With the cyclopentanone as solvent, we mix the compositions in the weight ratio of TINUVIN 234/ Tba/ OPPI/ SU-8 = 0.08:0.014:2.5:100. Before the exposure process, the SU-8 photopolymer was spin-coated upon a thin buffer layer (~1 μm) which can enhance the adhesion between the substrate and photopolymer. The photopolymer was then soft-baked at 65 °C for 5 min and 95 °C for 20 min so as to remove the solvent. The sample was dynamically exposed, as shown in **Figure 4.1 (b)**, by using optical 3D μ-printing technology.

To print high-quality WGM microcavities of suspended microdisks, the relation between the exposure dose and cured depth of photopolymer has been investigated to determine the exposure time of each sliced images of WGM microcavity. A series of micro-scale pillars were printed with increasing exposure time to obtain the relation. By applying the exposure time from 14 to 80 s with UV intensity of 1.81 mW/cm^2, the heights of pillars were measured to be from 1.8 to 12.7 μm.

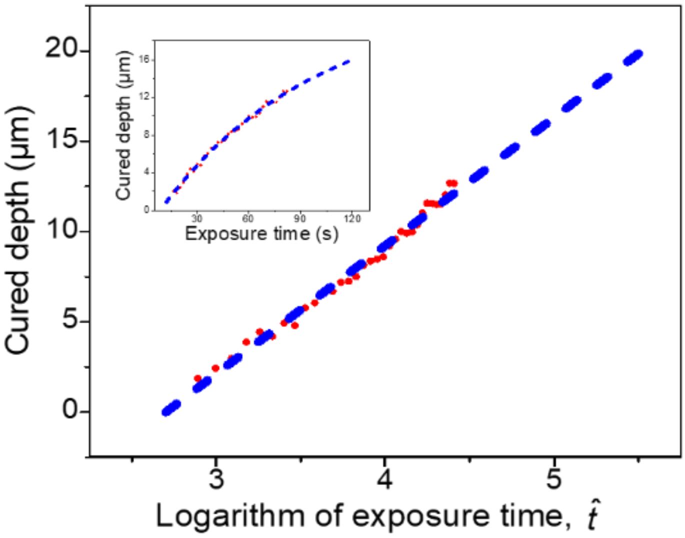

Figure 4.2 Dependence of the cured depth on natural logarithm of exposure time. The inset is the cured depth versus exposure time.

As shown in the inset of **Figure 4.2** the cured depth of photopolymer increases nonlinearly with increase of exposure time, which can be explained by Beer Lambert law. According to **Eq. 3.1**, such a nonlinear relation can be rewritten into a linear equation by taking logarithm of exposure time. The fitting result shows that, in the relation, the threshold time t_{th} is 14.29 s, while the slope of the equation γ is 6.89. Such a small slope enables us to print finer structure is z-axis.

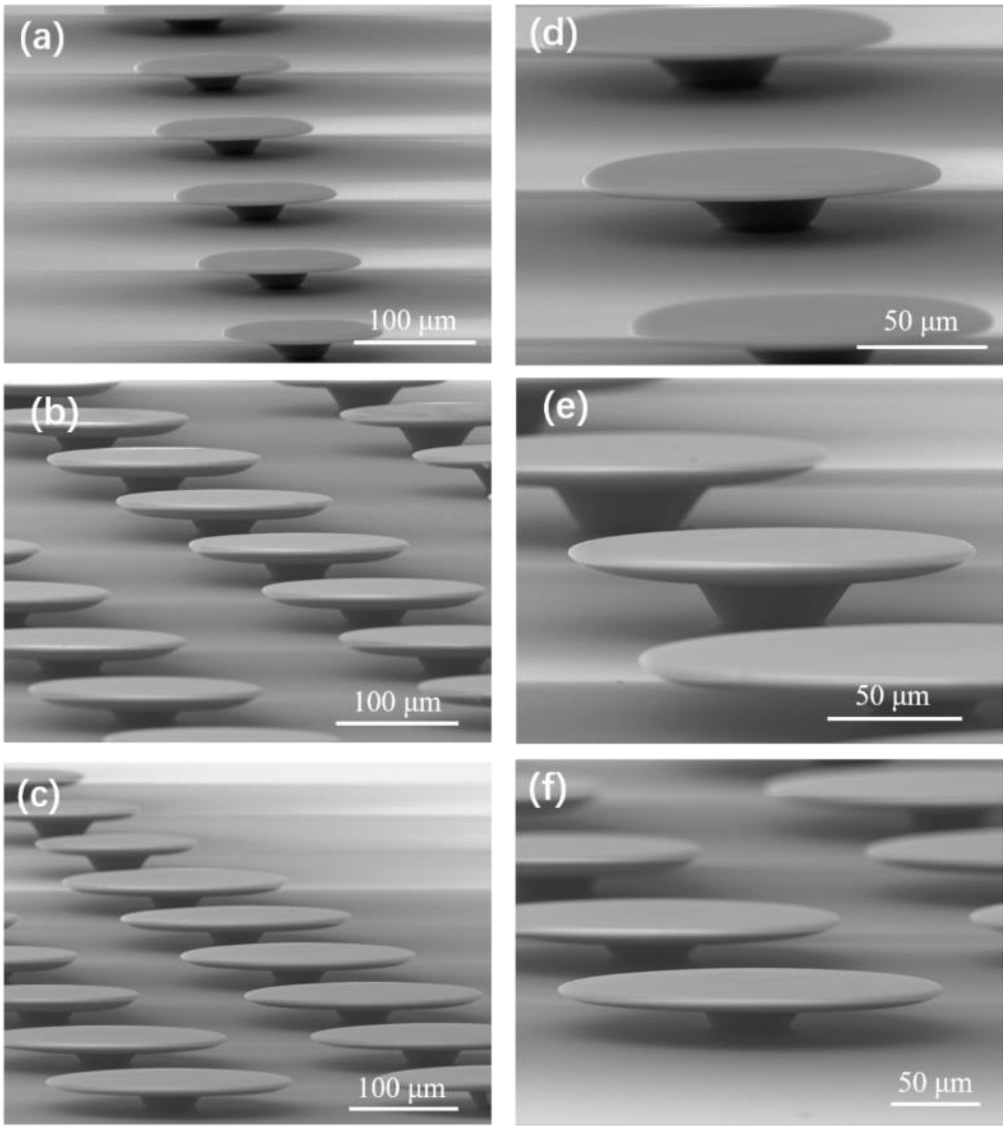

Figure 4.3 (a)-(c) are SEM images of SU-8 WGM microcavities with diameters of 116, 145, and 195 μm, respectively. (d)-(f) are zoom-in images of (a)-(c), respectively.

In the experiments, three groups of WGM microcavities with suspended microdisks were directly printed, called WGMR-1, WGMR-2 and WGMR-3, respectively. The exposure time of the WGM microcavities is less than 46 s. As shown in **Figure 4.3 (a)-(c)**, the diameter of WGMR-1 to WGMR-3 are 116, 145, and 195 μm, respectively. The heights of the three groups of WGM microcavities were measured to be around 30 μm by using a laser-scanning confocal microscope.

After exposure process, the samples were post-baked at 65 °C for 5 min and then followed by 95 °C for 8 min to cure the polymer. After a post-bake process, the sample was developed by using propylene glycol monomethyl ether acetate (PGMEA). To prepare WGM microlasers, 20% SU-8 resin was doped by Rh6G in concentration of 3 μmol/g solid SU-8 and then spin-coated upon the fabricated WGM microcavities. Soft-bake process was then used to remove the solvent.

4.3 Simulation of the WGM microcavities

Finite element method-based simulation software (COMSOL Multiphysics 5.1) has been used to investigate the field distribution of WGM microcatlvies with suspended microdisks.

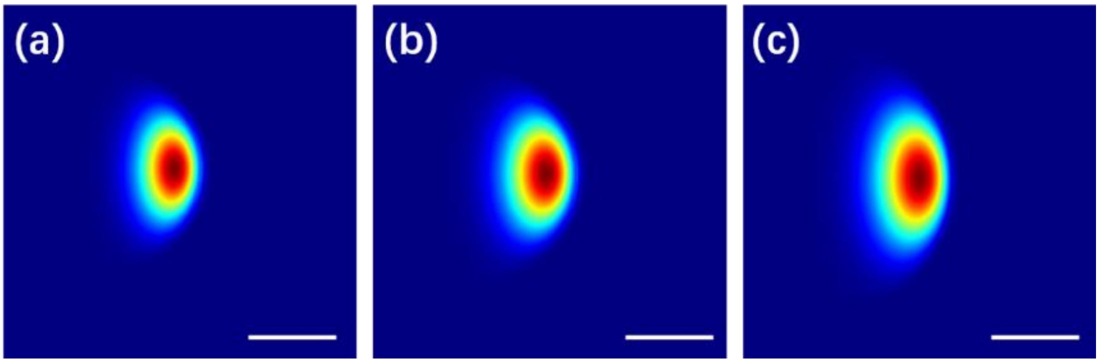

Figure 4.4 The cross-sectional field distribution of (a) WGMR-1, (b) WGMR-2, and (c) WGMR-3, whose characteristic indexes are (q, m, ℓ) = (1, 940, 940), (1, 1186, 1186), (1, 1585, 1585), respectively. The scale bars are 2 μm.

As mentioned in section 2.3.1, whispering gallery mode can be mainly described by three factors, i.e. radial mode number q, polar mode number m, and azimuthal mode number ℓ. Radial mode number q represents the number of maxima in the radial direction. Polar mode number m denotes the number of wavelengths along the boundary of microcavity and the direction of wave circulation. Azimuthal mode number ℓ stands for the number of electrical maxima in the equatorial plane. As shown in **Figure 4.4 (a)-(c)**, the fundamental TM mode are found at 604.13, 604.31, and 604.14 nm, respectively, when the azimuthal mode numbers are 940, 1186, and 1585, respectively.

4.4 Characterization of WGM microcavities

To measure the transmission spectra of WGM microcavities, a biconically tapered fiber with waist diameter of around 1.3 μm was prepared to couple light into and out from the microcavity.

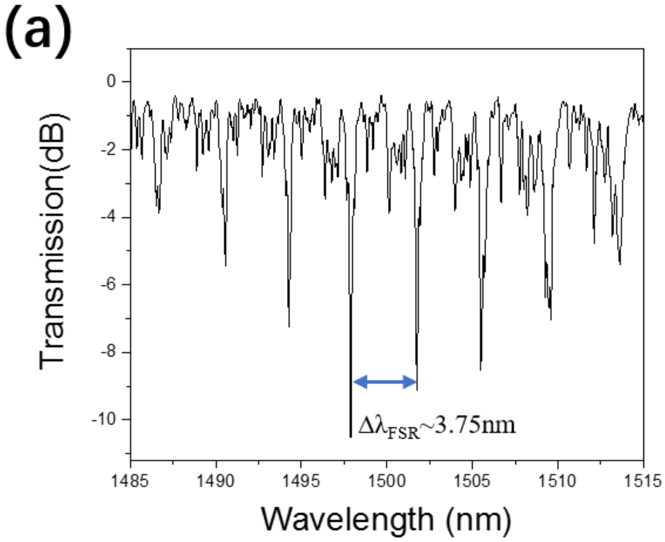

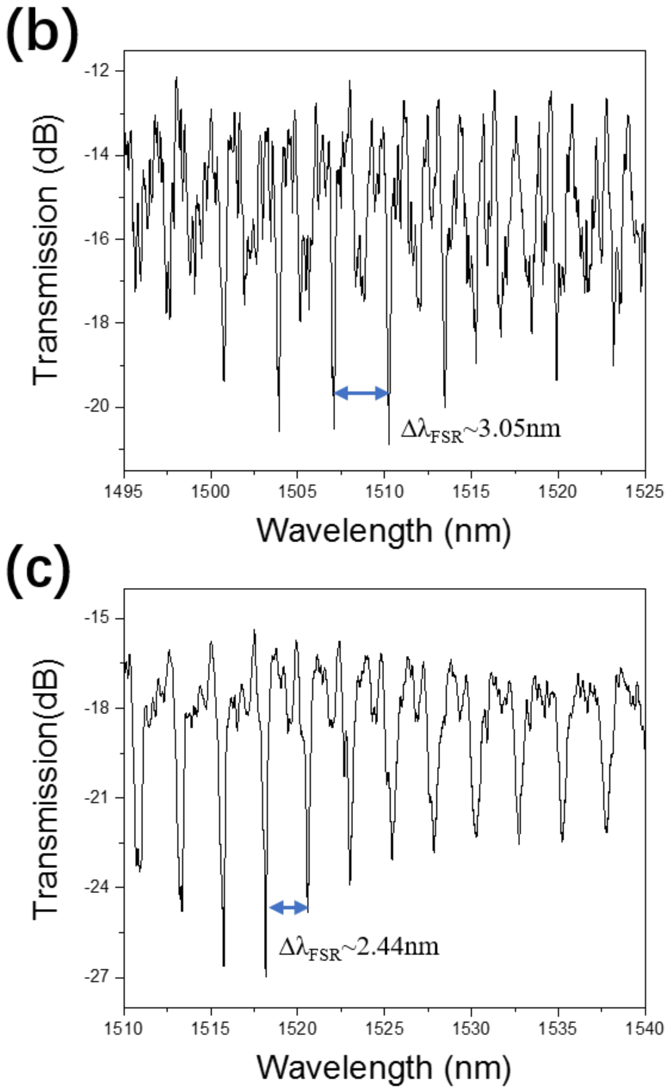

Figure 4.5 Transmission spectra of (a) WGMR-1, (b) WGMR-2, and (c) WGMR-3.

The tapered fiber was mounted onto a fixture connected to a 5-axis stage (MAX312D, KM100B, Thorlabs, Inc.), while the sample was placed on a 3-axis stage (MAX312D, Thorlabs, Inc.) so as to adjust finely the distance between the microcavity and tapered fiber. To observe the condition of coupling, two cameras (top-view, side-view) were used. In the measurement of transmission spectra, a wide band light source and an optical spectrum analyzer (OSA) with the resolution of 0.02 nm were used.

The measured transmission spectra of WGMR-1, WGMR-2, and WGMR-3 are shown in **Figure 4.5 (a)-(c)**, respectively. The WGM resonant peak can be observed clearly in the spectra. The measured average free-space ranges (FSR) of WGMR-1 to WGMR-3 are 3.75, 3.05, and 2.44 nm, respectively. The theoretical FSR can be estimated by:

$$\Delta\lambda_{FSR} = \lambda^2 / \left(2\pi nR\right), \tag{4.1}$$

in which n is refractive index of SU-8 resin at wavelength of 1550 nm, λ is the resonant wavelength, R is the radius of the microcavity. The theoretical FSRs of WGMR-1 to WGMR-3 are calculated to be around 3.91, 3.17, and 2.4 nm, respectively, which agree well with the measured results.

The FWHM of the WGM resonant peak of WGMR-1 to WGMR-3 are 0.152, 0.216, and 0.259 nm. The Q factor can be estimated by:

$$Q \approx \frac{\lambda}{\Delta\lambda_{FWHM}} \tag{4.2}$$

in which $\Delta\lambda_{FWHM}$ is the full width at half maximum of the Lorentzian-shape resonance peak, and λ is central wavelength of the resonant peak. The Q factors of WGMR-1, WGMR-2, and WGMR-3 are calculated to be around 9800, 7000, and 5800, respectively.

The fluorescent images of three groups of Rh6G-doped WGM microcavities are shown in **Figure 4.6**. The images were taken by fluorescent microscopy with excitation by a mercury arc lamp with a band pass filter with center wavelength of 532 nm.

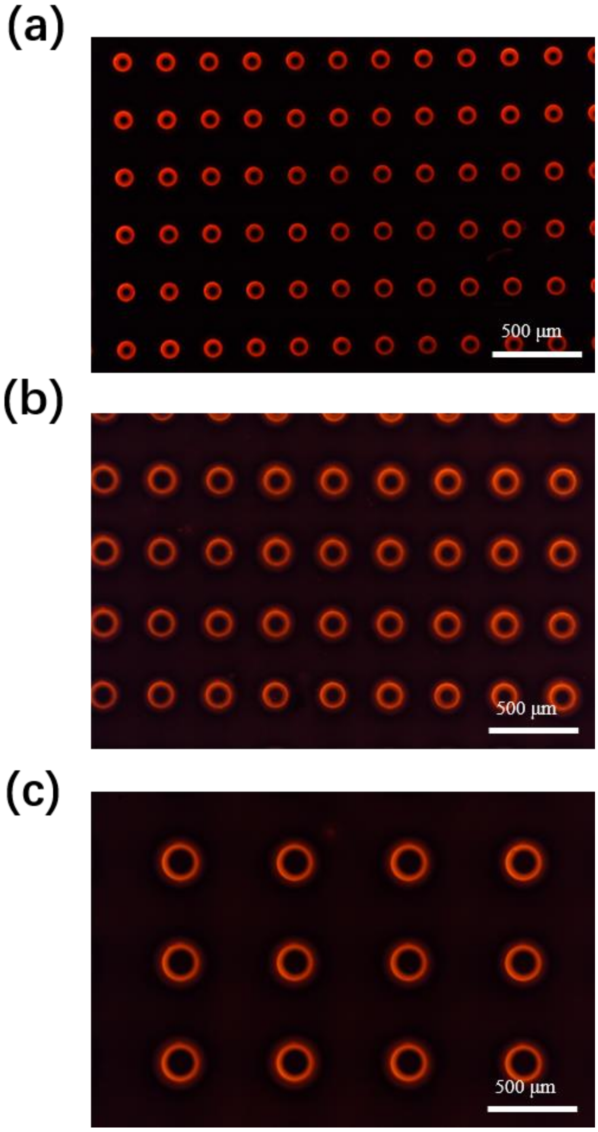

Figure 4.6 (a)-(c) are fluorescent images of WGMR-1, WGMR-2, and WGMR-3, respectively, with a thin layer of Rh6G.

In the fluorescent images, one can see the orange fluorescent light mainly distributed around the periphery of WGM microcavities for all three groups of microresonators, which may result from the fluorescent enhancement of the whispering-gallery mode. The fluorescent images also reveal that the uniformity of WGM microcavity array is good.

For the optical pumping test of WGM microlasers, a frequency doubled Nd:YAG pulse laser with center wavelength of 532 nm, pulse duration of 10 ns, and repetition rate of 10 Hz was utilized. A filter wheel with different neutral density filters was installed between the pump laser and an objective to control the pumping power. The objective converges pumping light into a multi-mode optical fiber with diameter of 105 nm that was used to guide the light and pump the microlasers in the equatorial plane of the suspended microdisk. To collect the light emitted from microcavity laser, another multi-mode optical fiber connected with spectrometer (SpectraPro 2750, Princeton Instruments Ltd.) was mounted and aligned in the equatorial plane.

The input-output curves and laser spectra of the three groups of WGM microcavities were shown in **Figure 4.7**. As shown in **Figure 4.7 (a)**, the laser threshold of WGM-1 is 0.218 nJ. The inset is its zoom-in fluorescent image. **Figure 4.7 (b)** shows the laser spectrum of WGM-1 at pump energy of 0.39 nJ, and the lasing mode spacing is 0.61 nm which can match with the diameter of WGM-1. For WGM-2, as shown in **Figure 4.7 (c)**, the threshold is 1.143 nJ. The laser spectrum at pump energy of 5.12 nJ are shown in **Figure 4.7 (d)** in which the lasing mode spacing is 0.53 nm. As shown in **Figure 4.7 (e) & (f)**, for WGM-3, the laser threshold is 1.232 nJ and lasing mode spacing is 0.36 nm.

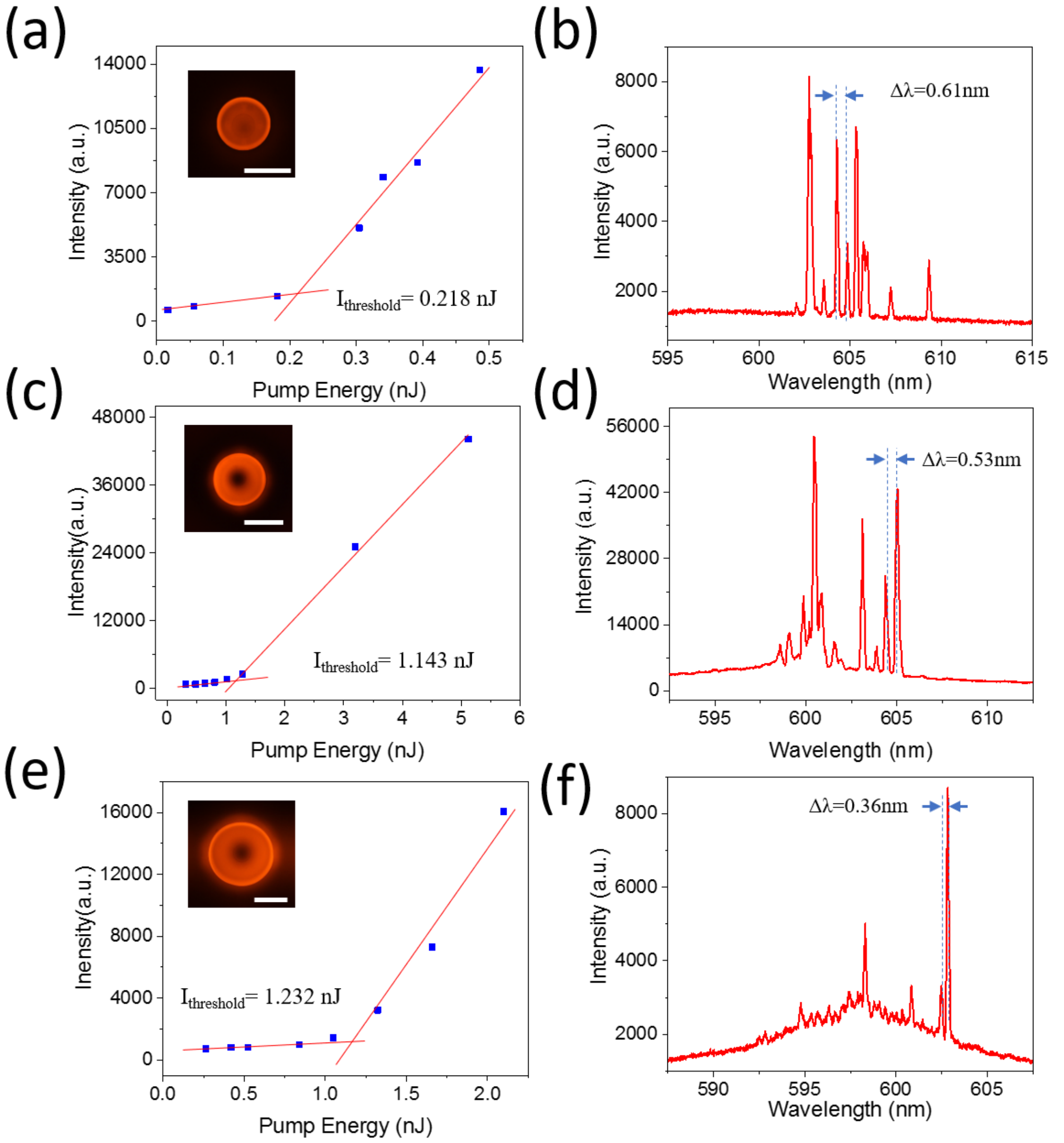

Figure 4.7 (a), (c) and (e) are measured input-output curves of microlaser made bythe WGMR-1, WGMR-2, and WGMR-3, respectively. (b), (d), and (e) are laser spectra of microlaser made bythe WGMR-1, WGMR-2, and WGMR-3, respectively.

It is known that lasing threshold of the WGM microlaser depends on effective mode volume and Q factor.[113] The lasing threshold of the microlasers could be inversely proportional to the Purcell enhancement factor *F* which can be described by [113, 220]

$$F = 3Q\frac{\left(\frac{\lambda_C}{n}\right)^3}{4\pi^2 V_{eff}} \sim \frac{Q}{V_{eff}}, \tag{4.3}$$

where λ_c represents central wavelength of lasing mode, n is refractive index of the microcavity, Q is quality factor, V_{eff} denotes the effective mode volume of the lasing mode. For qualitative analysis of the lasing thresholds, the Q factors in **Figure 4.5**, i.e. 9800 for WGM-1, 7000 for WGM-2 and 5800 for WGM-3 are considered. The effective mode volume can be calculated according to the formula[98]

$$V_{eff} = \frac{\int_V \varepsilon(\boldsymbol{r})\left|E(\boldsymbol{r})\right|^2 d^3\boldsymbol{r}}{\max\left[\varepsilon(\boldsymbol{r})\left|E(\boldsymbol{r})\right|^2\right]} \tag{4.4}$$

where $\varepsilon(\boldsymbol{r})$ represents the dielectric constant, and $\left|E(\boldsymbol{r})\right|$ denotes the electric field strength. For the fundamental modes of microlasers shown in **Figure 4.4**, the V_{eff} are around 7.56×10^3, 1.09×10^4, and 1.89×10^4 $(\lambda/n)^3$, respectively. It can be seen that the microlasers with largest F have lowest lasing threshold, which agree well the expected trend

4.5 Laser-intensity-modulation based biosensors and integrated optofluidic biochip

WGM microlasers can operate at low pump power and produce high-contrast-ratio light signal which are thus suitable to develop cost-effective laser-intensity-modulation-based biosensors for ultra-sensitive ELISA.

4.5.1 Design of optofluidic chip with microlasers

A design of optofluidic chip integrated with microlaser sensor array is shown in **Figure 4.8 (a)**. The fishbone-like micro channels were designed for integration of WGM microlasers and multimode optical fibers (MMOFs), in which the WGM microlasers located in the central main channels and MMOFs were inserted to the side channels. The microlasers are excited and collected by a pair of multimode optical fibers which are in the plane of microdisks. The optical fibers are placed perpendicularly to avoid that pump laser to be coupled into collecting optical fibers directly. As shown in the inset of **Figure 4.8 (a)**, the surface of microlaser is silanized to improve binding with antibodies because of electrostatic attraction[221]. As different concentration of antigen will cause color change of enzyme's substrate, it can be used as a detectable signal for biosensing. The higher concentration of antigen will lead to more optical loss of WGM microlasers and results in the lower laser intensity. The effective absorption length of the light can be increased by the high *Q* microcavities, which thus enhances the sensitivity of the laser-intensity based biosensors.

On the microfluidic part of the chip, eight inlets were designed for injection of antigens, antibodies, and enzyme's substrates for sandwich ELISA of VEGF, see **Figure 4.8 (b)**. The spiral microfluidic channel was designed for mixing color reagent for chromogenic reaction for ELISA. To achieve a sandwich ELISA, a surface should be prepared by binding capture antibody which can bind specifically with antigen, i.e. VEGF. The capture antibody was incubated over night at RT. For nonspecific binding sites, the surface is then blocked by adding Bovine Serum Albumin (BSA) after incubating 2 hours. After three times of standard washing procedures, the antigen-containing sample is applied to the surface and incubated for 2 hours at room temperature. After removing the unbound antigen, biotinylated detection antibody is added to bind with antigen specifically so as to form the 'sandwich' structure, i.e. antibody-antigen-antibody. Followed by washing out unbound biotinylated detection antibody, horseradish peroxidase (HRP)-streptavidin is added to bind with biotinylated detection antibody with biotin based on the strong streptavidin-biotin interaction. After washing out unbound HRP-streptavidin, enzyme's substrates, i.e. TMB reagents, are added and mixed in the mixer of microfluidic chip, which enables the optical loss-based biodetection.

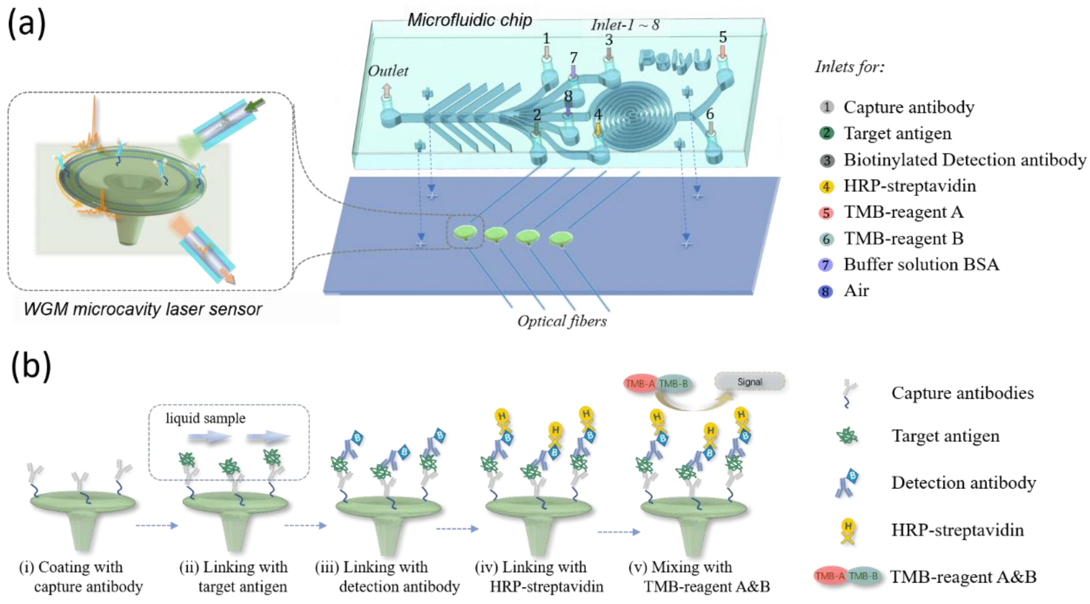

Figure 4.8 (a) Schematic of the optofluidic chip. (b) Surface functionalization of microlaser for VEGF detection.

4.5.2 On-chip integration of microlaser

The microfluidic chip was fabricated by the casting method with the SU-8 mold. [222] The mold of microfluidic chip, as shown in **Figure 4.9 (a)**, was also fabricated by optical μ-printed platform by using SU-8 2100 photoresist. The optical microscope images of the fabricated samples are shown in **Figure 4.9 (b)**. The height of microfluidic channel is around 150 μm which is compatible with the diameter of multimode optical fibers, i.e. 125 μm.

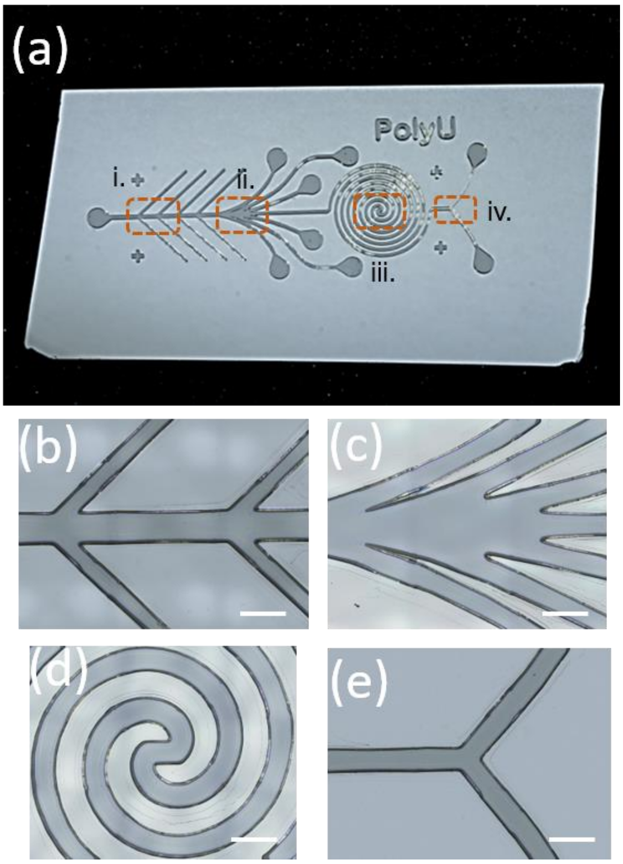

Figure 4.9 SU-8 mold of microfluidic chip. (a) Optically μ-printed microfluidic chip on silicon wafer. (b) to (e) are the microscope images of area i. to iv. in (a), respectively. The scale bars are 500 μm.

During casting process, PDMS precursor was firstly mixed with the curing agent (Dow corning Corporation) in the ratio of 11:1, and the mixture was poured into the pre-defined SU-8 mold. After degassing in the vacuum vessel, the mixture with mold was baked in the oven at 70 °C for 2 h. After that, the cured PDMS film with defined microfluidic channel was peeled off from the SU-8 mold.

As shown in **Figure 4.1 (b)**, after spin-coating of gain material-doped SU-8 upon all microcavities on the glass substrate, the surface of SU-8 WGM microcavities is modified for following processing:

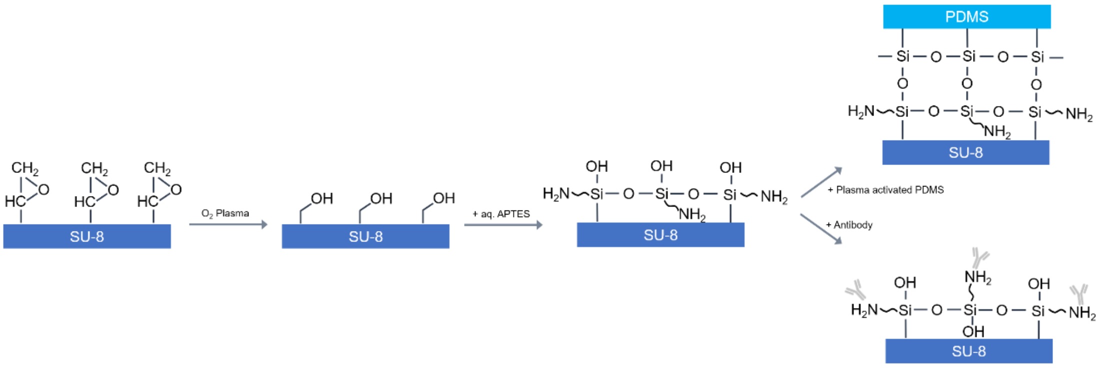

Figure 4.10 Surface modification of SU-8 WGM microcavities for binding antibodies

The surface of SU-8 WGM microcavities was silanized, as shown in **Figure 4.10**, to open the epoxy rings of SU-8 by oxygen plasma treatment (PDC-32G-2, Harrick Plasma Inc.) at RF power of 18 W for 3 min. Subsequently, the treated surface was immersed into 5% *v/v* aqueous (3-aminopropyl)triethoxysilane (APTES) solution in which the PH value was adjusted to around 4.0 for 30 min.[223] The PDMS microfluidic chip was treated by oxygen plasma for 3.5 min for surface activation. After that, with the assistance of 4 marks,s PDMS film with microfluidic channels and the glass substrate with microlaser array were well aligned and attached to form an optofluidic chip. The optofluidic chip was thereafter baked in the oven at 65 °C for 1 h, which forms irreversible binding between the PDMS film and the glass substrate with silanized SU-8.

4.5.3 Testing of biosensors for HRP

HRP-streptavidin (Solarbio Ltd., China), a kind of enzyme, is widely used in the chromogenic reaction in ELISA. An enzyme's substrate, 3,3′,5,5′-tetramethylbenzidine (TMB, Solarbio Ltd., China), can be catalyzed by HRP, which will cause color-changing effect in the solution.

The HRP-streptavidin solution with the concentration of 500 ng/mL was prepared by dissolving the stock solution in 0.1 M 0.2-um-filtered phosphate buffered solution (PBS). Then, the enzyme's substrates, including 50 μL color reagent TMB-A and 50 μL TMB-B, were mixed together. After that, 20 μL 500 ng/mL HRP-streptavidin solution was mixed with 80 μL mixture of enzyme's substrates, which is incubated in room temperature (RT) for 40 min before measurement of the absorbance spectra.

As shown in **Figure 4.11**, there are two absorption peaks in the mixture of enzyme's substrates and HRP-streptavidin, which confirms that the substrates were catalyzed by HRP. The strongest absorption peak locates at around 650 nm, and the absorption at around 600 nm is still strong at which the laser peaks locate.

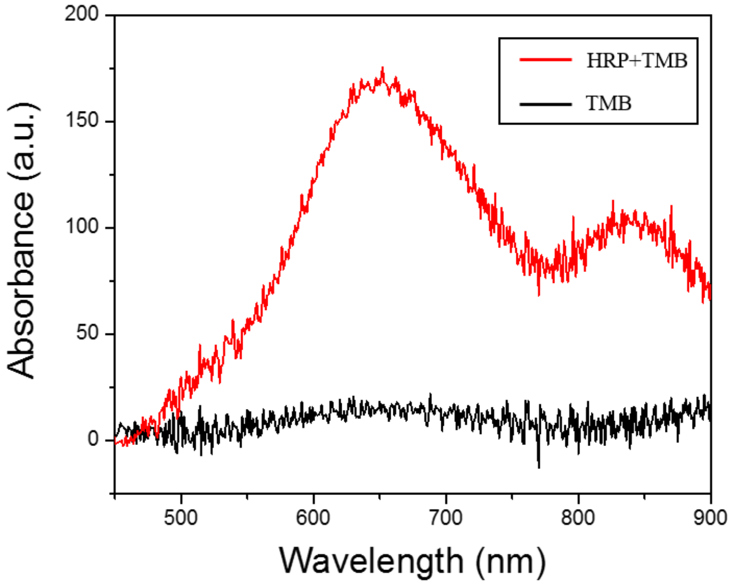

Figure 4.11 Absorbance spectra of TMB.

The photograph of the fabricated optofluidic chip is shown in **Figure 4.12 (a)**. The area of red frame is microlasers coupled with multimode optical fibers whose zoom-in image is shown in the inset. During the testing of HRP, the mixture of enzyme's substrate was injected from inlet 5, while the HRP-streptavidin solution was injected from inlet 6. Then the solution was mixed by the on-chip mixer, and flow into the sensing area for incubation of 40 min. As shown in **Figure 4.12 (a)**, the laser intensity of the laser peak at around 603.5 nm (measured by HR4000, Ocean Optics Inc.) was measured in mixture of enzyme's substrates and HRP-streptavidin with different concentration. The pump energy was around 0.39 nJ. It can be seen the relation is close to linear in the log-log scale, which confirms the Beer-Lambert law. The error bars represent standard deviation of laser intensity in 10 measured spectra per data point .

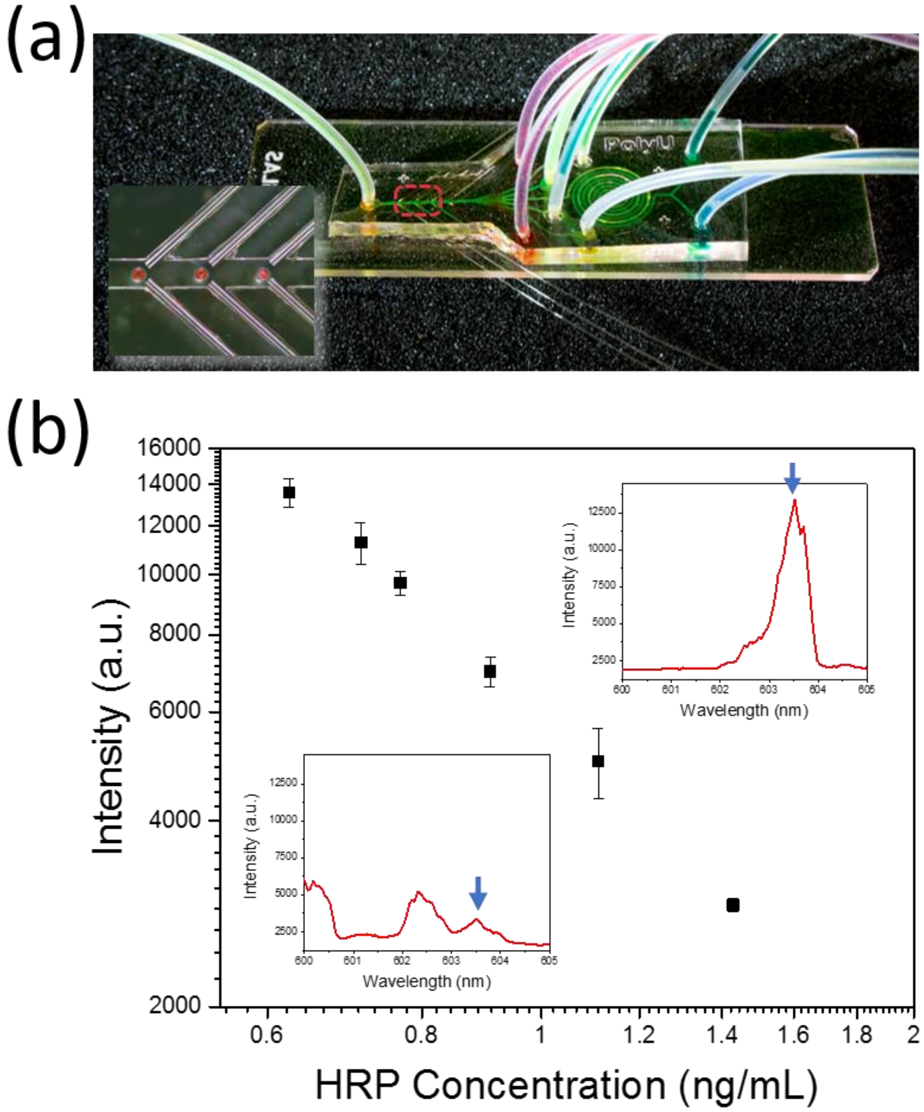

Figure 4.12 HRP sensing in optofluidic chip. (a) Photograph of fabricated optofluidic chip. Inset: zoom-in microscope image of the highlight area. (b) Laser intensity as a function of HRP concentration. Right-top and left-bottom insets are the laser spectra corresponding to the HRP-streptavidin concentrations of 0.625 and 1.43 ng/mL, respectively.

The limit of detection (LOD) can be estimated according to LOD=3S_a/b, [224] where b represents the slope of linear relation, S_a is the standard deviation of microlaser. Here, we fit the relation between the concentration of analyte and laser intensity by using

$$\log(\frac{I_0}{I}) = c\cdot\log(x)+d\ , \tag{4.5}$$

where I is laser intensity, I_0 represents the laser intensity of lowest concentration of analyte in experiment, x is the concentration of analyte, c and d are coefficients. The LOD was estimated by using the slope of Eq. 4.5 at I_0. For laser-based HRP biosensor, the LOD was calculated to be 0.3 ng/mL.

4.5.4 Testing of biosensors for VEGF

The on-chip ELISA procedures of VEGF were processed as mentioned in section 4.5.1. The chromogenic reaction in the ELISA will proceed in the sensing area of the optofluidic chip, in which the optical loss caused by the reaction is related to concentration of VEGF and will thus reduce the laser intensity. **Figure 4.13** plots the sensing signal of on-chip ELISA microlaser sensor under different pumping laser energy. As shown in **Figure 4.13 (a)**, the intensity of laser with the emission peak at 604.3 nm was tracked for detection of VEGF concentration from 65 fg/mL to 10^3 fg/mL when the pumping energy is 0.39 nJ. The relation between the laser intensity and VEGF concentration is linear in log-log scale. When the concentration of VEGF is lower, the laser intensity is higher as the VEGF binds with biotinylated detection antibody leading to less HRP on the surface of microlaser. The HRP produces the chromogenic reaction with TMB. When the concentration is high enough, the laser peak will become weaker and eventually extinct because of higher optical loss.

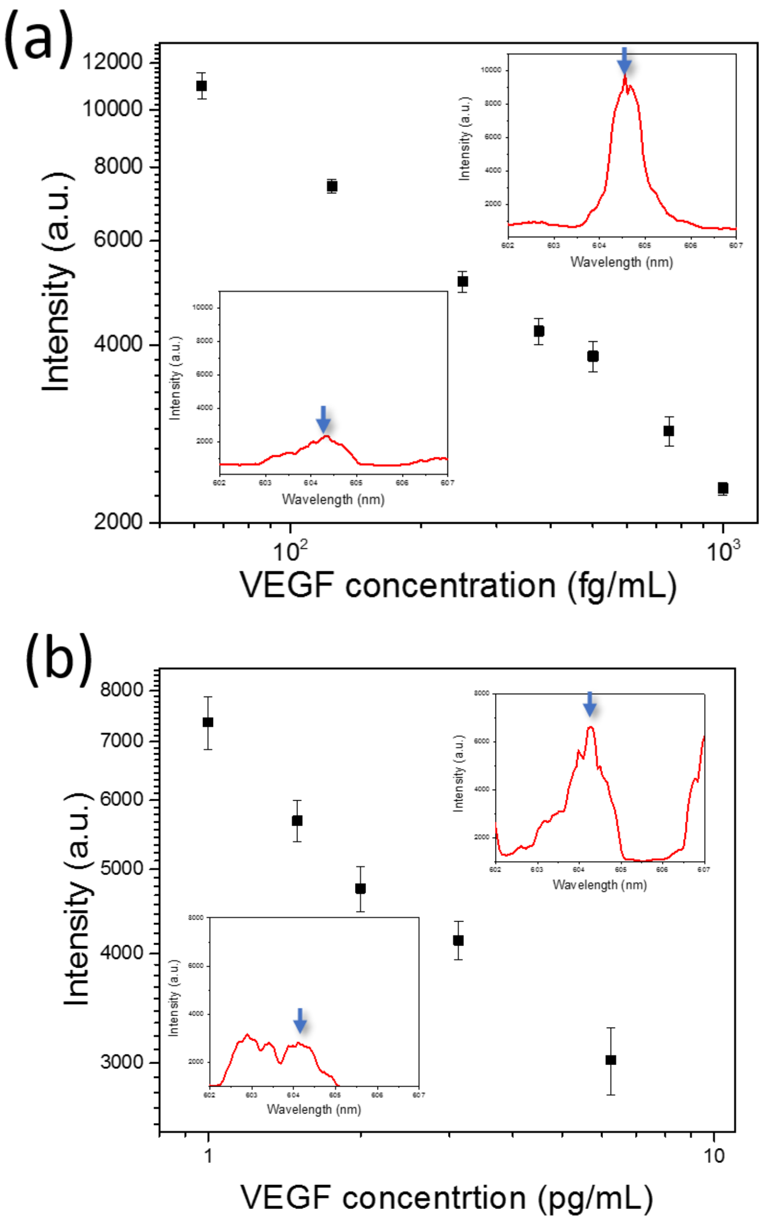

Figure 4.13 Measurement of VEGF under pump laser energy of (a) 0.39 nJ and (b) 0.98 nJ. Right-top and left-bottom insets in (a) are the laser spectra when the VEGF concentrations are 65 and 10^3 fg/mL, respectively. Right-top and left-bottom insets in (b) are the laser spectra when the VEGF concentrations are 10^3 and 6.25×10^3 fg/mL, respectively.

To extend the sensing range of VEGF, the pump laser energy can be enlarged so as to overcome the optical loss to support laser operation. As shown in **Figure 4.13 (b)**, the laser peak appeared again when the pump energy was increased to 0.98 nJ. The sensing range was extended up to

6.75×10^3 fg/mL. The LOD of the microlaser biosensor for VEGF under pumping energy of 0.39 nJ was calculated to be 17.8 fg/mL.

TABLE 4.1 Comparison of analytical performance of immune-based biosensor for detection of VEGF.

Sensors	**Detection scheme**	**LOD**	**Ref.**
SEARS-Microdroplet Sensor	Magnetic-field amplified SERS	1 fg/mL	[225]
1D Photonic Crystal Sensor	Bloch surface wave	650 fg/mL	[226]
Paper-based Sensor	Colorimetric determination	30 fg/mL	[227]
Nanostructured Microfluidic Array Sensor	Au nanoparticle immunoarray	10 fg/mL	[228]
Hollow Gold Nanosphere Sensor	SERS	1-10 pg/mL	[229]
Polymer WGM Microlaser Sensor	WGM microlaser intensity	17.8 fg/mL	this work

Notably, the LOD of this work is comparable to the Surface Enhanced Raman Scattering (SEARS)-Microdroplet sensor whose LOD is 1 fg/mL. However, as only polymer material and portable spectrometer were used in this work, the cost of WGML based opto-bio-microsystem was much lower than SEARS biosensor, which provide a promising cost-effective devices for portable poin-of-care diagnostics.

4.6 Summary

In summary, low-threshold WGM microlaser array was fabricated and integrated into a microfluidic chip to develop an optofluidic chip for ultrasensitive detection of VEGF. With the improved optical μ-printing platform, the suspended microdisks array were fabricated whose *Q* factor can reach 9800. A thin layer of SU-8 resin with gain media was spin-coated on the microdisks so as to support low-threshold laser oscillation in which the threshold as low as 0.218 nJ. The low-threshold microlasers were integrated into a microfluidic chip to achieve a platform for laser-based ELISA detection of VEGF. Compared with commercial ELISA kit with sensitivity of 5 pg/mL, highest sensitive microlaser biosensor of VEGF has the LOD of 17.8 fg/mL. Such a low-cost WGM microlaser-based biochip shows great potential in the applications of ultrasensitive chromogenic detection of biomarkers.

Chapter 5

Direct μ-Printing of Cellular-scale Microscaffold Arrays for 3D Cell Culture

5.1 Introduction

The production of 3D microstructures for mimicking realistic in vivo conditions was first demonstrated by Yamada *et al*[34]. In his work, cell-derived 3D matrices were utilized in cell culture, which demonstrates narrower integrin usage and better cell biological activities compared with 2D cell culture. Although the matrices based on fibrous collagen can recapitulate the physiologically related 3D environment *in vitro*[230, 231], cell shape cannot be controlled by the matrices whose mechanical property tend to be altered during cell culture[232]. Therefore, for bioprinted constructs with composition heterogeneity[233], three-dimensional fabrication technologies based on droplet (e.g., inkjet bioprinting[234, 235], microextrusion bioprinting[236, 237], and laser-assisted bioprinting[238, 239]) have been proposed to generate 3D environments for tissue and organ engineering[13]. Although the droplet-based bioprinter offer the affordable and versatile fabricating methods with reasonable resolution for biological constructs[14] , it is challenging to print porous or suspended structures with controlled topographies[240]. In addition, the other two limitations of droplet-based bioprinter, poor assembly to the substrate and inability to fabricate of structurally well-integrated architectures[241], make researcher seek fabricating methods for detailed biological constructs. Due to the submicrometer feature size and precision[168], the two-photon absorption based direct laser writing is capable to fabricate the standardized and controlled 3D scaffolds for the investigation of cell behaviors[242]. Via two-photon polymerization(i.e., non-linear-optical process happens in very focus of laser beam[45]), an extensive range of characteristic microstructures were fabricated for investigation of cell mechanics[44, 142, 243], cell morphology[151, 152, 244], and cell migration[245-247]. However, the two-photon polymerization based fabricating technology exhibits relatively low efficiency on fabrication of large quantities of detailed structures, since only one submicrometer-scale point in the bulk of photoresist can be polymerized at one time[45]. It takes even more time when the biomaterials with low photosensitivity are utilized to fabricate detailed 3D structures. Moreover, for biomaterials, the two-photon absorption cross-section of photoinitiators is typically small, which requires both high concentration of the photoinitiators and high laser power during photopolymerization [152, 248]. The requirement will limit the biocompatibility of the fabricating process [249].

In this chapter, we present a new optical 3D bioprinting technology which integrates dynamic optical projection stereolithography (DOPsL) with machine vision metrology. An optical 3D μ-printing technology was developed to use a polymer material (SU-8 resin) with good chemical resistance and mechanical property to fabricate a series of 3D micro cubic microscaffolds. The sizes of the cubic microscaffolds match with the size of cells, which enable us to investigate the cell behavior in engineered 3D microenvironment. What's more, an in-situ printing technology was developed so as to pattern the bioactive material, i.e. gelatin methacrylate (GelMA), on the bioinert suspended frames, which can influence the cell spreading geometrically. The two-material based optical μ-printing technology enable to fabricate biomimetic 3D microstrucutres with engineered geometry and materials for study on controllable cell spreading.

5.2 Fabrication of cellular-scale microscaffold arrays

Figure 5.1 shows a schematic representation of the optical μ-bioprinting platform based on a high-speed spatial light modulator, i.e. digital micromirror device. The CAD model of designed scaffolds was sliced into 100 layers which flowed into DMD chip. Illuminated by the collimated UV light, the DMD chip dynamically reflected the light with certain patterns according to the data of layers. The key contributor of high efficiency of DOPsL is the DMD chip which contains a million of micro mirrors and can switch the whole exposing pattern within 30 μs. The patterns were projected upon the photoresist which is spin-coated on glass slice through the projection optics. The projection optics here was carefully adjusted and can achieve 600-nm resolution which is sufficient for fabrication of scaffolds and for in-situ modification. In order to fabricate arrays of architectures, XY-Nanopositioning stage was utilized to locate the exposure area and realized seamless pattern-stitching technique. For right exposing position in the process of in-situ modification, CCD camera can assist to trace the location of fabricated structures. The duration of UV exposure is 55 seconds in fabrication process, which is much faster than two-photon polymerization based direct laser writing.

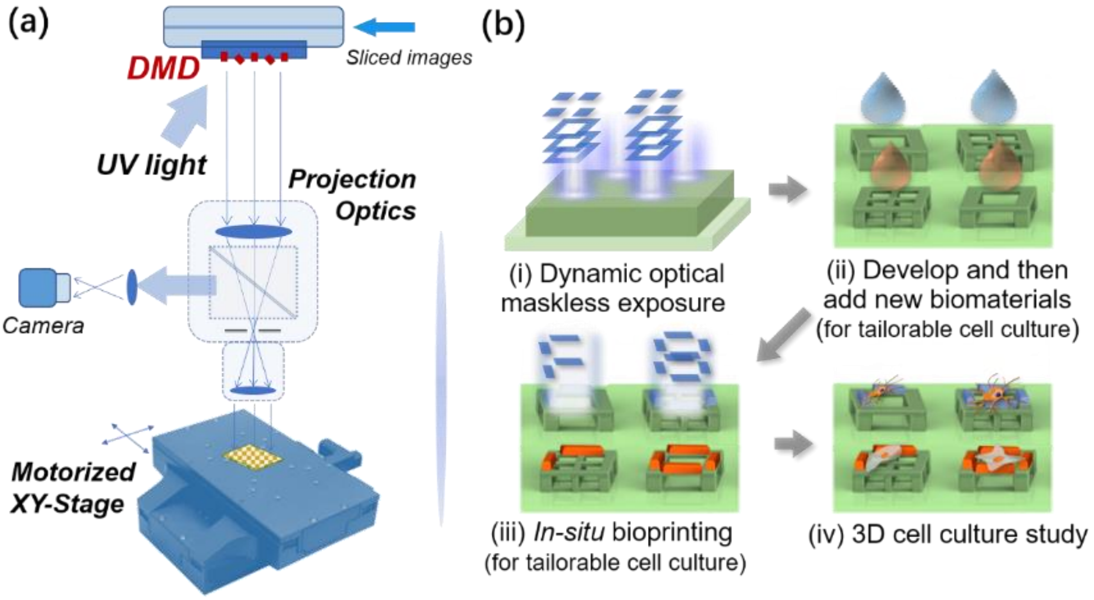

Figure 5.1 (a) Schematic illustrations of the DMD based optical µ-bioprinting technology (b) Process of optical in-situ bioprinting: (i) exposure of SU-8 photoresist by UV light with designed pattern; (ii) the fabricated architecture array coated with biomaterials; (iii) in-situ printed biomaterials on specific area of architectures; (iv) controlled cell culture study on the modified architectures.

To prepare SU-8 photoresist, 4-((2-hydroxytetradecyl)oxy)phenyl)-

phenyliodoniu (PC-2506) and Tributylamine (TBA) are used as the photo initiator and inhibitor, respectively. To control the penetration depth of UV light, 2-(2H-Benzotriazol-2-yl)-4,6-bis(1-methyl1-phenylethyl)phenol (TINUVIN 234) was used as light absorber agent. For preparation of photosensitive SU-8 resin, EPON SU-8 resin and above-mentioned chemical reagents was dissolved in a weight ratio of SU-8: PC-2506: TBA: TINUVIN 234 = 100: 2.5: 0.14: 0.2.

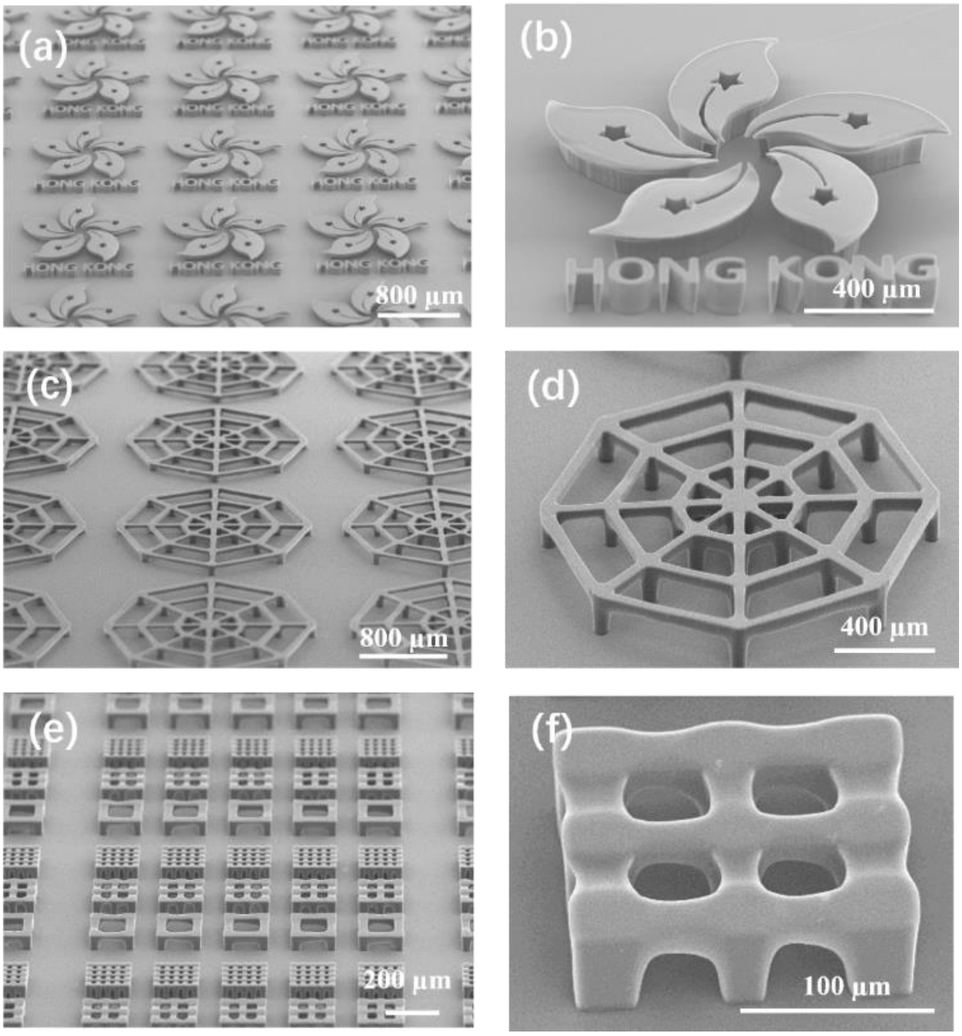

Figure 5.2 SEM images of the fabricated 3D microstructures. (a) Hong Kong Bauhinias. (b) Uplifted micro spider web. (c) 3D cubic microscaffolds. (b), (d) and (f) are zoom-in images of (a), (b) and (c), respectively.

Before fabrication of bioinert 3D microstructures, a thin layer of SU-8 (~1 μm) was spin-coated and cured upon a clean glass slice as a buffer layer, which improves the adhesion between glass slice and polymer microscaffolds. The thickness of buffer layer is around 1 μm. A thick layer of SU-8 with 40 μm was spin-coated on buffer layer and was soft baked at 65 °C for 5 minutes and 95 °C for 15 minutes to remove solvent. When the sample was cooled down to room temperature, as shown in Fig. 1(b), UV light source (159.12 mW/cm^2, 55s) was utilized during the exposing process. After exposure, the sample was post baked at 65 °C for 5 minutes and 95 °C for 20 minutes and developed in propyleneglycol monomethylether acetate (PGMEA) for 13 minutes.

To demonstrate the versatility of the system, besides arrays of microscaffolds, we fabricated Hong Kong Orchid and cobweb-like structures (**Figure 5.2**).

5.2.1 Design and fabrication of cellular-scale microscaffold arrays

The microscaffolds comprised flatten beams which were arranged as a cube-like architecture **(Figure 5.3**). We are interested in the influence of dimension of cubicle on the cell behavior.

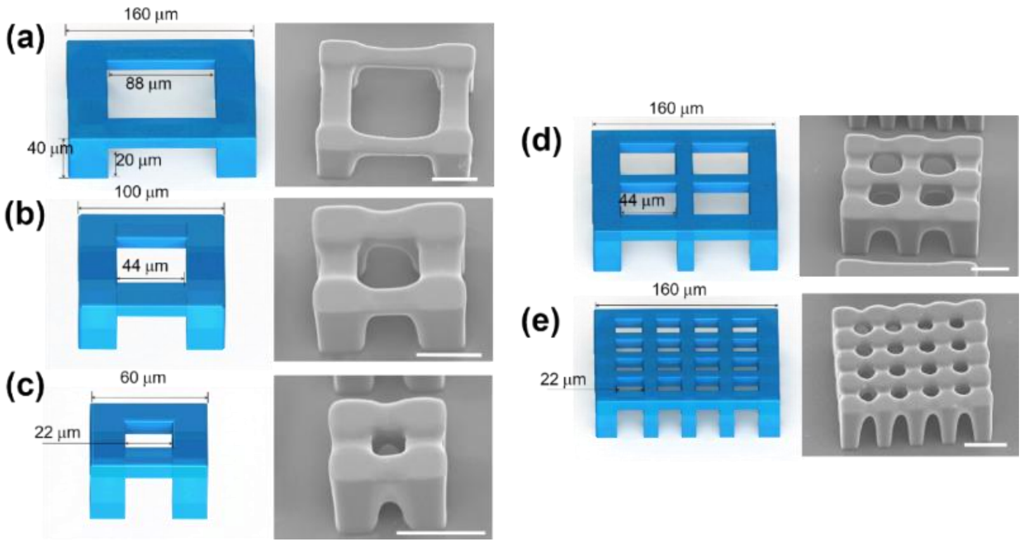

Figure 5.3 The designed structures and the corresponding SEM images of the 3D cubic microscaffolds. Scale bar = 50 μm.

In the first and second scaffolds, as shown in **Figure 5.3 (a) & (b)**, the length of side of hole are quad and double comparing the third one, so that the cell will stretch more on the scaffolds. In **Figure 5.3 (c)**, The scaffolds with one smallest hole (22×22 μm) were carefully designed to match dimension of one cell. For another set of scaffolds, as shown in **Figure 5.3 (d) & (e)**, cubic microscaffolds with different combination were fabricated, which can be used for study of cell-cell interaction.

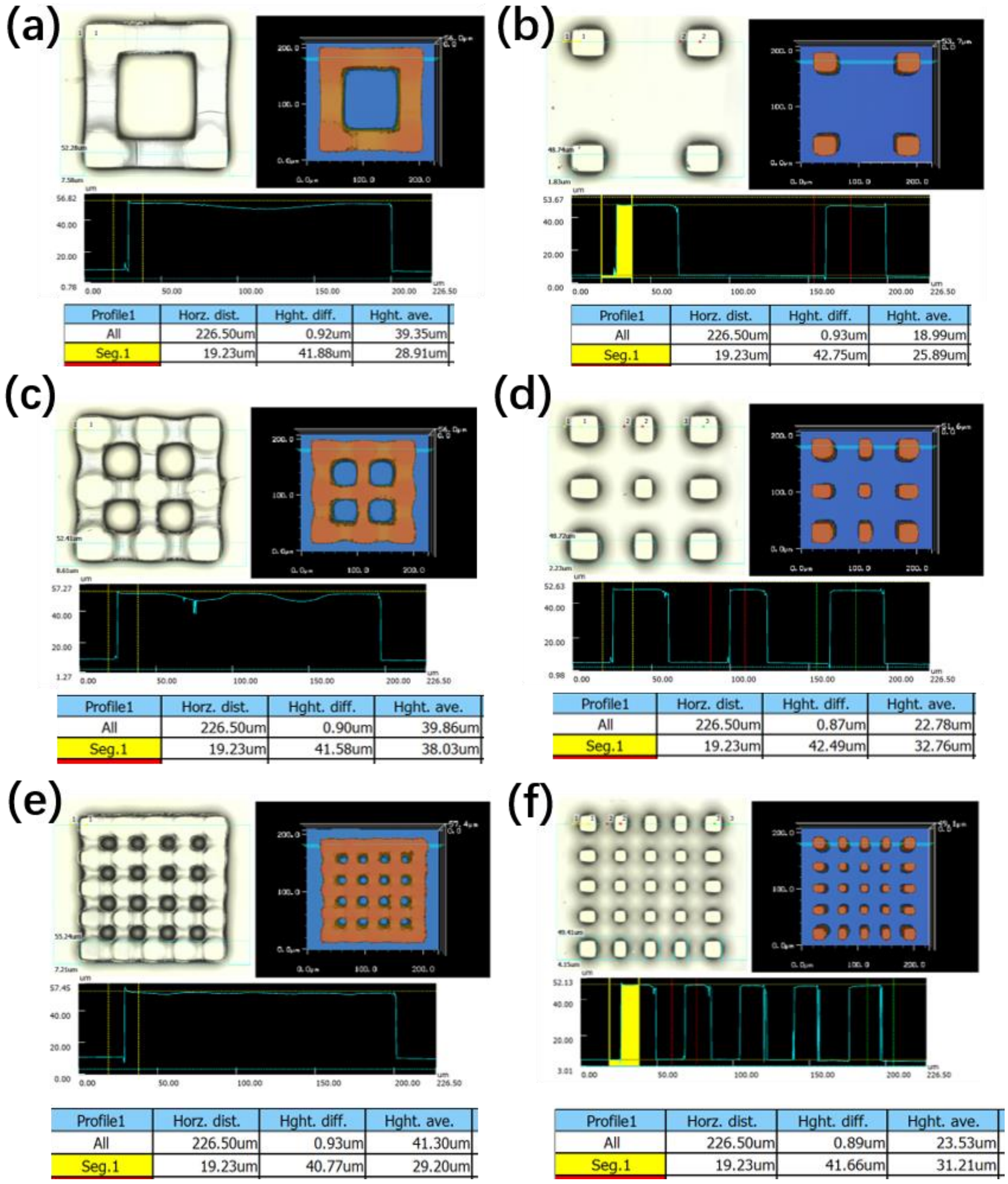

(a)

Profile1	Horz. dist.	Hght. diff.	Hght. ave.
All	226.50um	0.92um	39.35um
Seg.1	19.23um	41.88um	28.91um

(b)

Profile1	Horz. dist.	Hght. diff.	Hght. ave.
All	226.50um	0.93um	18.99um
Seg.1	19.23um	42.75um	25.89um

(c)

Profile1	Horz. dist.	Hght. diff.	Hght. ave.
All	226.50um	0.90um	39.86um
Seg.1	19.23um	41.58um	38.03um

(d)

Profile1	Horz. dist.	Hght. diff.	Hght. ave.
All	226.50um	0.87um	22.78um
Seg.1	19.23um	42.49um	32.76um

(e)

Profile1	Horz. dist.	Hght. diff.	Hght. ave.
All	226.50um	0.93um	41.30um
Seg.1	19.23um	40.77um	29.20um

(f)

Profile1	Horz. dist.	Hght. diff.	Hght. ave.
All	226.50um	0.89um	23.53um
Seg.1	19.23um	41.66um	31.21um

Figure 5.4 The laser scanning confocal images of microstructures. The height of fabricated microstructures from (a) to (f) is 41.88μm, 42.75μm, 41.58μm, 42.49μm, 40.77μm, and 41.66μm respectively.

The area of single hole of fabricated scaffolds with 4×4 holes, 2×2 holes and 1×1 hole is 22×22 μm, 44×44 μm, and 88×88 μm, respectively. The size of inner opening support cells with different extend of spreading. The different combinations mode (4×4 and 2×2) provides 3D environments by which cell-cell interaction can be studied. Due to proximity effects, the overhanging beams shrink, which can be fixed by adjusting the 3D models. The surfaces of fabricated architectures are smooth. It is shown that the beams of cube-like microscaffolds are not very flat, which is caused by insufficient soft bake of SU-8 photoresist. Because of insufficient soft bake, solvent is still in the photoresist and make it easy to be distorted. The design of pillars' height is also 40 μm, which is the same as experimental groups (**Figure 5.4**). In printing process of both microscaffolds and micropillars, SU-8 photoresist was spin-coated on glass slice in 4200 rpm for 40s, so that thickness of photoresist can be control in around 40 μm. Laser scanning confocal images shows that the height of fabricated microstructures is closed to the design.

5.2.2 Cell culture on micoscaffolds without selective bioactivation

For improvement of cell adhesion and attachment on the SU-8 microscaffolds, a universally adhesive polydopamine layer was coated on the surface the microscaffolds. The fabricated microscaffolds were immersed in dopamine solution in which Tris-HCl buffer with pH = 8.5 was added in 1 mg/ml dopamine and incubated for 4 h. Then the microscaffolds were rinsed with phosphate buffer saline (PBS), and sterilized by UV irradiation before the cell experiment.

The 40 μm-height microscaffolds can prevent the cells that spread on the overhanging beams of the microscaffolds form adhering to the underlying substrate. However, in the “no-beam” group, especially in the pillars array with large spacing, the cells can hardly suspend among the top of the pillars, and hence indeed adhered on the surface of underlying substrates. This phenomenon demonstrates the essential of the overhanging beams. Meanwhile, we also noticed that there were indeed some cells adhered to the space among the microscaffolds on bottom of the substrates, but these cells have already been excluded from the analysis and statistics, and thereby would not affect the final results.

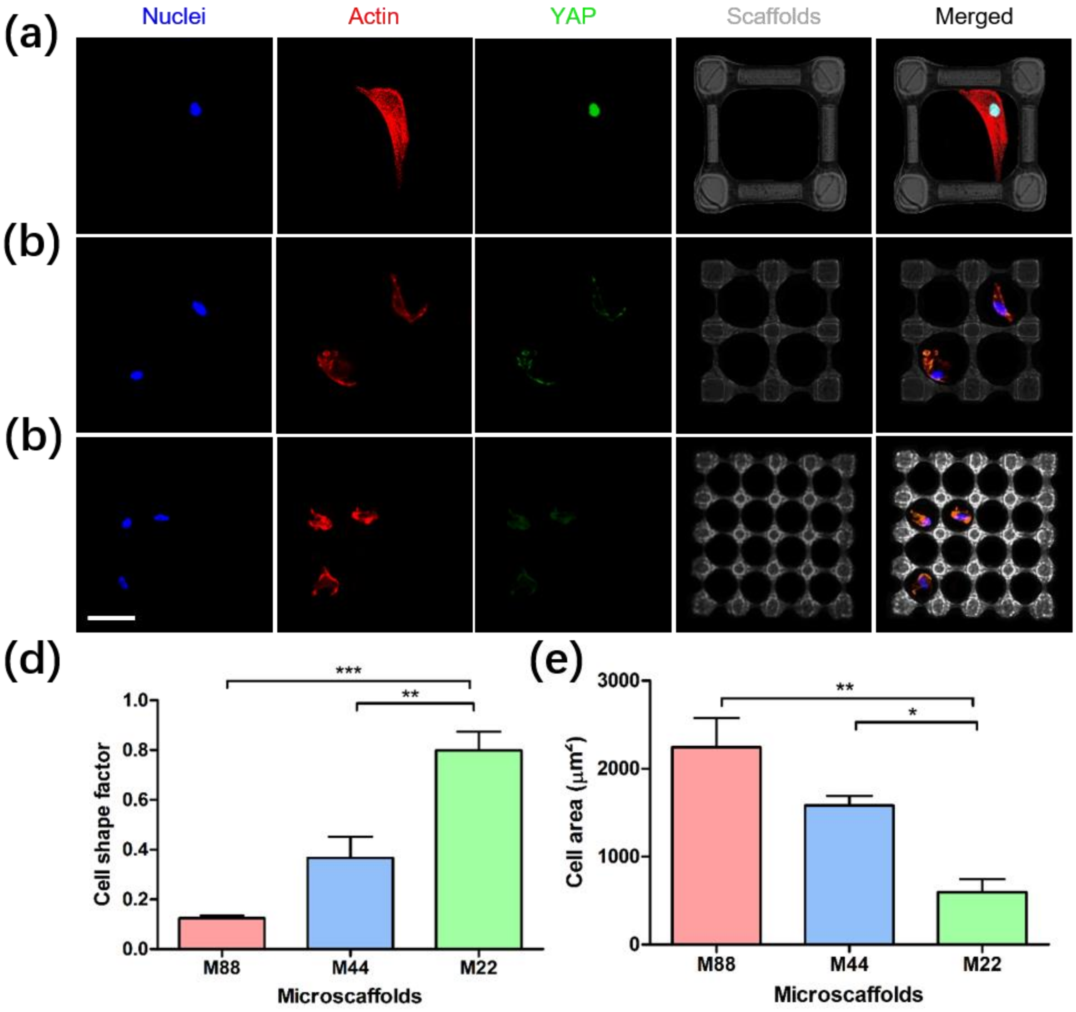

Figure 5.5 Fluorescent images of the hMSCs cultured in the 3D cubic microscaffolds with different cubicle sizes: (a) 88×88 μm^2 ("M88"), (b) 44×44 μm^2 ("M44"), and (c) 22×22 μm^2 ("M22") for 24 h. (d) Average cell shape factors and (e) average cell area of hMSCs cultured in the microscaffolds. *$p < 0.05$, **$p < 0.01$, ***$p < 0.001$. The error bars are based on observation over 20 cells per group. The cells were fluorescently stained by antibodies against YAP and goat anti-mouse IgG containing Alexa488 for YAP observation, by phalloidin-TRITC for cytoskeleton, and by (4′,6-Diamidino-2-phenylindole) DAPI for nuclei. Scale bar = 50 μm.

Figure 5.5 (a)-(c) shows that the fluorescent images of hMSCs were seeded on the multi-cubic microscaffolds. One can see that the cells only attached on and spread over a single opening rather than spread across it.

In **Figure 5.5 (d) and (e)**, it is shown that the extent of cell spread on multi-cubic microscaffolds shows similar trend with those in single-cubic microscaffolds. To reveal development of the cell cytoskeletal tension, we performed the immunostaining against yes-associated protein (YAP) which is a main mechanotransduction factor. It can be seen in Figure 5.5 that the fluorescent against YAP is brighter when the cell is on the scaffolds with larger opening, which indicate the cell cytoskeletal tension is larger. The cell shape factor is given by $f = 4\pi a/P^2$ where a is area and P is perimeter. The smaller f of cells in larger microscaffolds indicates that the cells tend to spread alone the beam of scaffolds instead of maintaining the initially circular shape. The activity of YAP is also reported to be closely involved in stem cell differentiations. In particular, osteogenic differentiation of stem cells has been shown to be positively correlated with YAP activity, which indicates that the microscaffolds with larger openings can enhance osteogenesis during cell differentiation.

5.3 Optical patterning of GelMA

Gelatin has been extensively used as scaffold material for tissue engineering due to its good biocompatibility and bioactivity, such as the support on cell adhesion via its RGD tripeptide sequence [250]. The photo-crosslinkable gelatin methacrylate (GelMA) is a popular biomaterial for 3D bioprinting. To synthesize gelatin methacrylate, 100 mL PBS was utilized to dissolved 10 g gelatin (type A) at 50 °C, and followed by adding Methacrylic anhydride (12 mL). The reaction between the two materials proceed for for 4 h at 50 °C under continuously stirring. It took the resulting mixture 6 days to dialyze against DI water, and then the mixture was then lyophilized. The degree of substitution determined by ^{1}H NMR was 3.17 × 10^{-4} mol/g.

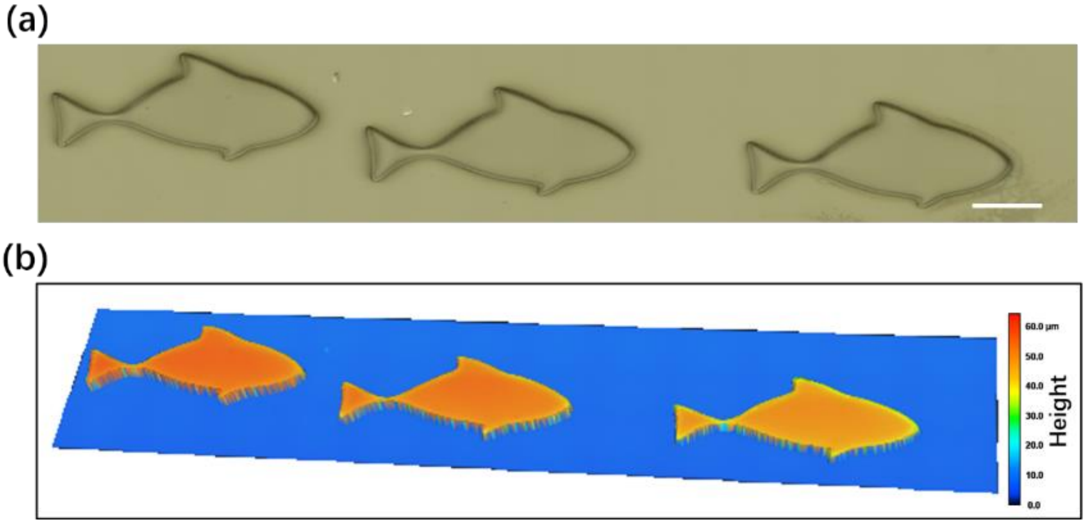

Figure 5.6 Optical microscopic image (a) and laser-scanning confocal 3D image (b) of GelMA fish.

For preparation of photo-crosslinkable 13% GelMA solution, 1 mL deionized (DI) water was utilized to dissolve 0.2 g GelMA at 35 °C for 6 hours. Then 2,2,6,6-tetramethylpiperidine 1-oxyl (TEMPO) 0.0045g, acrylic acid (AA) 0.03g, Irgacure 2959 0.02g and 2-hydroxy-4-methoxybenzophenon-5-sulfonic acid (HMBS) 0.005g were mixed within the GelMA solution as free-radical quencher, solvent of Irgacure 2959, free-radical generator, and UV absorber, respectively, and stirred at 35 °C for 12 hours.

Figure 5.6 shows fishes made by GelMA. By applying different exposure dose, the height of the fishes from left to right, as shown in **Figure 5.6**, can be tailored as 39.5, 44, and 47.7 μm, respectively.

5.4 Selectively bioactivated microscaffold for cell culture

5.4.1 In-situ printing of selected-bioactivated microscaffold

As shown in **Figure 5.1 (b)**, for study on guided cell adhesion and spreading, the surfaces of the 3D cubic microscaffolds were selectively printed with the photo-crosslinable GelMA by the optical μ-printing technology.

Because of the hydrophobicity and low surface energy of the surface of SU-8, the bioactive material is difficult to be coated on surface of SU-8 3D microstructures. As a result, for enhancement of adhesion of GelMA on surface of SU-8, oxygen plasma treatment was utilized. The dose of oxygen plasma treatment was carefully optimized, because the excessive treatment will reduce the discrepancy of the cell-adhesion properties between the SU-8 microstructures and GelMA patterns [251]. O_2 plasma cleaner (PDC-32G-2, Harrick Plasma.) was utilized in the treatment of SU-8 microstructures. The fabricated SU-8 scaffolds were treated at low, middle, and high-radio-frequency power for 10 s each time. In **Figure 5.1b (ii)**, prepared GelMA was dropped on the oxygen-plasma-treated microstructures through a pipette. With the help of the integrated machine-vision metrology and the high-precision motorized stage, the ultrafine alignment can be realized, which enables us to project optical patterns on the small targets of the microstructures precisely. For polymerization of bioactive GelMA only on the top surface of the suspended beams of the microscaffolds, an objective with short focal depth (~10 μm) was utilized in the projection optics of the setup.

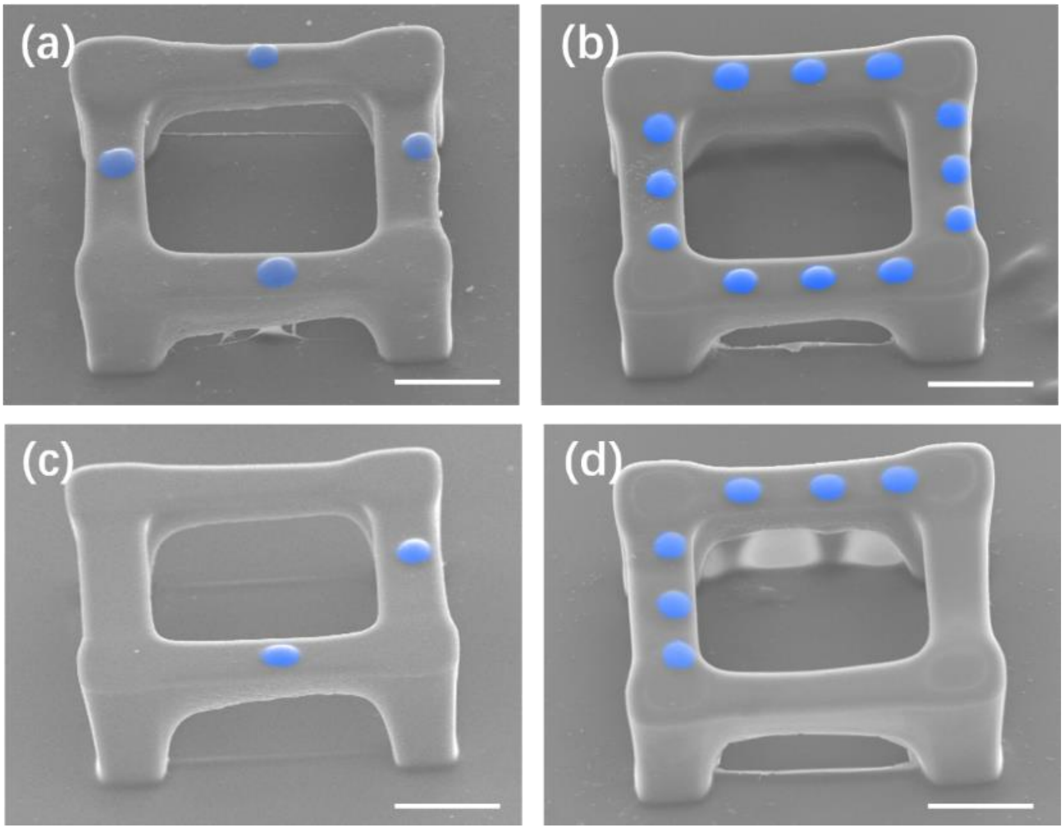

Figure 5.7 SEM images of the 3D cubic microscaffolds with *in-situ* printed GelMA patterns (highlighted in blue). Scale bar = 50 μm.

Figure 5.7 shows a series of patterns of GelMA (highlighted in blue) which were printed on the top surface of the SU-8 cubic microscaffolds. The total time of UV exposure was 30 s with the UV light intensity of 133.96 mW/cm^2. After exposure process, the samples were developed in DI water at 33 °C for 30 min.

5.4.2 Microscaffold for controlled cell behavior

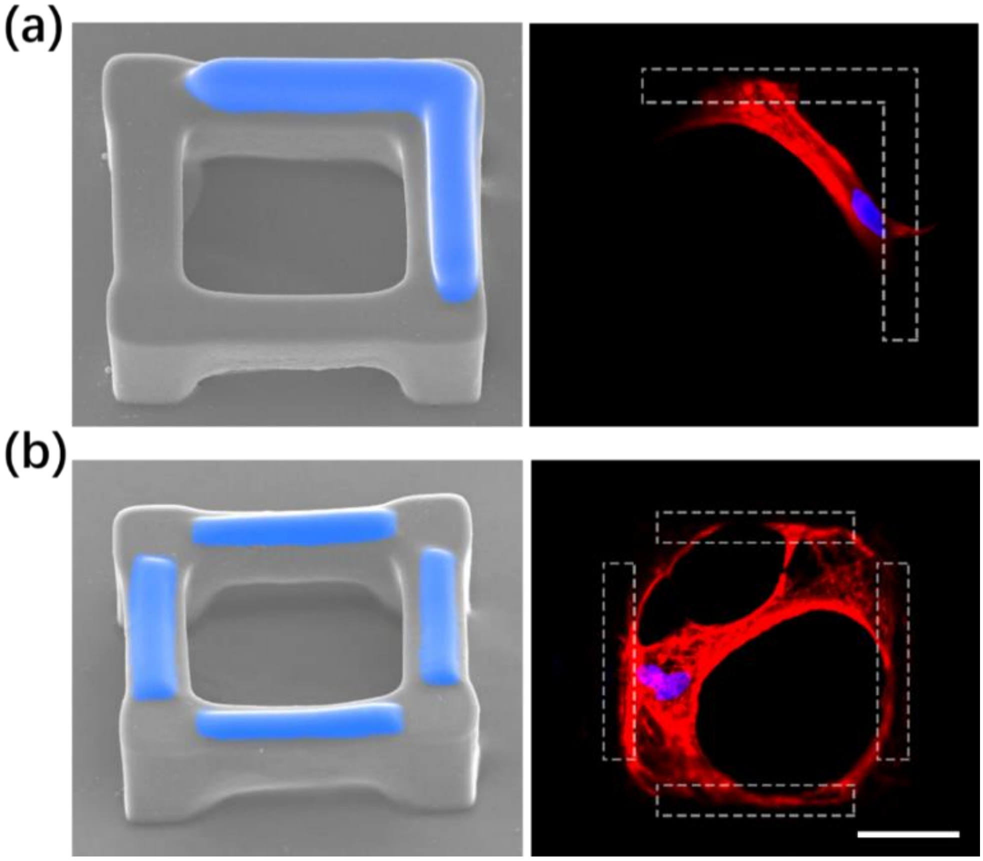

Figure 5.8 SEM images of the cubic microscaffolds with *in-situ* printed GelMA (highlighted in blue) and the fluorescent staining of f-actin (red) and nuclei (blue) of the hMSCs cultured in the corresponding microscaffolds (gelation shown as the dashed area). Scale bar = 50 μm.

The conventional universal polydopamine coating is short of capability of spatial control of cell spreading, and cell spread randomly on the microscaffolds. However, the in-situ printing technology enables to control the specific cell attachment on 3D environment precisely and consequent cell spreading behaviors. The microscaffolds (without polydopamine coating) with in-situ printed GelMA patterns were then used to seed hMSCs. On those microstructures, cells barely attached to the uncoating SU-8 surface. On contrary, the cell demonstrated the preference on adhesion to and spread along the printed GelMA pattern.

As shown in **Figure 5.8**, the cell can distinguish the bioactive pattern and bioinert microscaffold, and spread along the bioactive patterns upon 3D microstructures. In **Figure 5.8 (a)**, the cell spread across the corner of the fabricated cubic microscaffold in which the two neighboring suspended microbeams of the microscaffolds were printed an L-shape GelMA pattern. Confirmed by the confocal scanning of fluorescent cell staining, cell adhered to the overhanging microbeams on which were coated with GelMA at ends of the cell. Stretched by the GelMA patterns, cell suspended the central part over the internal opening of the cubic microscaffold. In **Figure 5.8 (b)**, all four suspended beams of the fabricated microscaffold were printed with GelMA stripe. Cell was controlled to adhere to all four suspended beams with GelMA strip and spread over the entire opening of the cubic microscaffold. The actin cytoskeleton was fluorescently stained and monitored by laser scanning confocal microscopy to show the morphology of cell spreading on microscaffold. In **Figure 5.8 (b)**, brighter fluorescent light of f-actin indicates that the cell on microscaffold with square-shape bioactive pattern has higher spreading level. Notably, the optical printed 3D cubic microscaffolds with presented bio-actively geometric cues can mimic the natural structure of bone lacunae, which thus provides a very promising platform to investigate hMSCs behaviors for bone research.

5.4.3 Discussion

hMSCs were seeded onto the polydopamine coated microscaffolds at the density of 20 000 cells/cm^2, which were continuously monitored for 24 h. After seeding, some cells were trapped by the SU-8 microscaffolds at first. After approximately 0.5 h, the cells gradually adhere to the beams of the 3D cubic microscaffolds. Although, for enhancement of cell adhesion, the entire environment was coated with polydopamine, it is interesting to note that the cells showed the preference on adhesion to the suspended microbeams instead of the pillars of the 3D microscaffold. The cells spread and elongated along the suspended beams. It took around 3 h to reach an equilibrium of the cell morphology after cell seeding.

For control experiments group, a series of micropillars array, as shown in **Figure 5.4 (b), (d) and (f)**, with same spacing and height of corresponding 3D microscaffolds. In the micropillars array, cells spread randomly on the surface of underlying substrates, rather than spread on those pillars or in the space between the pillars, which indicates that the fabricated 3D microscaffolds with suspended beams are critical for cell adhesion and spreading on 3D microenvironment.

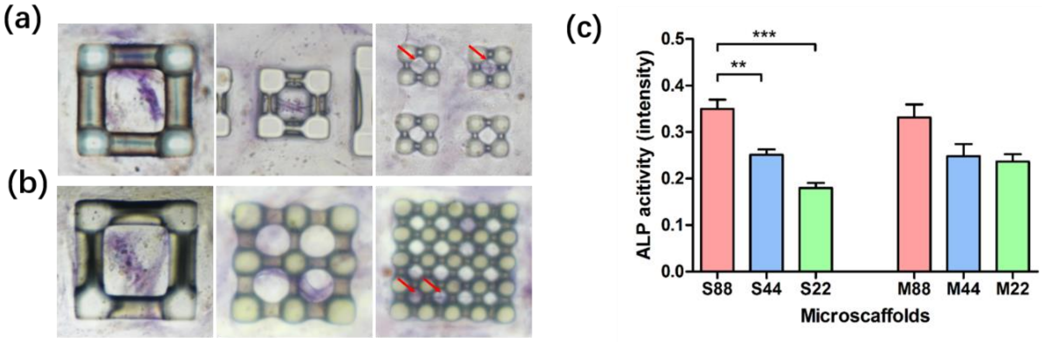

Figure 5.9 ALP staining of the hMSCs cultured in single-cubicle 3D microscaffolds (a) and multi-cubic 3D microscaffolds (b) after osteogenic induction for 7 d, scale bar = 50 μm. (c) Average ALP activity of the hMSCs; $**p < 0.01$, $***p < 0.001$.

It is found that the hMSCs in 3D microscaffolds with larger opening size show larger tendency of differentiation to osteogenesis (**Figure 5.9**), which can be deduced from the staining against alkaline phosphatase (ALP) which is a key marker of osteogenesis and biomineralization.

5.5 Summary

By using the novel 3D bio-fabrication platform, we demonstrated that SU-8 microscaffolds array with in-situ printed gelatin layer were fabricated for controlled cell culture. Due to the versatility and high efficiency of DOPsL, many large-area complex 3D architectures can be fabricated with photosensitive material in relatively short time. For investigation of interaction between cell morphology and 3D environment, two groups of microscaffolds with various dimension and combination were fabricated and then immersed into solution of polydopamine for non-specific surface modification. Further, with imaging system and nanopositioner of DOPsL, we in-situ printed GelMA on top of fabricated suspended scaffolds, which guided cell to spread in certain shape according to patterns of the gelatin. Although this work is just the first step in understanding stem cell behaviors in 3D environment, we believe that the strategy presented here opens a new route towards this goal.

Chapter 6

Conclusions and Future Outlook

6.1 Conclusions

In this thesis, two kinds of micro-optics devices, including top-lensed microlens array and WGM microcavity laser sensors, and a new kind of cellular-scale 3D microscaffolds have been developed for bio-microsystems. Thanks to our custom-built DLP-based optical μ-printing technology, which has the advantages including flexibility in pattern design, fabrication of 3D microstructures, and relatively low cost, we developed a new pathway in fabrication of micro-optics devices and 3D microstructures.

Firstly, the top-lensed microlens arrays were fabricated by custom-built DLP-based optical μ-printing technology. We investigated the relation between the UV exposure dose and cured depth of the photopolymer, which can be used to correct the bitmap of exposure scheme of the designed microlens. It was experimentally demonstrated that various microlens arrays with engineered focal structures were fabricated. To achieve the elongated focal depth, the top-lensed microlenses with hyperbolical upper lenses and oblate ellipsoidal bottom lenses were fabricated. By further increasing the difference of the curvature between the upper lenses and bottom lenses, the focal structure containing two distinct foci has been demonstrated. Due to the great capabilities in advanced light beam shaping or focusing, the TLMLs have significant potentials in micro-optical applications, such as optical storage, and in bio-microsystems, such as on-chip real-time cell counting.

Secondly, polymer optical WGM microlaser sensors were fabricated by using custom-built optical μ-printing technology and integrated into an optofluidic chip for sensing of biomarkers. The WGM microcavities of suspended microdisk were fabricated according to corrected bitmaps. The highest Q factor can reach around 10^4. The fabricated optical WGM microcavites were then deposited with a gain layer so as to support low-threshold lasing operation in visible wavelength. The microlasers were integrated into an optofluidic chip which can provide a platform for ELISA detection of VEGF. The microlaser can reduce the detection limit of VEGF to 17.8 fg/mL.

Lastly, the custom-built optical *in-situ* μ-printing technology was used to *in-situ* print bioactive patterns on the fabricated 3D microscaffolds with suspended beams. The single-cubical 3D microscaffolds with various opening areas were fabricated, which were used for investigation on cell spreading and differentiation. The results review that the 3D microscaffolds with larger opening area can enable smaller cell spreading factor and thus guide cell in osteogenic differentiation. Then the 3D microscaffolds with different combinations were also fabricated, which shows that the cell have same tendency in spreading and differentiation with the single-cubical microscaffolds. The bioactive material (i.e. GelMA) can be selectively patterned on the fabricated bioinert 3D microscaffolds, on which the cell spreading was guided by the bioactive pattern. Such 3D cubical microscafolds with precisely presented bioactive cues mimic the natural structure of bone lacunae, which thus provides a very promising platform to investigate hMSC behaviors for bone research.

6.2 Future outlook

In this thesis, two kinds of the micro-optics devices with miniaturized dimension and 3D microscaffolds with in-situ printed patterns have been successfully fabricated. Several outlooks for future research are as below:

1) With the advantages in miniaturization and engineered focal structure, the microlens arrays has great potential in integration of bio-systems. By further tailoring the profile of lens-on-lens structures, the lenses with two or more distinct foci can be achieved, which can be integrated into the microfluidic chip with multi-layer channels for ultra-compact high throughput flow cytometry. Also, the microlens with short focal depth can be fabricated by stimulus responsive materials, which can be integrated into the microfluidic chip for cost-effective intensity-modulation based sensors by tracing the shift of

the focus.

2) The WGM microcavities laser sensor can be improved by enhanced quality factors, advanced gain material, and coupled microdisks. As the Q factor of the fabricated optical microcavities is highly related to the dimension of the microdisks, which should be corresponding to the scattering loss on the surface. To improve the Q factor, the material which is easy to be reflowed thermally can be coated on the surface, such as PMMA. The advanced gain material, such as perovskite and aggregation-induced-emission materials, can be used in WGM microcavity laser with the higher photostability and sensing capability. For further improved sensitivity of biomolecules, the coupled microdisks with a doped and a undoped microcavities can be used for suppressing lasing mode, which can be used for ultrahigh sensitive biosensing application. Furthermore, WGMLs can be functionalized by using multiple antibodies through microfluidics. Therefore, the optofluidic chip can be used to simultaneously detect multiple biomolecules, such as interleukin-6, tumor necrosis factor and interferon, from one liquid sample.
3) The microscaffolds can be further improved in complex microstructures and novel biomaterials. Various geometries have different effect on cell behavior, as the cell shape factor will be different on such geometries. Moreover, through layer-by-layer

exposure, the complex 3D matrix can be created, which can mimic the bone structures and be used in *in-vivo* studies for tissue engineering and transplant organ. The novel biomaterial on microstructures can assist guided cell behavior, such as poly(L-lactic acid), poly(ε-caprolactone) and polyphosphoesters. The fabricated 3D microscaffolds arrays can also be integrated into a biochip for investigation of organ-on-chip.

References

1. W. Fritzsche and J. Popp, *Optical nano-and microsystems for bioanalytics* (Springer Science & Business Media, 2012), Vol. 10.
2. J. Godin, C. H. Chen, S. H. Cho, W. Qiao, F. Tsai, and Y. H. Lo, "Microfluidics and photonics for Bio-System-on-a-Chip: a review of advancements in technology towards a microfluidic flow cytometry chip," J Biophotonics **1**, 355-376 (2008).
3. S. Camou, A. Tixier-Mita, H. Fujita, and T. Fujii, "Integration of Microoptics in Bio-Micro-Electro-Mechanical Systems towards Micro-Total-Analysis Systems," Japanese Journal of Applied Physics **43**, 5697-5705 (2004).
4. Y. M. Song, Y. Xie, V. Malyarchuk, J. Xiao, I. Jung, K. J. Choi, Z. Liu, H. Park, C. Lu, R. H. Kim, R. Li, K. B. Crozier, Y. Huang, and J. A. Rogers, "Digital cameras with designs inspired by the arthropod eye," Nature **497**, 95-99 (2013).
5. S. Nizamoglu, M. C. Gather, M. Humar, M. Choi, S. Kim, K. S. Kim, S. K. Hahn, G. Scarcelli, M. Randolph, R. W. Redmond, and S. H. Yun, "Bioabsorbable polymer optical waveguides for deep-tissue photomedicine," Nat Commun **7**, 10374 (2016).
6. W. Chen, Ş. Kaya Özdemir, G. Zhao, J. Wiersig, and L. Yang, "Exceptional points enhance sensing in an optical microcavity," Nature **548**, 192-196 (2017).
7. K. Y. Yang, D. Y. Oh, S. H. Lee, Q.-F. Yang, X. Yi, B. Shen, H. Wang, and K. Vahala, "Bridging ultrahigh-Q devices and photonic circuits," Nature Photonics **12**, 297-302 (2018).
8. Y. C. Tung, N. T. Huang, B. R. Oh, B. Patra, C. C. Pan, T. Qiu, P. K. Chu, W. Zhang, and K. Kurabayashi, "Optofluidic detection for cellular phenotyping," Lab Chip **12**, 3552-3565 (2012).
9. C. Lv, H. Xia, W. Guan, Y. L. Sun, Z. N. Tian, T. Jiang, Y. S. Wang, Y. L. Zhang, Q. D. Chen, K. Ariga, Y. D. Yu, and H. B. Sun, "Integrated optofluidic-microfluidic twin channels: toward diverse application of lab-on-a-chip systems," Scientific Reports **6**, 9 (2016).
10. D. C. Cole, E. S. Lamb, P. Del'Haye, S. A. Diddams, and S. B. Papp, "Soliton crystals in Kerr resonators," Nature Photonics **11**, 671-676 (2017).
11. E. Lafalce, Q. Zeng, C. H. Lin, M. J. Smith, S. T. Malak, J. Jung, Y. J. Yoon, Z. Lin, V. V. Tsukruk, and Z. V. Vardeny, "Robust lasing modes in coupled colloidal quantum dot microdisk pairs using a non-Hermitian exceptional point," Nat Commun **10**, 561 (2019).
12. Y. Ye, Z. J. Wong, X. Lu, X. Ni, H. Zhu, X. Chen, Y. Wang, and X. Zhang, "Monolayer excitonic laser," Nature Photonics **9**, 733-737 (2015).
13. S. V. Murphy and A. Atala, "3D bioprinting of tissues and organs," Nat Biotechnol **32**, 773-785 (2014).
14. H. W. Kang, S. J. Lee, I. K. Ko, C. Kengla, J. J. Yoo, and A. Atala, "A 3D bioprinting system to produce human-scale tissue constructs with structural integrity," Nat Biotechnol **34**, 312-319 (2016).
15. V. Esteve, J. Berganzo, R. Monge, M. C. Martinez-Bisbal, R. Villa, B. Celda, and L. Fernandez, "Development of a three-dimensional cell culture system based on microfluidics for nuclear magnetic resonance and optical monitoring," Biomicrofluidics **8**, 064105 (2014).
16. H. Hwang and J. K. Park, "Optoelectrofluidic platforms for chemistry and biology," Lab Chip **11**, 33-47 (2011).
17. D. Zhang, Q. Xu, C. Fang, K. Wang, X. Wang, S. Zhuang, and B. Dai, "Fabrication of a Microlens

Array with Controlled Curvature by Thermally Curving Photosensitive Gel Film beneath Microholes," ACS Appl Mater Interfaces **9**, 16604-16609 (2017).

18. Q. Chen, M. Ritt, S. Sivaramakrishnan, Y. Sun, and X. Fan, "Optofluidic lasers with a single molecular layer of gain," Lab Chip **14**, 4590-4595 (2014).
19. R. Li, F. Jia, W. Zhang, F. Shi, Z. Fang, H. Zhao, Z. Hu, and Z. Wei, "Device for whole genome sequencing single circulating tumor cells from whole blood," Lab Chip **19**, 3168-3178 (2019).
20. B. Zhang, M. Montgomery, M. D. Chamberlain, S. Ogawa, A. Korolj, A. Pahnke, L. A. Wells, S. Masse, J. Kim, L. Reis, A. Momen, S. S. Nunes, A. R. Wheeler, K. Nanthakumar, G. Keller, M. V. Sefton, and M. Radisic, "Biodegradable scaffold with built-in vasculature for organ-on-a-chip engineering and direct surgical anastomosis," Nat Mater **15**, 669-678 (2016).
21. H. Zappe, "Micro-optics: a micro-tutorial," Advanced Optical Technologies **1**(2012).
22. L. Miccio, P. Memmolo, F. Merola, P. A. Netti, and P. Ferraro, "Red blood cell as an adaptive optofluidic microlens," Nat Commun **6**, 6502 (2015).
23. D. Wu, J. Xu, L.-G. Niu, S.-Z. Wu, K. Midorikawa, and K. Sugioka, "In-channel integration of designable microoptical devices using flat scaffold-supported femtosecond-laser microfabrication for coupling-free optofluidic cell counting," Light: Science & Applications **4**, e228 (2015).
24. E. Chen, R. Wu, and T. Guo, "Design a freeform microlens array module for any arbitrary-shape collimated beam shaping and color mixing," Optics Communications **321**, 78-85 (2014).
25. R. Wu, Z. Zheng, H. Li, and X. Liu, "Freeform lens for off-axis illumination in optical lithography system," Optics Communications **284**, 2662-2667 (2011).
26. Y. Zhang, R. Wu, P. Liu, Z. Zheng, H. Li, and X. Liu, "Double freeform surfaces design for laser beam shaping with Monge–Ampère equation method," Optics Communications **331**, 297-305 (2014).
27. Y. Zou, W. Zhang, F. S. Chau, and G. Zhou, "Solid electrically tunable dual-focus lens using freeform surfaces and microelectro-mechanical-systems actuator," Opt Lett **41**, 1-4 (2016).
28. Q. Yang, S. Tong, F. Chen, Z. Deng, H. Bian, G. Du, J. Yong, and X. Hou, "Lens-on-lens microstructures," Optics Letters **40**, 5359-5362 (2015).
29. E. Kim, M. D. Baaske, and F. Vollmer, "Towards next-generation label-free biosensors: recent advances in whispering gallery mode sensors," Lab Chip (2017).
30. L. He, Ş. K. Özdemir, and L. Yang, "Whispering gallery microcavity lasers," Laser & Photonics Reviews **7**, 60-82 (2013).
31. L. He, S. K. Ozdemir, J. Zhu, W. Kim, and L. Yang, "Detecting single viruses and nanoparticles using whispering gallery microlasers," Nat Nanotechnol **6**, 428-432 (2011).
32. L. He, Ş. K. Özdemir, J. Zhu, and L. Yang, "Ultrasensitive detection of mode splitting in active optical microcavities," Physical Review A **82**(2010).
33. T. Siegle, J. Kellerer, M. Bonenberger, S. Krammer, C. Klusmann, M. Muller, and H. Kalt, "Comparison of various excitation and detection schemes for dye-doped polymeric whispering gallery mode micro-lasers," Opt Express **26**, 3579-3593 (2018).
34. E. Cukierman, R. Pankov, D. R. Stevens, and K. M. Yamada, "Taking Cell-Matrix Adhesions to the Third Dimension," Science **294**, 1708-1712 (2001).
35. S. Oh, K. S. Brammer, Y. S. J. Li, D. Teng, A. J. Engler, S. Chien, and S. Jin, "Stem cell fate dictated solely by altered nanotube dimension," **106**, 2130-2135 (2009).
36. M. J. Dalby, N. Gadegaard, R. Tare, A. Andar, M. O. Riehle, P. Herzyk, C. D. Wilkinson, and R. O. Oreffo, "The control of human mesenchymal cell differentiation using nanoscale symmetry and disorder," Nat Mater **6**, 997-1003 (2007).

37. R. J. McMurray, N. Gadegaard, P. M. Tsimbouri, K. V. Burgess, L. E. McNamara, R. Tare, K. Murawski, E. Kingham, R. O. Oreffo, and M. J. Dalby, "Nanoscale surfaces for the long-term maintenance of mesenchymal stem cell phenotype and multipotency," Nat Mater **10**, 637-644 (2011).
38. A. Higuchi, Q. D. Ling, S. T. Hsu, and A. Umezawa, "Biomimetic cell culture proteins as extracellular matrices for stem cell differentiation," Chem Rev **112**, 4507-4540 (2012).
39. K. A. Kilian, B. Bugarija, B. T. Lahn, and M. Mrksich, "Geometric cues for directing the differentiation of mesenchymal stem cells," Proc Natl Acad Sci U S A **107**, 4872-4877 (2010).
40. R. Peng, X. Yao, and J. Ding, "Effect of cell anisotropy on differentiation of stem cells on micropatterned surfaces through the controlled single cell adhesion," Biomaterials **32**, 8048-8057 (2011).
41. R. Peng, X. Yao, B. Cao, J. Tang, and J. Ding, "The effect of culture conditions on the adipogenic and osteogenic inductions of mesenchymal stem cells on micropatterned surfaces," Biomaterials **33**, 6008-6019 (2012).
42. H. Cui, M. Nowicki, J. P. Fisher, and L. G. Zhang, "3D Bioprinting for Organ Regeneration," Adv Healthc Mater **6**(2017).
43. A. Marino, C. Filippeschi, G. G. Genchi, V. Mattoli, B. Mazzolai, and G. Ciofani, "The Osteoprint: a bioinspired two-photon polymerized 3-D structure for the enhancement of bone-like cell differentiation," Acta Biomater **10**, 4304-4313 (2014).
44. M. Marelli, N. Gadhari, G. Boero, M. Chiquet, and J. Brugger, "Cell force measurements in 3D microfabricated environments based on compliant cantilevers," Lab Chip **14**, 286-293 (2014).
45. J. K. Hohmann, M. Renner, E. H. Waller, and G. von Freymann, "Three-Dimensional μ-Printing: An Enabling Technology," Advanced Optical Materials **3**, 1488-1507 (2015).
46. R. Palankar, M. Glaubitz, U. Martens, N. Medvedev, M. von der Ehe, S. B. Felix, M. Munzenberg, and M. Delcea, "3D Micropillars Guide the Mechanobiology of Human Induced Pluripotent Stem Cell-Derived Cardiomyocytes," Adv Healthc Mater **5**, 335-341 (2016).
47. N. Zhang, Z. Gu, S. Liu, Y. Wang, S. Wang, Z. Duan, W. Sun, Y.-F. Xiao, S. Xiao, and Q. Song, "Far-field single nanoparticle detection and sizing," Optica **4**, 1151 (2017).
48. M. S. Hahn, J. S. Miller, and J. L. West, "Three-Dimensional Biochemical and Biomechanical Patterning of Hydrogels for Guiding Cell Behavior," Advanced Materials **18**, 2679-2684 (2006).
49. P. Soman, J. A. Kelber, J. W. Lee, T. N. Wright, K. S. Vecchio, R. L. Klemke, and S. Chen, "Cancer cell migration within 3D layer-by-layer microfabricated photocrosslinked PEG scaffolds with tunable stiffness," Biomaterials **33**, 7064-7070 (2012).
50. A. P. Zhang, X. Qu, P. Soman, K. C. Hribar, J. W. Lee, S. Chen, and S. He, "Rapid fabrication of complex 3D extracellular microenvironments by dynamic optical projection stereolithography," Advanced materials **24**, 4266-4270 (2012).
51. H. P. Herzig, *Micro-optics: elements, systems and applications* (CRC Press, 2014).
52. N. Lindlein and H. P. Herzig, *Design and modeling of a miniature system containing micro-optics*, International Symposium on Optical Science and Technology (SPIE, 2001), Vol. 4437.
53. J. Ye, L. Chen, X. Li, Q. Yuan, and Z. Gao, *Review of optical freeform surface representation technique and its application* (SPIE, 2017), Vol. 56, pp. 1-15, 15.
54. W. Yuan, L.-H. Li, W.-B. Lee, and C.-Y. Chan, "Fabrication of Microlens Array and Its Application: A Review," Chinese Journal of Mechanical Engineering **31**(2018).
55. A. K. Yetisen, H. Butt, T. Mikulchyk, R. Ahmed, Y. Montelongo, M. Humar, N. Jiang, S. Martin, I. Naydenova, and S. H. Yun, "Color-Selective 2.5D Holograms on Large-Area Flexible Substrates for

Sensing and Multilevel Security," Advanced Optical Materials **4**, 1589-1600 (2016).

56. Y.-L. Sun, W.-F. Dong, L.-G. Niu, T. Jiang, D.-X. Liu, L. Zhang, Y.-S. Wang, Q.-D. Chen, D.-P. Kim, and H.-B. Sun, "Protein-based soft micro-optics fabricated by femtosecond laser direct writing," Light: Science & Applications **3**, e129-e129 (2014).
57. J. Kim, J. Kim, J.-H. Na, B. Lee, and S.-D. Lee, "Liquid crystal-based square lens array with tunable focal length," Optics Express **22**, 3316-3324 (2014).
58. L. Liang, X. Q. Zhu, H. L. Liu, Y. Shi, and Y. Yang, "A switchable 3D liquid-liquid biconvex lens with enhanced resolution using Dean flow," Lab Chip **17**, 3258-3263 (2017).
59. R. Ahmed, A. K. Yetisen, and H. Butt, "High Numerical Aperture Hexagonal Stacked Ring-Based Bidirectional Flexible Polymer Microlens Array," ACS Nano **11**, 3155-3165 (2017).
60. M. M. Vekshin, A. S. Levchenko, A. V. Nikitin, V. A. Nikitin, and N. A. Yacovenko, "Glass microlens arrays for Shack–Hartmann wavefront sensors," Measurement Science and Technology **21**, 054010 (2010).
61. G. T. Paloczi, "Polymer integrated optics Device architectures and fabrication methods," 2005).
62. R. Kingslake and R. Barry Johnson, "Chapter 4 - Aberration Theory," in *Lens Design Fundamentals (Second Edition)*, R. Kingslake and R. Barry Johnson, eds. (Academic Press, Boston, 2010), pp. 101-135.
63. T. Hou, C. Zheng, S. Bai, Q. Ma, D. Bridges, A. Hu, and W. W. Duley, "Fabrication, characterization, and applications of microlenses," Appl Opt **54**, 7366-7376 (2015).
64. C. T. Pan and C. Y. Su, "Study of micro-lens array by reflow process," Journal of Modern Optics **55**, 2843-2856 (2008).
65. J. M. Geary, *Introduction to lens design: with practical ZEMAX examples* (Willmann-Bell Richmond, VA, USA:, 2002).
66. M. J. I. Laikin, New York, "Lens Design, Mercel Dekker," (1995).
67. V. N. Mahajan, *Aberration theory made simple* (SPIE Optical Engineering Press, Bellingham, Wash., USA, 1991).
68. V. N. Mahajan, *Optical imaging and aberrations* (SPIE Optical Engineering Press, Bellingham, Wa., 1998).
69. P. Schnauber, A. Thoma, C. Heine, A. Schlehahn, L. Gantz, M. Gschrey, R. Schmidt, C. Hopfmann, B. Wohlfeil, J.-H. Schulze, A. Strittmatter, T. Heindel, S. Rodt, U. Woggon, D. Gershoni, and S. Reitzenstein, "Bright Single-Photon Sources Based on Anti-Reflection Coated Deterministic Quantum Dot Microlenses," Technologies **4**(2015).
70. M.-L. Wu, Y.-C. Lee, S.-P. Yang, P.-S. Lee, and J.-Y. Chang, "Azimuthally isotropic irradiance of GaN-based light-emitting diodes with GaN microlens arrays," Optics Express **17**, 6148-6155 (2009).
71. F. Galeotti, W. Mróz, G. Scavia, and C. Botta, "Microlens arrays for light extraction enhancement in organic light-emitting diodes: A facile approach," Organic Electronics **14**, 212-218 (2013).
72. Y. Peng, X. Guo, R. Liang, Y. Mou, H. Cheng, M. Chen, and S. Liu, "Fabrication of Microlens Arrays with Controlled Curvature by Micromolding Water Condensing Based Porous Films for Deep Ultraviolet LEDs," ACS Photonics **4**, 2479-2485 (2017).
73. S. Fischbach, A. Schlehahn, A. Thoma, N. Srocka, T. Gissibl, S. Ristok, S. Thiele, A. Kaganskiy, A. Strittmatter, T. Heindel, S. Rodt, A. Herkommer, H. Giessen, and S. Reitzenstein, "Single Quantum Dot with Microlens and 3D-Printed Micro-objective as Integrated Bright Single-Photon Source," ACS Photonics **4**, 1327-1332 (2017).
74. M. Sartison, S. L. Portalupi, T. Gissibl, M. Jetter, H. Giessen, and P. Michler, "Combining in-situ

lithography with 3D printed solid immersion lenses for single quantum dot spectroscopy," Sci Rep **7**, 39916 (2017).

75. Y. Hu, S. Rao, S. Wu, P. Wei, W. Qiu, D. Wu, B. Xu, J. Ni, L. Yang, J. Li, J. Chu, and K. Sugioka, "All-Glass 3D Optofluidic Microchip with Built-in Tunable Microlens Fabricated by Femtosecond Laser-Assisted Etching," Advanced Optical Materials **6**(2018).
76. H. Yang, M. Cornaglia, and M. A. Gijs, "Photonic nanojet array for fast detection of single nanoparticles in a flow," Nano Lett **15**, 1730-1735 (2015).
77. H. Yang and M. A. Gijs, "Microtextured substrates and microparticles used as in situ lenses for on-chip immunofluorescence amplification," Anal Chem **85**, 2064-2071 (2013).
78. J. J. Schwartz, S. Stavrakis, and S. R. Quake, "Colloidal lenses allow high-temperature single-molecule imaging and improve fluorophore photostability," Nat Nanotechnol **5**, 127-132 (2010).
79. A. Schaap, T. Rohrlack, and Y. Bellouard, "Optical classification of algae species with a glass lab-on-a-chip," Lab Chip **12**, 1527-1532 (2012).
80. D. Wu, L. G. Niu, S. Z. Wu, J. Xu, K. Midorikawa, and K. Sugioka, "Ship-in-a-bottle femtosecond laser integration of optofluidic microlens arrays with center-pass units enabling coupling-free parallel cell counting with a 100% success rate," Lab Chip **15**, 1515-1523 (2015).
81. G. Holzner, Y. Du, X. Cao, J. Choo, J. d. A, and S. Stavrakis, "An optofluidic system with integrated microlens arrays for parallel imaging flow cytometry," Lab Chip **18**, 3631-3637 (2018).
82. L. J. T. L. Rayleigh, Edinburgh,, D. P. Magazine, and J. o. Science, "CXII. The problem of the whispering gallery," **20**, 1001-1004 (1910).
83. A. Chiasera, Y. Dumeige, P. Féron, M. Ferrari, Y. Jestin, G. Nunzi Conti, S. Pelli, S. Soria, and G. C. Righini, "Spherical whispering-gallery-mode microresonators," Laser & Photonics Reviews **4**, 457-482 (2010).
84. S. Yang, Y. Wang, and H. Sun, "Advances and Prospects for Whispering Gallery Mode Microcavities," Advanced Optical Materials **3**, 1136-1162 (2015).
85. D. J. Griffiths, *Introduction to electrodynamics,* 4th ed.. ed. (Pearson, Boston, 2013).
86. G. C. Righini, Y. Dumeige, P. Feron, M. Ferrari, G. N. Conti, D. Ristic, and S. Soria, "Whispering gallery mode microresonators: Fundamentals and applications," Rivista Del Nuovo Cimento **34**, 435-488 (2011).
87. A. N. Oraevsky, "Whispering-gallery waves," Quantum Electronics **32**, 377-400 (2002).
88. I. Breunig, B. Sturman, F. Sedlmeir, H. G. Schwefel, and K. Buse, "Whispering gallery modes at the rim of an axisymmetric optical resonator: analytical versus numerical description and comparison with experiment," Opt Express **21**, 30683-30692 (2013).
89. M. L. Gorodetsky and Y. A. Demchenko, *Accurate analytical estimates of eigenfrequencies and dispersion in whispering-gallery spheroidal resonators*, SPIE LASE (SPIE, 2012), Vol. 8236.
90. G. Schunk, J. U. Furst, M. Fortsch, D. V. Strekalov, U. Vogl, F. Sedlmeir, H. G. Schwefel, G. Leuchs, and C. Marquardt, "Identifying modes of large whispering-gallery mode resonators from the spectrum and emission pattern," Opt Express **22**, 30795-30806 (2014).
91. T. J. Kippenberg, S. M. Spillane, and K. J. Vahala, "Demonstration of ultra-high-Q small mode volume toroid microcavities on a chip," Applied Physics Letters **85**, 6113-6115 (2004).
92. D. W. Vernooy and H. J. Kimble, "Quantum structure and dynamics for atom galleries," Physical Review A **55**, 1239-1261 (1997).
93. S. M. Spillane, T. J. Kippenberg, K. J. Vahala, K. W. Goh, E. Wilcut, and H. J. Kimble, "Ultrahigh-Qtoroidal microresonators for cavity quantum electrodynamics," Physical Review A **71**(2005).

94. M. L. Gorodetsky, A. A. Savchenkov, and V. S. Ilchenko, "Ultimate Q of optical microsphere resonators," Optics Letters **21**, 453-455 (1996).
95. A. E. Shitikov, I. A. Bilenko, N. M. Kondratiev, V. E. Lobanov, A. Markosyan, and M. L. Gorodetsky, "Billion Q-factor in silicon WGM resonators," Optica **5**(2018).
96. A. A. Savchenkov, A. B. Matsko, M. Mohageg, and L. Maleki, "Ringdown spectroscopy of stimulated Raman scattering in a whispering gallery mode resonator," Optics Letters **32**, 497-499 (2007).
97. Y. Dumeige, S. Trebaol, L. Ghişa, T. K. N. Nguyên, H. Tavernier, and P. Féron, "Determination of coupling regime of high-Q resonators and optical gain of highly selective amplifiers," Journal of the Optical Society of America B **25**, 2073-2080 (2008).
98. K. Srinivasan, M. Borselli, O. Painter, A. Stintz, and S. Krishna, "Cavity Q, mode volume, and lasing threshold in small diameter AlGaAs microdisks with embedded quantum dots," Optics Express **14**, 1094-1105 (2006).
99. S. Zhu, B. Xiao, B. Jiang, L. Shi, and X. Zhang, "Tunable Brillouin and Raman microlasers using hybrid microbottle resonators," Nanophotonics **0**(2019).
100. J. Zhu, S. K. Ozdemir, Y.-F. Xiao, L. Li, L. He, D.-R. Chen, and L. Yang, "On-chip single nanoparticle detection and sizing by mode splitting in an ultrahigh-Q microresonator," Nature Photonics **4**, 46-49 (2009).
101. A. L. Martin, D. K. Armani, L. Yang, and K. J. Vahala, "Replica-molded high-Q polymer microresonators," Optics Letters **29**, 533-535 (2004).
102. J. R. Schwesyg, T. Beckmann, A. S. Zimmermann, K. Buse, and D. Haertle, "Fabrication and characterization of whispering-gallery-mode resonators made of polymers," Optics Express **17**, 2573-2578 (2009).
103. Y. L. Sun, Z. S. Hou, S. M. Sun, B. Y. Zheng, J. F. Ku, W. F. Dong, Q. D. Chen, and H. B. Sun, "Protein-Based Three-Dimensional Whispering-Gallery-Mode Micro-Lasers with Stimulus-Responsiveness," Sci Rep **5**, 12852 (2015).
104. S. Avino, A. Krause, R. Zullo, A. Giorgini, P. Malara, P. De Natale, H. P. Loock, and G. Gagliardi, "Direct Sensing in Liquids Using Whispering-Gallery-Mode Droplet Resonators," Advanced Optical Materials **2**, 1155-1159 (2014).
105. J. Wu, X. Guo, A. P. Zhang, and H. Y. Tam, "Rapid 3D u-printing of polymer optical whispering-gallery mode resonators," Opt Express **23**, 29708-29714 (2015).
106. M. Kuwata-Gonokami and K. Takeda, "Polymer whispering gallery mode lasers," Optical Materials **9**, 12-17 (1998).
107. P. T. Snee, Y. Chan, D. G. Nocera, and M. G. Bawendi, "Whispering-Gallery-Mode Lasing from a Semiconductor Nanocrystal/Microsphere Resonator Composite," Advanced Materials **17**, 1131-1136 (2005).
108. Z. Zhang, Z. Wang, Z. Xu, Q. Gao, P. Liu, J. Ren, M. Li, C. Zhou, Q. Liao, and H. Fu, "Soft Lithography to Fabricate 3D Patterning Organic Microrings towards High-Performance Near-Infrared Laser Arrays," Advanced Optical Materials **6**(2018).
109. I. B. Dogru, R. Melikov, and S. Nizamoglu, "Biomaterial Disk Lasers by Suppressing the Coffee Ring Effect," ACS Biomaterials Science & Engineering **4**, 4385-4390 (2018).
110. S. F. Wondimu, S. von der Ecken, R. Ahrens, W. Freude, A. E. Guber, and C. Koos, "Integration of digital microfluidics with whispering-gallery mode sensors for label-free detection of biomolecules," Lab Chip **17**, 1740-1748 (2017).
111. W. Stöber, A. Fink, and E. Bohn, "Controlled growth of monodisperse silica spheres in the micron

size range," Journal of Colloid and Interface Science **26**, 62-69 (1968).

112. T. Yoshie, L. Tang, and S. Y. Su, "Optical microcavity: sensing down to single molecules and atoms," Sensors (Basel) **11**, 1972-1991 (2011).
113. T. Reynolds, N. Riesen, A. Meldrum, X. Fan, J. M. M. Hall, T. M. Monro, and A. François, "Fluorescent and lasing whispering gallery mode microresonators for sensing applications," Laser & Photonics Reviews **11**, 1600265 (2017).
114. X. Zheng, J. Deotte, M. P. Alonso, G. R. Farquar, T. H. Weisgraber, S. Gemberling, H. Lee, N. Fang, and C. M. Spadaccini, "Design and optimization of a light-emitting diode projection micro-stereolithography three-dimensional manufacturing system," Rev Sci Instrum **83**, 125001 (2012).
115. L. Labrador-Paez, K. Soler-Carracedo, M. Hernandez-Rodriguez, I. R. Martin, T. Carmon, and L. L. Martin, "Liquid whispering-gallery-mode resonator as a humidity sensor," Opt Express **25**, 1165-1172 (2017).
116. M. Manzo and T. Ioppolo, "Untethered photonic sensor for wall pressure measurement," Opt Lett **40**, 2257-2260 (2015).
117. T. A. Kumar, M. A. Mohiddon, N. Dutta, N. K. Viswanathan, and S. Dhara, "Detection of phase transitions from the study of whispering gallery mode resonance in liquid crystal droplets," Applied Physics Letters **106**(2015).
118. C. Pérez-Rodríguez, L. Labrador-Páez, I. R. Martín, and S. Ríos, "Temperature response of the whispering gallery mode resonances from the green upconversion emission of an Er3+–Yb3+ co-doped microsphere," Laser Physics Letters **12**(2015).
119. X. Zhou, L. Zhang, and W. Pang, "Performance and noise analysis of optical microresonator-based biochemical sensors using intensity detection," Opt Express **24**, 18197-18208 (2016).
120. M. Himmelhaus and A. Francois, "In-vitro sensing of biomechanical forces in live cells by a whispering gallery mode biosensor," Biosens Bioelectron **25**, 418-427 (2009).
121. X. Fan and S. H. Yun, "The potential of optofluidic biolasers," Nat Methods **11**, 141-147 (2014).
122. W. Kim, Ş. K. Özdemir, J. Zhu, L. He, and L. Yang, "Demonstration of mode splitting in an optical microcavity in aqueous environment," Applied Physics Letters **97**, 071111 (2010).
123. X. Jiang, A. J. Qavi, S. H. Huang, and L. J. a. p. a. Yang, "Whispering gallery microsensors: a review," (2018).
124. B. B. Li, W. R. Clements, X. C. Yu, K. Shi, Q. Gong, and Y. F. Xiao, "Single nanoparticle detection using split-mode microcavity Raman lasers," Proc Natl Acad Sci U S A **111**, 14657-14662 (2014).
125. C. Gong, Y. Gong, X. Zhao, Y. Luo, Q. Chen, X. Tan, Y. Wu, X. Fan, G. D. Peng, and Y. J. Rao, "Distributed fibre optofluidic laser for chip-scale arrayed biochemical sensing," Lab Chip **18**, 2741-2748 (2018).
126. Y. C. Chen, Q. Chen, and X. Fan, "Lasing in blood," Optica **3**, 809-815 (2016).
127. E. S. Bos, A. A. van der Doelen, N. van Rooy, and A. H. Schuurs, "3,3',5,5' - Tetramethylbenzidine as an Ames test negative chromogen for horse-radish peroxidase in enzyme-immunoassay," J Immunoassay **2**, 187-204 (1981).
128. M. Hamon, J. W. J. M. Hong, and Cells, "New tools and new biology: Recent miniaturized systems for molecular and cellular biology," **36**, 485-506 (2013).
129. P. Shinde, L. Mohan, A. Kumar, K. Dey, A. Maddi, A. N. Patananan, F. G. Tseng, H. Y. Chang, M. Nagai, and T. S. Santra, "Current Trends of Microfluidic Single-Cell Technologies," Int J Mol Sci **19**(2018).
130. P. Neuzil, C. D. Campos, C. C. Wong, J. B. Soon, J. Reboud, and A. Manz, "From chip-in-a-lab to

lab-on-a-chip: towards a single handheld electronic system for multiple application-specific lab-on-a-chip (ASLOC)," Lab Chip **14**, 2168-2176 (2014).

131. G. Whitesides, "The lab finally comes to the chip!," Lab Chip **14**, 3125-3126 (2014).
132. X. Xing, C. N. Ng, M. L. Chau, and L. Yobas, "Railing cells along 3D microelectrode tracks for continuous-flow dielectrophoretic sorting," Lab Chip **18**, 3760-3769 (2018).
133. C. W. t. Shields, C. D. Reyes, and G. P. Lopez, "Microfluidic cell sorting: a review of the advances in the separation of cells from debulking to rare cell isolation," Lab Chip **15**, 1230-1249 (2015).
134. N. M. Karabacak, P. S. Spuhler, F. Fachin, E. J. Lim, V. Pai, E. Ozkumur, J. M. Martel, N. Kojic, K. Smith, P. I. Chen, J. Yang, H. Hwang, B. Morgan, J. Trautwein, T. A. Barber, S. L. Stott, S. Maheswaran, R. Kapur, D. A. Haber, and M. Toner, "Microfluidic, marker-free isolation of circulating tumor cells from blood samples," Nat Protoc **9**, 694-710 (2014).
135. S. M. McFaul, B. K. Lin, and H. Ma, "Cell separation based on size and deformability using microfluidic funnel ratchets," Lab Chip **12**, 2369-2376 (2012).
136. W. Sheng, O. O. Ogunwobi, T. Chen, J. Zhang, T. J. George, C. Liu, and Z. H. Fan, "Capture, release and culture of circulating tumor cells from pancreatic cancer patients using an enhanced mixing chip," Lab Chip **14**, 89-98 (2014).
137. S. J. Tan, R. L. Lakshmi, P. Chen, W. T. Lim, L. Yobas, and C. T. Lim, "Versatile label free biochip for the detection of circulating tumor cells from peripheral blood in cancer patients," Biosens Bioelectron **26**, 1701-1705 (2010).
138. M. E. Warkiani, B. L. Khoo, L. Wu, A. K. Tay, A. A. Bhagat, J. Han, and C. T. Lim, "Ultra-fast, label-free isolation of circulating tumor cells from blood using spiral microfluidics," Nat Protoc **11**, 134-148 (2016).
139. J. McGrath, M. Jimenez, and H. Bridle, "Deterministic lateral displacement for particle separation: a review," Lab Chip **14**, 4139-4158 (2014).
140. E. D. Lemma, B. Spagnolo, M. De Vittorio, and F. Pisanello, "Studying Cell Mechanobiology in 3D: The Two-Photon Lithography Approach," Trends Biotechnol **37**, 358-372 (2019).
141. K. C. Hribar, P. Soman, J. Warner, P. Chung, and S. Chen, "Light-assisted direct-write of 3D functional biomaterials," Lab Chip **14**, 268-275 (2014).
142. F. Klein, T. Striebel, J. Fischer, Z. Jiang, C. M. Franz, G. von Freymann, M. Wegener, and M. Bastmeyer, "Elastic fully three-dimensional microstructure scaffolds for cell force measurements," Adv Mater **22**, 868-871 (2010).
143. S. Gao, W.-T. Tung, D. S.-H. Wong, L. Bian, and A. P. Zhang, "Direct optical micropatterning of poly(dimethylsiloxane) for microfluidic devices," Journal of Micromechanics and Microengineering **28**, 095011 (2018).
144. X. Ouyang, K. Zhang, J. Wu, D. S. Wong, Q. Feng, L. Bian, and A. P. Zhang, "Optical micro-Printing of Cellular-Scale Microscaffold Arrays for 3D Cell Culture," Sci Rep **7**, 8880 (2017).
145. A. Marino, G. Ciofani, C. Filippeschi, M. Pellegrino, M. Pellegrini, P. Orsini, M. Pasqualetti, V. Mattoli, and B. Mazzolai, "Two-photon polymerization of sub-micrometric patterned surfaces: investigation of cell-substrate interactions and improved differentiation of neuron-like cells," ACS Appl Mater Interfaces **5**, 13012-13021 (2013).
146. M. H. Olsen, G. M. Hjorto, M. Hansen, O. Met, I. M. Svane, and N. B. Larsen, "In-chip fabrication of free-form 3D constructs for directed cell migration analysis," Lab Chip **13**, 4800-4809 (2013).
147. J. Maciulaitis, M. Deveikyte, S. Rekstyte, M. Bratchikov, A. Darinskas, A. Simbelyte, G. Daunoras, A. Laurinaviciene, A. Laurinavicius, R. Gudas, M. Malinauskas, and R. Maciulaitis, "Preclinical

study of SZ2080 material 3D microstructured scaffolds for cartilage tissue engineering made by femtosecond direct laser writing lithography," Biofabrication **7**, 015015 (2015).

148. J. K. Hohmann and G. von Freymann, "Influence of Direct Laser Written 3D Topographies on Proliferation and Differentiation of Osteoblast-Like Cells: Towards Improved Implant Surfaces," Advanced Functional Materials **24**, 6573-6580 (2014).
149. A. K. Nguyen and R. J. Narayan, "Two-photon polymerization for biological applications," Materials Today **20**, 314-322 (2017).
150. A. Marino, C. Filippeschi, V. Mattoli, B. Mazzolai, and G. Ciofani, "Biomimicry at the nanoscale: current research and perspectives of two-photon polymerization," Nanoscale **7**, 2841-2850 (2015).
151. F. Klein, B. Richter, T. Striebel, C. M. Franz, G. von Freymann, M. Wegener, and M. Bastmeyer, "Two-component polymer scaffolds for controlled three-dimensional cell culture," Adv Mater **23**, 1341-1345 (2011).
152. B. Richter, V. Hahn, S. Bertels, T. K. Claus, M. Wegener, G. Delaittre, C. Barner-Kowollik, and M. Bastmeyer, "Guiding Cell Attachment in 3D Microscaffolds Selectively Functionalized with Two Distinct Adhesion Proteins," Adv Mater **29**(2017).
153. C. Barner-Kowollik, M. Bastmeyer, E. Blasco, G. Delaittre, P. Muller, B. Richter, and M. Wegener, "3D Laser Micro- and Nanoprinting: Challenges for Chemistry," Angew Chem Int Ed Engl **56**, 15828-15845 (2017).
154. R. L. Truby and J. A. Lewis, "Printing soft matter in three dimensions," Nature **540**, 371-378 (2016).
155. N. D. Parab, J. E. Barnes, C. Zhao, R. W. Cunningham, K. Fezzaa, A. D. Rollett, and T. Sun, "Real time observation of binder jetting printing process using high-speed X-ray imaging," Sci Rep **9**, 2499 (2019).
156. B. Derby, "Inkjet Printing of Functional and Structural Materials: Fluid Property Requirements, Feature Stability, and Resolution," Annual Review of Materials Research **40**, 395-414 (2010).
157. B. J. de Gans, P. C. Duineveld, and U. S. Schubert, "Inkjet Printing of Polymers: State of the Art and Future Developments," Advanced Materials **16**, 203-213 (2004).
158. Z. Zhu, S. Z. Guo, T. Hirdler, C. Eide, X. Fan, J. Tolar, and M. C. McAlpine, "3D Printed Functional and Biological Materials on Moving Freeform Surfaces," Adv Mater **30**, e1707495 (2018).
159. I. S. Kinstlinger, A. Bastian, S. J. Paulsen, D. H. Hwang, A. H. Ta, D. R. Yalacki, T. Schmidt, and J. S. Miller, "Open-Source Selective Laser Sintering (OpenSLS) of Nylon and Biocompatible Polycaprolactone," PLoS One **11**, e0147399 (2016).
160. H. J. R. o. s. i. Kodama, "Automatic method for fabricating a three-dimensional plastic model with photo-hardening polymer," **52**, 1770-1773 (1981).
161. C. Sun, N. Fang, D. M. Wu, and X. Zhang, "Projection micro-stereolithography using digital micro-mirror dynamic mask," Sensors and Actuators A: Physical **121**, 113-120 (2005).
162. M. J. Yin, M. Yao, S. Gao, A. P. Zhang, H. Y. Tam, and P. K. Wai, "Rapid 3D Patterning of Poly(acrylic acid) Ionic Hydrogel for Miniature pH Sensors," Adv Mater **28**, 1394-1399 (2016).
163. B. H. Cumpston, S. P. Ananthavel, S. Barlow, D. L. Dyer, J. E. Ehrlich, L. L. Erskine, A. A. Heikal, S. M. Kuebler, I. Y. S. Lee, D. McCord-Maughon, J. Qin, H. Rockel, M. Rumi, X.-L. Wu, S. R. Marder, and J. W. Perry, "Two-photon polymerization initiators for three-dimensional optical data storage and microfabrication," Nature **398**, 51-54 (1999).
164. E. Avci, M. Grammatikopoulou, and G.-Z. Yang, "Laser-Printing and 3D Optical-Control of Untethered Microrobots," Advanced Optical Materials **5**(2017).
165. J. R. Tumbleston, D. Shirvanyants, N. Ermoshkin, R. Janusziewicz, A. R. Johnson, D. Kelly, K.

Chen, R. Pinschmidt, J. P. Rolland, A. Ermoshkin, E. T. Samulski, and J. M. DeSimone, "Continuous liquid interface production of 3D objects," Science **347**, 1349-1352 (2015).

166. V. F. Paz, M. Emons, K. Obata, A. Ovsianikov, S. Peterhänsel, K. Frenner, C. Reinhardt, B. Chichkov, U. Morgner, and W. Osten, "Development of functional sub-100 nm structures with 3D two-photon polymerization technique and optical methods for characterization," Journal of Laser Applications **24**, 042004 (2012).
167. W. Zhu, X. Qu, J. Zhu, X. Ma, S. Patel, J. Liu, P. Wang, C. S. Lai, M. Gou, Y. Xu, K. Zhang, and S. Chen, "Direct 3D bioprinting of prevascularized tissue constructs with complex microarchitecture," Biomaterials **124**, 106-115 (2017).
168. S. Kawata, H.-B. Sun, T. Tanaka, and K. Takada, "Finer features for functional microdevices," Nature **412**, 697-698 (2001).
169. S. Maruo, O. Nakamura, and S. Kawata, "Three-dimensional microfabrication with two-photon-absorbed photopolymerization," Optics Letters **22**, 132-134 (1997).
170. J. Fischer and M. Wegener, "Three-dimensional optical laser lithography beyond the diffraction limit," Laser & Photonics Reviews **7**, 22-44 (2013).
171. L. J. Hornbeck, *Digital Light Processing for high-brightness high-resolution applications*, Electronic Imaging '97 (SPIE, 1997), Vol. 3013.
172. L. J. Hornbeck, "Spatial light modulator and method," (Google Patents, 1987).
173. A. Travinsky, D. Vorobiev, Z. Ninkov, A. Raisanen, M. A. Quijada, S. A. Smee, J. A. Pellish, T. Schwartz, M. Robberto, S. Heap, D. Conley, C. Benavides, N. Garcia, Z. Bredl, and S. Yllanes, "Evaluation of digital micromirror devices for use in space-based multiobject spectrometer application," **3**, 1-20, 20 (2017).
174. T. Yoon, C.-S. Kim, K. Kim, and J.-r. Choi, "Emerging applications of digital micromirror devices in biophotonic fields," Optics & Laser Technology **104**, 17-25 (2018).
175. H.-F. Shih, Y.-C. Lee, Y. Chiu, D. W.-C. Chao, G.-D. Lin, C.-S. Lu, and J.-C. Chiou, "Micro objective lens with NA 0.65 for the blue-light small-form-factor optical pickup head," Optics Express **16**, 13150-13157 (2008).
176. Z. N. Tian, L. J. Wang, Q. D. Chen, T. Jiang, L. Qin, L. J. Wang, and H. B. Sun, "Beam shaping of edge-emitting diode lasers using a single double-axial hyperboloidal micro-lens," Opt Lett **38**, 5414-5417 (2013).
177. Y.-J. Lin, Y. Chiu, H.-F. Shih, and J.-C. Chiou, "Fabrication and Verification of a Small-Form-Factor Blue-Light Optical Pickup Head With Holographic Optical Element," Journal of Lightwave Technology **30**, 38-42 (2012).
178. H. M. Leung, G. Zhou, H. Yu, F. S. Chau, and A. S. Kumar, "Liquid tunable double-focus lens fabricated with diamond cutting and soft lithography," Appl. Opt. **48**, 5733-5740 (2009).
179. J.-M. Lee, D. Lee, and Y. Baek, "Fabrication of dual-focus dual-layered microlens," Optics Communications **289**, 69-74 (2013).
180. Z. Xia, Y. Li, X. Su, Y. Han, Z. Guo, J. Gao, Q. Sun, and S. Qu, "Fabrication of polymer compound microlens by lens-on-lens microstructures," Current Applied Physics **17**, 110-114 (2017).
181. X. J. Shen, L.-W. Pan, and L. Lin, "Microplastic embossing process: experimental and theoretical characterizations," Sensors and Actuators A: Physical **97–98**, 428-433 (2002).
182. M. Blattmann, M. Ocker, H. Zappe, and A. Seifert, "Jet printing of convex and concave polymer micro-lenses," Opt Express **23**, 24525-24536 (2015).
183. J. Yong, F. Chen, Q. Yang, G. Du, H. Bian, D. Zhang, J. Si, F. Yun, and X. Hou, "Rapid fabrication

of large-area concave microlens arrays on PDMS by a femtosecond laser," ACS Appl Mater Interfaces **5**, 9382-9385 (2013).

184. J.-G. Hua, Z.-N. Tian, S.-J. Xu, S. Lundgaard, and S. Juodkazis, "Fast fabrication of optical vortex generators by femtosecond laser ablation," Applied Surface Science **475**, 660-665 (2019).
185. T. Gissibl, S. Thiele, A. Herkommer, and H. Giessen, "Two-photon direct laser writing of ultracompact multi-lens objectives," Nature Photonics **10**, 554-560 (2016).
186. N. Tsutsumi, J. Hirota, K. Kinashi, and W. Sakai, "Direct laser writing for micro-optical devices using a negative photoresist," Opt Express **25**, 31539-31551 (2017).
187. G. von Freymann, L. Jonusauskas, A. Žukauskas, P. Danilevicius, M. Malinauskas, W. V. Schoenfeld, and R. C. Rumpf, "Fabrication, replication, and characterization of microlenses for optofluidic applications," in *Advanced Fabrication Technologies for Micro/Nano Optics and Photonics VI,* (2013).
188. Y. Lu and S. Chen, "Direct write of microlens array using digital projection photopolymerization," Applied Physics Letters **92**, 041109 (2008).
189. N. Lindlein, "Simulation of micro-optical systems including microlens arrays," Journal of Optics A: Pure and Applied Optics **4**, S1-S9 (2002).
190. A. Akatay and H. Urey, "Design and optimization of microlens array based high resolution beam steering system," Optics Express **15**, 4523-4529 (2007).
191. I. Powell, "Design of a laser beam line expander," Appl. Opt. **26**, 3705-3709 (1987).
192. K. J. Vahala, "Optical microcavities," Nature **424**, 839-846 (2003).
193. J. Kim, D. Yang, S.-h. Oh, and K. An, "Coherent single-atom superradiance," Science (2017).
194. G. Crosnier, D. Sanchez, S. Bouchoule, P. Monnier, G. Beaudoin, I. Sagnes, R. Raj, and F. Raineri, "Hybrid indium phosphide-on-silicon nanolaser diode," Nature Photonics **11**, 297-300 (2017).
195. N. B. Tomazio, L. Boni, and C. R. Mendonca, "Low threshold Rhodamine-doped whispering gallery mode microlasers fabricated by direct laser writing," Sci Rep **7**, 8559 (2017).
196. T. Grossmann, S. Schleede, M. Hauser, M. B. Christiansen, C. Vannahme, C. Eschenbaum, S. Klinkhammer, T. Beck, J. Fuchs, G. U. Nienhaus, U. Lemmer, A. Kristensen, T. Mappes, and H. Kalt, "Low-threshold conical microcavity dye lasers," Applied Physics Letters **97**, 063304 (2010).
197. S. Lacey, I. M. White, Y. Sun, S. I. Shopova, J. M. Cupps, P. Zhang, and X. Fan, "Versatile opto-fluidic ring resonator lasers with ultra-low threshold," Optics Express **15**, 15523-15530 (2007).
198. J. C. Knight, G. Cheung, F. Jacques, and T. A. Birks, "Phase-matched excitation of whispering-gallery-mode resonances by a fiber taper," Optics Letters **22**, 1129-1131 (1997).
199. T. Grossmann, T. Wienhold, U. Bog, T. Beck, C. Friedmann, H. Kalt, and T. Mappes, "Polymeric photonic molecule super-mode lasers on silicon," Light: Science & Applications **2**, e82 (2013).
200. L. Jin, Y. Wu, Y. Wang, S. Liu, Y. Zhang, Z. Li, X. Chen, W. Zhang, S. Xiao, and Q. Song, "Mass-Manufactural Lanthanide-Based Ultraviolet B Microlasers," Adv Mater, e1807079 (2018).
201. L. Wan, H. Chandrahalim, J. Zhou, Z. Li, C. Chen, S. Cho, H. Zhang, T. Mei, H. Tian, Y. Oki, N. Nishimura, X. Fan, and L. J. Guo, "Demonstration of versatile whispering-gallery micro-lasers for remote refractive index sensing," Opt Express **26**, 5800-5809 (2018).
202. S. Pang, R. E. Beckham, and K. E. Meissner, "Quantum dot-embedded microspheres for remote refractive index sensing," Appl Phys Lett **92**, 221108-2211083 (2008).
203. T. Wienhold, S. Kraemmer, S. F. Wondimu, T. Siegle, U. Bog, U. Weinzierl, S. Schmidt, H. Becker, H. Kalt, T. Mappes, S. Koeber, and C. Koos, "All-polymer photonic sensing platform based on whispering-gallery mode microgoblet lasers," Lab Chip **15**, 3800-3806 (2015).

204. L. J. Chen, L. L. Gong, Y. L. Lin, X. Y. Jin, H. Y. Li, S. S. Li, K. J. Che, Z. P. Cai, and C. J. Yang, "Microfluidic fabrication of cholesteric liquid crystal core-shell structures toward magnetically transportable microlasers," Lab Chip **16**, 1206-1213 (2016).
205. C. Chung-Yen and L. J. Guo, "Design and optimization of microring resonators in biochemical sensing applications," Journal of Lightwave Technology **24**, 1395-1402 (2006).
206. U. Bog, F. Brinkmann, H. Kalt, C. Koos, T. Mappes, M. Hirtz, H. Fuchs, and S. Kober, "Large-scale parallel surface functionalization of goblet-type whispering gallery mode microcavity arrays for biosensing applications," Small **10**, 3863-3868 (2014).
207. Y. Sun, S. I. Shopova, C. S. Wu, S. Arnold, and X. Fan, "Bioinspired optofluidic FRET lasers via DNA scaffolds," Proc Natl Acad Sci U S A **107**, 16039-16042 (2010).
208. W. Lee, Q. Chen, X. Fan, and D. K. Yoon, "Digital DNA detection based on a compact optofluidic laser with ultra-low sample consumption," Lab Chip **16**, 4770-4776 (2016).
209. C. Gong, Y. Gong, Q. Chen, Y. J. Rao, G. D. Peng, and X. Fan, "Reproducible fiber optofluidic laser for disposable and array applications," Lab Chip **17**, 3431-3436 (2017).
210. M. S. Pepe, R. Etzioni, Z. Feng, J. D. Potter, M. L. Thompson, M. Thornquist, M. Winget, and Y. Yasui, "Phases of Biomarker Development for Early Detection of Cancer," JNCI: Journal of the National Cancer Institute **93**, 1054-1061 (2001).
211. S. Dehghani, R. Nosrati, M. Yousefi, A. Nezami, F. Soltani, S. M. Taghdisi, K. Abnous, M. Alibolandi, and M. Ramezani, "Aptamer-based biosensors and nanosensors for the detection of vascular endothelial growth factor (VEGF): A review," Biosens Bioelectron **110**, 23-37 (2018).
212. L. Gnudi, S. Benedetti, A. S. Woolf, and D. A. Long, "Vascular growth factors play critical roles in kidney glomeruli," Clin Sci (Lond) **129**, 1225-1236 (2015).
213. X.-M. Fu, Z.-J. Liu, S.-X. Cai, Y.-P. Zhao, D.-Z. Wu, C.-Y. Li, and J.-H. Chen, "Electrochemical aptasensor for the detection of vascular endothelial growth factor (VEGF) based on DNA-templated Ag/Pt bimetallic nanoclusters," Chinese Chemical Letters **27**, 920-926 (2016).
214. D. M. Rissin, C. W. Kan, T. G. Campbell, S. C. Howes, D. R. Fournier, L. Song, T. Piech, P. P. Patel, L. Chang, A. J. Rivnak, E. P. Ferrell, J. D. Randall, G. K. Provuncher, D. R. Walt, and D. C. Duffy, "Single-molecule enzyme-linked immunosorbent assay detects serum proteins at subfemtomolar concentrations," Nat Biotechnol **28**, 595-599 (2010).
215. R. de la Rica and M. M. Stevens, "Plasmonic ELISA for the ultrasensitive detection of disease biomarkers with the naked eye," Nat Nanotechnol **7**, 821-824 (2012).
216. X. Wu, M. K. Oo, K. Reddy, Q. Chen, Y. Sun, and X. Fan, "Optofluidic laser for dual-mode sensitive biomolecular detection with a large dynamic range," Nat Commun **5**, 3779 (2014).
217. W. Xie, M. Tian, X. Luo, Y. Jiang, N. He, X. Liao, and Y. Liu, "A dual-mode fluorescent and colorimetric immunoassay based on in situ ascorbic acid-induced signal generation from metal-organic frameworks," Sensors and Actuators B: Chemical **302**(2020).
218. Y. Zhang, Q. Zhang, X. Ouyang, D. Y. Lei, A. P. Zhang, and H. Y. Tam, "Ultrafast Light-Controlled Growth of Silver Nanoparticles for Direct Plasmonic Color Printing," ACS Nano **12**, 9913-9921 (2018).
219. X. Ouyang, Z. Yin, J. Wu, C. Zhou, and A. P. Zhang, "Rapid optical u-printing of polymer top-lensed microlens array," Optics Express **27**, 18376-18382 (2019).
220. E. M. Purcell, "Spontaneous Emission Probabilities at Radio Frequencies," in *Confined Electrons and Photons: New Physics and Applications*, E. Burstein and C. Weisbuch, eds. (Springer US, Boston, MA, 1995), pp. 839-839.

221. Y. Huang, M. Ding, T. Guo, D. Hu, Y. Cao, L. Jin, and B. O. Guan, "A fiber-optic sensor for neurotransmitters with ultralow concentration: near-infrared plasmonic electromagnetic field enhancement using raspberry-like meso-SiO2 nanospheres," Nanoscale **9**, 14929-14936 (2017).

222. B.-b. Huang, M.-j. Yin, A. P. Zhang, and X.-s. Ye, "On-chip microfabrication of thermally controllable PNIPAAm microvalves by using optical maskless stereolithography," Sensors and Actuators A: Physical **247**, 397-402 (2016).

223. V. Sunkara and Y. K. Cho, "Investigation on the mechanism of aminosilane-mediated bonding of thermoplastics and poly(dimethylsiloxane)," ACS Appl Mater Interfaces **4**, 6537-6544 (2012).

224. A. Shrivastava and V. Gupta, "Methods for the determination of limit of detection and limit of quantitation of the analytical methods," Chronicles of Young Scientists **2**(2011).

225. D. Sun, F. Cao, W. Xu, Q. Chen, W. Shi, and S. Xu, "Ultrasensitive and Simultaneous Detection of Two Cytokines Secreted by Single Cell in Microfluidic Droplets via Magnetic-Field Amplified SERS," Anal Chem **91**, 2551-2558 (2019).

226. R. Rizzo, M. Alvaro, N. Danz, L. Napione, E. Descrovi, S. Schmieder, A. Sinibaldi, R. Chandrawati, S. Rana, P. Munzert, T. Schubert, E. Maillart, A. Anopchenko, P. Rivolo, A. Mascioletti, F. Sonntag, M. M. Stevens, F. Bussolino, and F. Michelotti, "Bloch surface wave label-free and fluorescence platform for the detection of VEGF biomarker in biological matrices," Sensors and Actuators B: Chemical **255**, 2143-2150 (2018).

227. M. Y. Hsu, Y. C. Hung, D. K. Hwang, S. C. Lin, K. H. Lin, C. Y. Wang, H. Y. Choi, Y. P. Wang, and C. M. Cheng, "Detection of aqueous VEGF concentrations before and after intravitreal injection of anti-VEGF antibody using low-volume sampling paper-based ELISA," Sci Rep **6**, 34631 (2016).

228. R. Malhotra, V. Patel, B. V. Chikkaveeraiah, B. S. Munge, S. C. Cheong, R. B. Zain, M. T. Abraham, D. K. Dey, J. S. Gutkind, and J. F. Rusling, "Ultrasensitive detection of cancer biomarkers in the clinic by use of a nanostructured microfluidic array," Anal Chem **84**, 6249-6255 (2012).

229. J. Ko, S. Lee, E. K. Lee, S. I. Chang, L. Chen, S. Y. Yoon, and J. Choo, "SERS-based immunoassay of tumor marker VEGF using DNA aptamers and silica-encapsulated hollow gold nanospheres," Phys Chem Chem Phys **15**, 5379-5385 (2013).

230. L. G. Griffith and M. A. Swartz, "Capturing complex 3D tissue physiology in vitro," Nat Rev Mol Cell Biol **7**, 211-224 (2006).

231. S. I. Fraley, Y. Feng, R. Krishnamurthy, D. H. Kim, A. Celedon, G. D. Longmore, and D. Wirtz, "A distinctive role for focal adhesion proteins in three-dimensional cell motility," Nat Cell Biol **12**, 598-604 (2010).

232. M. Ochsner, M. R. Dusseiller, H. M. Grandin, S. Luna-Morris, M. Textor, V. Vogel, and M. L. Smith, "Micro-well arrays for 3D shape control and high resolution analysis of single cells," Lab Chip **7**, 1074-1077 (2007).

233. R. R. Jose, M. J. Rodriguez, T. A. Dixon, F. Omenetto, and D. L. Kaplan, "Evolution of Bioinks and Additive Manufacturing Technologies for 3D Bioprinting," ACS Biomaterials Science & Engineering **2**, 1662-1678 (2016).

234. T. Xu, K. W. Binder, M. Z. Albanna, D. Dice, W. Zhao, J. J. Yoo, and A. Atala, "Hybrid printing of mechanically and biologically improved constructs for cartilage tissue engineering applications," Biofabrication **5**, 015001 (2013).

235. A. Skardal and A. Atala, "Biomaterials for integration with 3-D bioprinting," Ann Biomed Eng **43**, 730-746 (2015).

236. M. M. Stanton, J. Samitier, and S. Sanchez, "Bioprinting of 3D hydrogels," Lab Chip **15**, 3111-3115

(2015).

237. J. Visser, B. Peters, T. J. Burger, J. Boomstra, W. J. Dhert, F. P. Melchels, and J. Malda, "Biofabrication of multi-material anatomically shaped tissue constructs," Biofabrication **5**, 035007 (2013).
238. S. Tasoglu and U. Demirci, "Bioprinting for stem cell research," Trends Biotechnol **31**, 10-19 (2013).
239. R. Xiong, Z. Zhang, W. Chai, Y. Huang, and D. B. Chrisey, "Freeform drop-on-demand laser printing of 3D alginate and cellular constructs," Biofabrication **7**, 045011 (2015).
240. H. Gudapati, M. Dey, and I. Ozbolat, "A comprehensive review on droplet-based bioprinting: Past, present and future," Biomaterials **102**, 20-42 (2016).
241. A. B. Dababneh and I. T. Ozbolat, "Bioprinting Technology: A Current State-of-the-Art Review," Journal of Manufacturing Science and Engineering **136**, 061016-061016-061011 (2014).
242. A. M. Greiner, B. Richter, and M. Bastmeyer, "Micro-engineered 3D scaffolds for cell culture studies," Macromol Biosci **12**, 1301-1314 (2012).
243. M. H. Tong, N. Huang, W. Zhang, Z. L. Zhou, A. H. Ngan, Y. Du, and B. P. Chan, "Multiphoton photochemical crosslinking-based fabrication of protein micropatterns with controllable mechanical properties for single cell traction force measurements," Sci Rep **6**, 20063 (2016).
244. A. M. Greiner, F. Klein, T. Gudzenko, B. Richter, T. Striebel, B. G. Wundari, T. J. Autenrieth, M. Wegener, C. M. Franz, and M. Bastmeyer, "Cell type-specific adaptation of cellular and nuclear volume in micro-engineered 3D environments," Biomaterials **69**, 121-132 (2015).
245. P. Tayalia, C. R. Mendonca, T. Baldacchini, D. J. Mooney, and E. Mazur, "3D Cell-Migration Studies using Two-Photon Engineered Polymer Scaffolds," Advanced Materials **20**, 4494-4498 (2008).
246. B. Spagnolo, V. Brunetti, G. Lemenager, E. De Luca, L. Sileo, T. Pellegrino, P. Paolo Pompa, M. De Vittorio, and F. Pisanello, "Three-dimensional cage-like microscaffolds for cell invasion studies," Sci Rep **5**, 10531 (2015).
247. S. H. Lee, J. J. Moon, and J. L. West, "Three-dimensional micropatterning of bioactive hydrogels via two-photon laser scanning photolithography for guided 3D cell migration," Biomaterials **29**, 2962-2968 (2008).
248. T. Billiet, M. Vandenhaute, J. Schelfhout, S. Van Vlierberghe, and P. Dubruel, "A review of trends and limitations in hydrogel-rapid prototyping for tissue engineering," Biomaterials **33**, 6020-6041 (2012).
249. C. G. Williams, A. N. Malik, T. K. Kim, P. N. Manson, and J. H. Elisseeff, "Variable cytocompatibility of six cell lines with photoinitiators used for polymerizing hydrogels and cell encapsulation," Biomaterials **26**, 1211-1218 (2005).
250. J. W. Nichol, S. T. Koshy, H. Bae, C. M. Hwang, S. Yamanlar, and A. Khademhosseini, "Cell-laden microengineered gelatin methacrylate hydrogels," Biomaterials **31**, 5536-5544 (2010).
251. Q. Hamid, C. Wang, J. Snyder, and W. Sun, "Surface modification of SU-8 for enhanced cell attachment and proliferation within microfluidic chips," J Biomed Mater Res B Appl Biomater **103**, 473-484 (2015).